DESIGN AND OPTIMIZATION OF THE COMPONENTS OF AN ACCELERATOR DRIVEN THORIUM-FUELED MOLTEN SALT LOOP USING MCNP6/SERPENT2 MONTE CARLO METHODS

A Thesis

by

EMAN HAITHAM MOHAMMAD AL SMADI

Submitted to the Office of Graduate and Professional Studies of
Texas A&M University
in partial fulfillment of the requirements for the degree of

MASTER OF SCIENCE

Chair of Committee,	Yassin A. Hassan
Committee Members,	Rodolfo Vaghetto
	Kalyan Annamalai
Head of Department,	Micheal Nastasi

August 2020

Major Subject: Nuclear Engineering

ABSTRACT

This thesis summarizes an intensive computational study to a proton accelerator-driven thorium-fueled molten salt reactor, including sensitivity analysis, parametric studies, and design & optimization for selected components of the molten salt loop facility using MCNP6 code, and results benchmark using SERPENT2 Monte Carlo method. The accelerator-driven thorium molten salt reactor is located at the thermal-hydraulics laboratory at Texas A & M University, it is composed of two parts; the proton accelerator coupled with a thorium molten salt test loop. The proton accelerator was used as a neutron generator via spallation reaction, and the molten salt loop which confines and circulates the thorium molten salt. The main goal behind this research is to impose the required boundary conditions on molten salt flow and induce fast fission events of ^{232}Th within the molten salt in a safe, subcritical nuclear facility. The research consists of 3 parts, MCNP6 simulations, SERPENT2 simulations, and MCNP6-SERPENT2 benchmark, simulations are divided into phases, where each phase aims to accomplish a certain task. MCNP6 simulations were run with a license through the inspect Oak Ridge National Laboratory (ORNL) cluster, and SERPENT2 simulations were run on a local computer with a license that was provided from the code developer.

DEDICATION

First and foremost, praises and thanks to ALLAH, the Almighty, for his blessings, mercy, and compassion that gave me the persistence and strength to accomplish this work successfully.

I would like express my sincere gratitude to my professor Dr.Yassin Hassan for giving me the opportunity to work on this research providing invaluable guidance. I am also thankful to Dr.Rodolfo Vaghetto who has given me a continuous support and encouragement through out this research. I am deeply indebted for Sero Yang, whose vision, sincerity, stimulating suggestion, and motivation have inspired me.

I am extremely grateful to my parents, for their love, care, affection, encouragement, and prayers of day and night made me able to get such success and honor. Thank you for believing in me and making me believe in myself.

Dr. Rafil Ali, my sweet fiancee, you have been an inspiration, thank you for your complete support, love, encouragement, every day, even from afar, it has always made a difference. It has been incredible having you beside as I flourish, may the next chapter of our adventures and achievements involve a bit less FaceTime across the country.

ACKNOWLEDGMENTS

The research presented in this thesis was part of Thorium Research Initiative project established between Texas Thorium LLC and the thermal-hydraulic research laboratory at Texas A&M University. I would like to express my gratitude to the Texas Thorium LLC for the funding received that made this research possible. I would also like to thank personally Mr.Holloway Frost and Mr. Bob McAughan for their continuous technical guidance and interactions throughout the entire duration of the project.

Their curiosity and enthusiasm shown during our meetings motivated all the students and researchers involved in the project. .

CONTRIBUTORS AND FUNDING SOURCES

Contributors

This work was supported and guided by Professor Yassin Hassan, supervised by Dr.Rodolfo Vaghetto. Special thanks to Sero Yang for his technical contribution, to and Trevor Parker for his participation. All other work conducted for the thesis was completed by the student independently.

Funding Sources

The research presented in this thesis was part of Thorium Research Initiative project established between Texas Thorium LLC and the thermal-hydraulic research laboratory at Texas A&M University.

NOMENCLATURE

MSR	Molten Salt Reactor
ORNL	Oak Ridge National Laboratory
ARE	Aircraft Reactor Experiment
MSRE	Molten Salt Reactor Experiment
MSBR	Molten Salt Breeder Reactor
LFTR	Liquid Fluoride Thorium Reactor
VHTR	Very High Temperature Reactor
MSRSSC	Molten Salt Reactor System Steering Committee
FLiBe	LiF-BeF_2
FLiNaK	LiF-NaF-KF
FLiNak-ThF_4	LiF-NaF-KF-ThF_4
MA	Minor Actinide
SF	Spent Fuel
ADS	Accelerator Driven System
ADMSR	Accelerator Driven Molten Salt Reactor
MC	Monte Carlo
MCNP	Monte Carlo N-Particle
SERPENT	Monte Carlo Nuetronics Code
OECD/NEA	Organization for Economic Co-operation and Development Nuclear Energy Agency
RSICC	Radiation Safety Information Computational Center
CFD	Computational Fluid Dynamics

ANL	Argon National Laboratory
REBUS	Monte Carlo Reactor Burn-up System
GDR	Giant Dipole Resonance
NaF	Sodium Fluoride
UF	Uranium Fluoride
BNL	Brookhaven National Laboratory
MSRP	Molten Salt Reactor Program
THORIMS-NES	Thorium-Molten Salt Nuclear Energy Synergetics
MSB	Molten Salt Fissile Breeder
AMSB	Accelerator Molten Salt Breeder
MEPHI	Moscow Engineering Physics Institute
MCU-PTR	Monte Carlo Universal code
ACE/MCU	A Compact ENDF/Monte Carlo Universal
TRIGA	Training, Research, Isotopes, General Atomic
STL	Stereolithography Geometry
NESTLE	Nodal Kinetics code for Steady-state and Transient Reactor Neutronics
CTU	Czech Technical University
MTC	Moderator Temperature Coefficients
TRI	Thorium Reactor Initiative
ENDF	Evaluated Nuclear Data File
JEFF	Joint Evaluated Fission and Fusion File
ID	Inner Diameter
OD	Outer Diameter
PE	Poly-ethylene

BPE	Borated Poly-ethylene
ICRP	International Commission on Radiological Protection
NSC	Nuclear Science Center

TABLE OF CONTENTS

Page

ABSTRACT ii

DEDICATION iii

ACKNOWLEDGMENTS iv

CONTRIBUTORS AND FUNDING SOURCES v

NOMENCLATURE vi

TABLE OF CONTENTS ix

LIST OF FIGURES xi

LIST OF TABLES xv

1. INTRODUCTION 1

    1.1 Molten Salt Reactors 1
        1.1.1 Molten Salt 1
        1.1.2 Advantages 2
        1.1.3 Literature Review 3
        1.1.4 Proton Accelerator Driven System 6
        1.1.5 Facility Description 10
    1.2 Scope And Goal 12

2. METHODOLOGY 13

    2.1 Neutron Transport Theory 13
    2.2 Stochastic And Deterministic Methods 13
    2.3 Monte Carlo Methods 14
    2.4 Fundamentals of Monte Carlo Particle Transport 16
    2.5 Tools 19
        2.5.1 MCNP6 Code 20
        2.5.2 SERPENT2 Code 21
        2.5.3 Nuclear Data 22

3. RESULTS 23

    3.1 MCNP6 Simulation Results 23

3.1.1 Phase 1 24
3.1.1.1 Case 1 Results 26
3.1.1.2 Case 2 Results 28
3.1.1.3 Cases 3, 4, 5, and 6 Results 30
3.1.1.4 Phase 1 conclusion 34
3.1.2 Phase 2 35
3.1.2.1 Phase 2 Results 36
3.1.3 Phase 3 38
3.1.3.1 Phase 3 Results 41
3.1.4 Phase 4 42
3.1.4.1 Phase 4 Results 43
3.1.5 Phase 5 45
3.1.5.1 Phase 5 Results 45
3.1.6 Phase 6 51
3.1.6.1 Phase 6 Results 52
3.1.7 Phase 7 54
3.1.7.1 Phase 7 Results 55
3.1.8 Phase 8 59
3.1.8.1 Phase 8 Results 60
3.1.9 Phase 9 62
3.1.9.1 Phase 9 Results 62
3.1.10 Phase 10 70
3.1.10.1 Phase 10 Results 70
3.2 SERPENT2 Simulations Results 74
3.2.1 Source Conversion And Geometrical Design 75
3.2.2 Shielding Material Specification 77
3.2.3 Shielding design sensitivity analysis 77
3.2.4 Lithium target sensitivity analysis 78

4. DISCUSSION AND CONCLUSIONS 82

4.1 Shielding Material Composition Bench Marking 82
4.2 Shielding Material Thickness Bench Marking 85
4.3 Target Thickness Bench Marking 87
4.4 Conclusion 88

REFERENCES 89

LIST OF FIGURES

FIGURE Page

1.1 Fast fission cross-section ^{232}Th 8

1.2 Photo fission cross-section ^{232}Th 8

1.3 Photo neutron cross-section ^{232}Th 9

1.4 Photo 2 neutrons cross-section ^{232}Th 9

1.5 ^{7}Li(p,n) spallation reaction cross-section as a function of proton energy 10

1.6 ^{9}Be(p,n) spallation reaction cross-section as a function of proton energy 11

2.1 Particle histories by Monte Carlo methods 18

3.1 3D MCNP model for neutron detectors 26

3.2 Neutron energy spectrum at a fixed surface (26.27 cm) with volumetric source 27

3.3 Neutron energy spectrum at the varying graphite surface with volumetric source 27

3.4 Integrated neutron flux as a function of graphite thickness with volumetric source ... 28

3.5 Neutron energy spectrum at a fixed surface (26.27 cm) with surface source 29

3.6 Neutron energy spectrum at the varying graphite surface with surface source 29

3.7 Integrated neutron flux as a function of graphite thickness with surface source 30

3.8 MCNP6 2D model for the proton beam, the proton circular disc source, the lithium target, the graphite shield, and the neutrons produced 31

3.9 Two source strengths impact on the surface neutron flux as a function of graphite thickness 32

3.10 Angular specification impact on the surface neutron flux as a functions of graphite thickness 33

3.11 Neutron energy spectrum at a varying graphite surface with mono-directional, squared disc, 3 MeV, and 2 $\mu Amps$ proton source 34

3.12 2D MCNP6 model for the proton source with graphite shielding 35

3.13 Contour plot for neutron flux as a function for five tested graphite shields 36

3.14 Neutron energy spectrum at a varying graphite surface with mono-directional, squared disc, 3 MeV, and 2 $\mu Amps$ proton source 37

3.15 Generated neutron spectrum for different proton source configurations..... 38

3.16 Axial neutron flux at the proton beam center using FMESH tally 39

3.17 2D MCNP model FLiNaK-ThF_4 test section 40

3.18 3D MCNP model FLiNaK-ThF_4 test section 40

3.19 ^{232}Th paths after neutron absorption 41

3.20 Axial neutron flux at the proton beam center with FLiNaK-ThF_4 42

3.21 ^{232}Th fission rate density in units of ($reactions/cm^3.s$) for case 1 43

3.22 ^{232}Th radiative capture rate density with 10^7 nps for case 1 44

3.23 ^{232}Th radiative capture rate density rate with 10^9 nps for case 1 44

3.24 ^{232}Th fission rate density for isotropic, energy weighted neutron source..... 46

3.25 ^{232}Th radiative capture rate density for isotropic, energy weighted neutron source ... 46

3.26 ^{232}Th fission rate density for isotropic, mono-energetic neutron source..... 47

3.27 ^{232}Th radiative capture rate density for isotropic, mono-energetic neutron source 47

3.28 ^{232}Th fission rate density for mono-directional, energy weighted neutron source 48

3.29 ^{232}Th radiative capture rate density for mono-directional, energy weighted neutron source 48

3.30 Contour plot of particles generated in 2D MCNP6 model 49

3.31 Neutron flux inside FLiNaK-ThF4 with 100 MeV, 20 $\mu Amps$ proton source 50

3.32 Contour plot of the neutron flux generated in 2D MCNP6 model 50

3.33 Neutron flux inside FLiNaK-ThF_4 with 100 MeV, 20 $\mu Amps$ proton source 51

3.34 Neutron flux inside FLiNaK-ThF_4 with 4.5 MeV, 2 $\mu Amps$ proton source for different perturbations 53

3.35 Axial neutron flux at the proton beam center with 4.5 MeV, 2 $\mu Amps$ proton source for different perturbations..... 54

3.36 Target location effect with 0.02 cm on the neutron flux inside FLiNaK-ThF_4 56

3.37 Target location effect with 3 cm on the neutron flux inside FLiNaK-ThF_4 56

3.38 Thickness sensitivity at the beam center (Z = 0 cm) 58

3.39 Thickness sensitivity at the end of the beam (Z = 28 cm)..... 58

3.40 The two tested locations for the Li target 60

3.41 Target thickness sensitivity at the end of the beam 61

3.42 Cylindrical volume detectors placed on both side of the shielding 63

3.43 Four wall detectors placed outside the shielding 64

3.44 3D MCNP6 model for the proton accelerator driven molten salt loop 65

3.45 Neutron spectrum leak out of the loop 66

3.46 Neutron spectrum leak out of the shielding 66

3.47 Point detectors dosimeter along the beam center line 67

3.48 Annual dose (288 hours/year) as a function of shielding thickness..... 68

3.49 Exposure limits fro NCRP report No.116 and ICRP publication 60..... 69

3.50 Four wall detectors placed outside the shielding 71

3.51 Comparison for the average neutron energy spectrum inside and outside the shield (detector) 71

3.52 Annual dose (100 hours/year) as a function of shielding thickness..... 72

3.53 Hourly dose rate as a function of shielding thickness for 4.5 MeV source energy 73

3.54 Hourly dose rate as a function of shielding thickness for 2.5 MeV source energy 74

3.55 The produced neutron energy spectrum using MCNP6 76

3.56 The produced neutron energy probability using MCNP6 76

3.57 Neutron spectrum leak out of the shielding for a neutron source using SERPENT2 .. 77

3.58 Average Neutron spectrum in the detector as a function of PE thickness using SERPENT2 78

3.59 Target thickness sensitivity at the end of the beam using SERPENT2 79

3.60 Neutrons produced using mesh plotter SERPENT2 where target is at the end of the beam 80

3.61 Neutrons produced using mesh plotter SERPENT2 where target is attached to the test section 81

4.1 Neutron spectrum leak out of the shielding for a neutron source using SERPENT2 code 82

4.2 Neutron spectrum leak out of the shielding for a neutron source using MCNP6 code 83

4.3 Neutron spectrum leak out of the shielding in MCNP6 and SERPENT2 84

4.4 Neutron spectrum inside FLiNaK-ThF_4 test section in MCNP6 and SERPENT2 84

4.5 Average neutron spectrum in the detector as a function of PE thickness using SERPENT2 85

4.6 Average neutron spectrum in the detector as a function of PE thickness using MCNP6 86

4.7 Average Neutron spectrum in the detector at 50 cm PE using MCNP6 and SERPENT2 86

4.8 Lithium target sensitivity analysis using MCNP6 and SERPENT2 87

LIST OF TABLES

TABLE Page

1.1 Lithium isotopes binding energies in MeV 10

3.1 MCNP phases 23

3.2 Phase 1 cases 24

3.3 Analytical full surface area 25

3.4 MCNP code cylindrical area 25

3.5 Phase 2 cases 35

3.6 Stainless steel 316 39

3.7 Phase 4 cases 43

3.8 Phase 5 cases 45

3.9 Phase 6 cases 51

3.10 Neutron production for phase 6 52

3.11 Phase 7 cases 55

3.12 Induced fission neutron production for phase 7 57

3.13 Phase 8 cases 59

3.14 Neutron production for different target depths 61

3.15 Weight fraction for different shielding compositions 68

3.16 Annual dose for different shielding compositions at different thickness 70

3.17 Characterization of SERPENT2 Model 75

1. INTRODUCTION

1.1 Molten Salt Reactors

Nuclear power research projects that were held through the years had a specific goal, it is to satisfy different constraints such as, waste management, neutron economy, fission product solubility, cost, operating conditions, and online processing availability. The principle concept of Generation IV Molten Salt Nuclear Reactors (MSR) is using fluoride or chloride salts as a primary coolant, fuel (fissile/fertile material) can be fixed solid or liquid dissolved in the liquid molten salt as a fuel carrier, which could also act as a primary coolant. The Molten Salt Reactor System Steering Committee (MSRSSC) was founded to perform research about MSR that uses liquid fuel dissolved in molten salt coolant mixture [1].

1.1.1 Molten Salt

The selection of molten salt in MSR should satisfy the reactor design criteria including proper thermal and physical properties, such as high heat transfer properties, stability at high temperature, ability to dissolve fuel actinides, low melting point at low pressure, high boiling point, and has a high neutron economy. Researches have led to the choice of either chloride salts or fluoride salts. Chlorides have some attractive advantages compared to fluorides in fast spectrum reactors because chlorine has two stable isotopes, these are ^{35}Cl and ^{37}Cl. Because ^{35}Cl gives rise to the production of ^{36}S, the isotope ^{37}Cl is much preferable to be used in fast reactors.

Researchers have concluded that the most efficient salts to use in thermal and epi-thermal MSR are fluoride salts [2], because the stable isotope ^{19}F is hard to get radioactive when bombarded by a neutron, it has a lower neutron absorption cross-section, and high neutron moderation compared with chlorine. Because the melting point of each separate component of is very high when compared to the salt composition melting point, choosing the optimum salt mole fraction composition depends on the minimum melting point and the best thermal properties.

Lithium Fluoride-Beryllium Fluoride denoted as (LiF-BeF_2) and Lithium Fluoride-Sodium

Fluoride-Potassium Fluoride denoted as (FLiNaK) in its eutectic composition [3] are used world-wide as a coolant fuel carrier thanks to their physical properties, like the salt density, salt heat capacity, and salt melting temperature. However, LiF-BeF_2 salt when examined have shown a moderate solubility of ThF_4 and UF_4, but a very small dissolution for the UPu fuel compared to the eutectic composition of FLiNaK salt that showed a supremely high solubility of PuF_3, UF_4, and AmF_3. FLiNaK salt that was tested by Bergman and Dragunov [4] has one eutectic point at 46.5-11.5-42 of LiF-NaF-KF, respectively. Lithium element is a component in both salts, natural lithium consists of 92.4% of ^{7}Li and 7.6% of ^{6}Li which has a large neutron absorption cross-section. Therefore, lithium should be 99.9% enriched with ^{7}Li isotope before including it in either salts.

1.1.2 Advantages

Many studies show that the operation of MSR is economically beneficial, like high-efficiency power cycles, however, there are some features that add extra cost, like the radioactive system remote maintenance. Developing the Molten Salt Breeder Reactor (MSBR) has a significance that arises from the need for cheaper nuclear energy. The MSBR which depends on breeding a fertile material to fissile material has also economic attractions that reduce the fuel cycle cost, like the fuel is processed on-site location, and the fact that there is no fuel fabrication, and low fissile fuel supply. The capital cost can be reduced as well, thanks to the low pressure, low damage, high thermal efficiency, and the breeding associated with this type of fuel. As a result, the above-mentioned cost savings overcome the cost that is needed to handle the radioactive fluids [5].

Liquid Fluoride Thorium Reactor (LFTR) concept is derived from the Molten Salt Reactor, which is in the Generation IV international forum list [6]. The advantages of LFTR fall into 3 main classifications that differentiate these reactors:

A. Safety: Three major properties play a role in the inherent safety feature of LFTR;

I. The ability of the molten salt to operate at low pressure: Because the boiling point of the salt is at 1400 $^\circ C$, there is no need to pressurize the reactor vessel, the salt is in a liquid phase at atmospheric pressure.

II. Negative temperature reactivity coefficient: As the temperature of the core rises, the reactivity reduces. The temperature reactivity coefficient is affected by several phenomena, like the expansion property of the molten salt when it heats up move the liquid fuel salt out of the core active area, the Doppler effect that induces a high neutron absorption cross-section as temperature increases, and the moderation efficiency of the graphite reflectors.

III. Liquid fuel: Fuel is already dissolved in the molten salt, as a result, meltdown accident will never occur.

B. Fuel efficiency: Molten salt can be heated up to temperatures greater than the conventional light water reactor under low pressure, which results in a higher fuel efficiency.

C. Radioactive waste: The thorium-uranium fuel cycle produces fission products similar to the ones produced in the conventional water-cooled reactors, but a quite different spectrum of actinides. However, the gas fission products in shapes of bubbles produced are removed from liquid salt by reactor system[6].

Removal of the Minor Actinides (MA) that exist in the Spent Fuel (SF) safely is either by burying them or by transmutation (convert) into short-lived radioactive fission products. MA inventories exist in the SF is almost 250 tons of americium-241 (^{241}Am) and 2 tons of curium-242 (^{242}Cm) all over the world, these numbers increase annually by almost 5 tons of 6241Am and decrease by 0.1 tons of ^{242}Cm [7]. The MA has to be incinerated at a rate faster than the rate of its production. MSR gained a huge attention in this regard because it has some valuable features over solid fuel reactors, such as no limitation on the fuel burn-up because no fuel swelling will occur and the elimination of the fuel fabrication facility that results in a highly toxic material. Another significance for MSR liquid fuel over the solid fuel stands out in emergencies, where the molten salt can be drained out fast from the reactor into cooling tanks, thus, stopping the fission chain [6].

1.1.3 Literature Review

The fluidized fuel dissolved in the molten salt application was adopted for the Aircraft Reactor Experiment (ARE) as a source of airplane motive force, nuclear stability analysis in the circulating system, and core heat removal by R. C. Brian and W.R. Grimes at ORNL, Tennessee, the United

States in 1950 [8]. Back in time, the only available fluoride fuel is a mixture of zirconium fluoride (ZrF_4), sodium fluoride (NaF), and uranium fluoride (UF_4) with 93.4% enrichment. They used a hexagon-shaped Beryllium oxide blocks for moderation, and these blocks were shielded from the fuel running tubes. The fluoride salts were the most suitable for such an experiment, thanks to its thermal and physical properties such as chemical stability, low pressure, radiation damage resistance, and high Uranium solubility. The experiment successfully operated in 1954, the operation of the ARE lasted for 9 days and then stopped. since then, power applications started considering the molten salt reactors.

In 1956, H. G. MacPherson conducted a research group to investigate the molten salt characteristics as converters and breeders [5]. They concluded after several years of investigation that graphite moderators and thorium fuel cycles are the best for MSR. MacPherson's research group considered 2 configurations of the graphite moderator in MSR, a single-fluid, means that thorium and uranium are dissolved in the same fluid, and a double-fluid, means that fissile and fertile fuel are separated. They concluded that even though the double-cycle fluid served a better breeding, single fluid is a better choice regarding the low economical cost.

In 1960, Macpherson was a project coordinator for a Molten Salt Reactor Program (MSRP) at ORNL. The program addressed the Molten Salt Reactor Experiment (MSRE), onstruction began in 1962 [5], MSRE components development, reactor engineering analysis such as core calculations, temperature coefficient behavior, and analog computer studies were investigated [9]. The Molten Salt Reactor Experiment (MSRE) was a single-fluid design, but the salt did not include the thorium, thus, it was similar to the double-fluid reactor. The fuel was a mixture of zirconium, lithium, uranium, and beryllium fluorides. The moderator was graphite blocks with a very small pore size so that the salt will not penetrate, criticality was achieved in 1965 and one year later, operation at full power was achieved with a max of 8000 KW where heat was vented to the outside atmosphere[5].

Phase two of the MSRE operation started in 1968 [5], a batch of ^{233}U was added to the salt carrier after removing the original uranium. The reactor reached criticality, being the first reactor that is operating based on ^{233}U. New experimental results in the field of core design development

caused ORNL to change the double fluid MSR breeder to a single fluid MSR breeder lately in 1967 [5]. This was due to two aspects; the graphite behavior at high exposure, and the chemical processing. Because data showed that radiation-exposed graphite moderator changed dimensions more than was expected, it was important to try to minimize graphite density in the reactor. Whenever the graphite reaches the radiation limit or grow a leak, it gets necessary to replace the whole core and entire reactor vessel.

A new chemical processing improvement was introduced, which enhanced the principle of the single fluid reactor, to maximize the thorium breeding in the single fluid reactor, the decay of protactinium into uranium should be outside of the core. This can be done by performing protactinium and uranium extraction chemically from the fluorides molten salt in the laboratory. Uranium can be extracted by adding molten bismuth to the salts, and protactinium can be stored in tanks until it decays to uranium, then transferred back to the reactor core via electrolysis, which can be fast and continuously. A similar process was developed in Brookhaven National Laboratory (BNL) and Argonne National Laboratory (ANL) for fission product removal from the molten bismuth. The progress in the core design that created a switch to the single fluid reactor was the recognition of the blanket that can be composed of salt including uranium and thorium.

This can be achieved by increasing the salt and minimizing the moderator at the outer part of the core, in order to maximize the thorium breeding. Thus, studies resumed about the single fluid reactor design, many studies indicated that the utilization of the fuel in the single fluid reactor can be as efficient as the double fluid reactors, with a better economics. Hence, the Molten Salt Reactor Program (MSRP) at ORNL started the development of a single fluid reactor in 1968 [5]. The Molten Salt Breeder Reactor (MSBR) was first developed by ORNL for low-cost power generation and breeding purposes. Research on the MSBR lasted from the 1970 to 1976 [7], and then research in the field of MSR stopped.

Japan resumed the research on the MSR in 1980 and initiated the Thorium-Molten Salt Nuclear Energy Synergetics project (THORIMS-NES)[10], the project proposed thorium resource utilization program that include a power station and a fissile material producer. The project suggested

two stages; the first is to develop the MSR that is already introduced by ORNL, and the second is to develop the Molten Salt Fissile Breeder (MSB). The FUJI project started a molten salt power station and an Accelerator Molten Salt Breeder (AMSB) facility that produce fissile material as a part of the THORIMS-NES project [11].

In the 1990s, interest in the MSR raised again with a concept of nuclear waste incineration in subcritical reactors, this was done by the TIER-1 project [12]. Another study showed that the thorium MSR can be operated in thermal, epi-thermal, and fast neutron spectrum [7]. But there were some problems that arise during the operation of each kind of spectrum. For example, operation at thermal spectrum had some safety issues which can be reduced by minimizing the distance between the graphite and the salt channel. However, the feedback was faintly negative and the graphite moderator has to be yearly reprocessed.

Unlike the epi-thermal spectrum, where the safety was improved due to a very negative feedback coefficient. The fast spectrum mode, which is a single molten salt loop and without a graphite moderator was the highest potential. This study serves as a proof and clarification that the fast spectrum has intrinsic advantages, because no graphite reprocessing will be necessary as in the thermal and epi-thermal spectrum.

Recently in the 2000s, interest has grown dramatically in the MSR, so the Molten Salt Reactor System Steering Committee (MSRSSC) was formed in the 2004 [13], first meeting was in 2005, Russia joined the forum in 2006, the policy group was decided in 2009, and the main activities started in 2010.

1.1.4 Proton Accelerator Driven System

Proton accelerator driven system is a nuclear facility that is built by coupling nuclear assemblies with a high energy proton accelerator. Accelerator Driven Systems (ADS) have safety features over conventional nuclear reactors, the system uses thorium as a fuel which is not fissile, hence, the fission reaction rate stops as soon as the proton accelerator stops, so they operate in subcritical mode. These facilities serve as breeders or MA incinerators, the concept is based on the spallation of a proton source into a solid target to produce neutrons.

The neutron population produced from interactions are then subjected to the test section or reactor core where they breed the fertile material such as ^{232}Th and convert it to fissile ^{233}U to be used in reactors.

There are 3 main characteristics for the accelerator-driven molten Salt breeder and converter:

1 - The system is operated in sub-critical mode, it is Based on 3 components, these are, the accelerator, the target to produce neutrons, and the blanket (test section.

2 - The target is considered as neutron source, more neutrons are generated (neutron multiplication) in the test section (blanket).

3 - The blanket here is the fuel dissolved in fluoride salt carrier.

In the molten salt breeder reactor, neutron generation in the target and blanket is not only due to spallation and fast events. In fact, high energetic photons can also produce neutrons via Photoneutron interactions, photofission interactions, and nuclei breakup. These interactions have maximum cross-section in the Giant Dipole Resounance (GDR) in energy range between (10-20) MeV near the nucleon binding energy which is almost 8 MeV . The (photon,neutron) total cross-section is shown in Equation 1.1[14].

$$\sigma_{tot}(\gamma, n) = \sum_i \sigma_i(\gamma, i) \tag{1.1}$$

Where;

$$\sum_i \sigma_i(\gamma, i) = \sigma(\gamma, n) + \sigma(\gamma, 2n) + \sigma(\gamma, fis) \tag{1.2}$$

The cross-section of ^{232}Th fast fission has a 1 MeV threshold as shown in Figure 1.1, photo-fission cross-section is shown in Figure 1.2, photo-neutron is shown in Figure 1.3, and photo-2 neutrons in Figure 1.4.

Spallation target can be ^{7}Li or ^{9}Be to produce neutrons via (p,n) reactions, ^{7}Li has 1 MeV (p,n) reaction threshold energy and a peak at 2.5 MeV as shown in Figure 1.5, while ^{9}Be has a threshold of 2.2 MeV and a peak at almost 5 MeV as shown in Figure 1.6. Neutrons are not only produced from the lithium target via spallation reaction, different isotopes of lithium have different nucleus

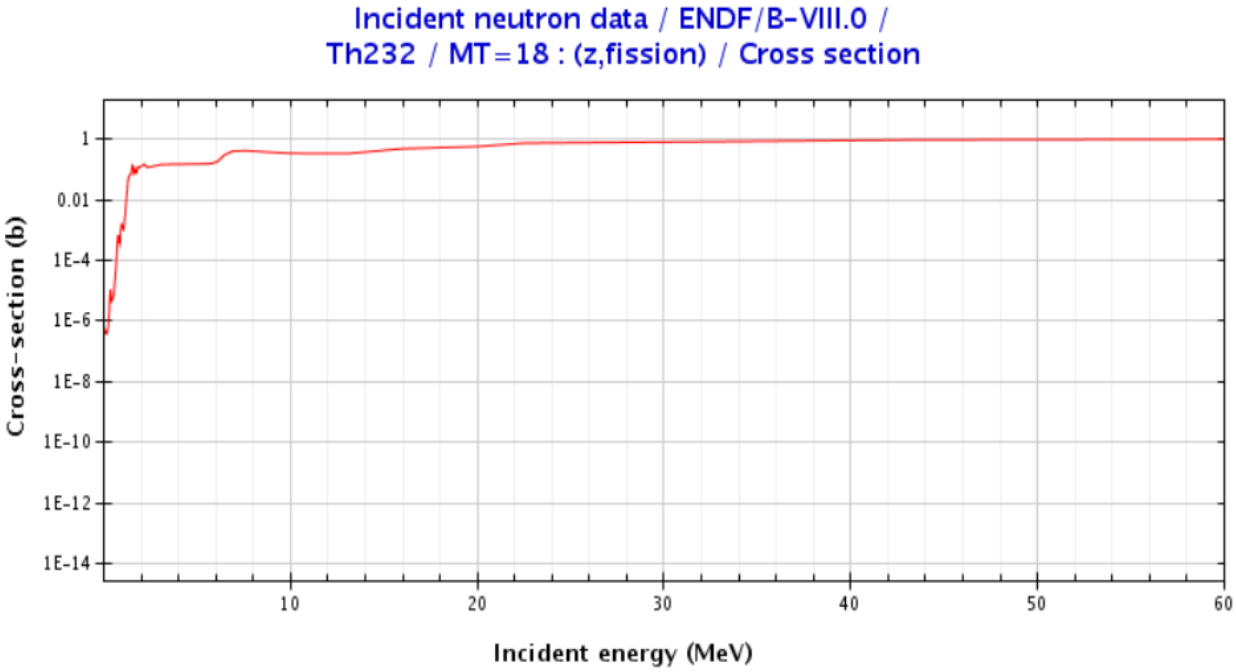

Figure 1.1: Fast fission cross-section ^{232}Th

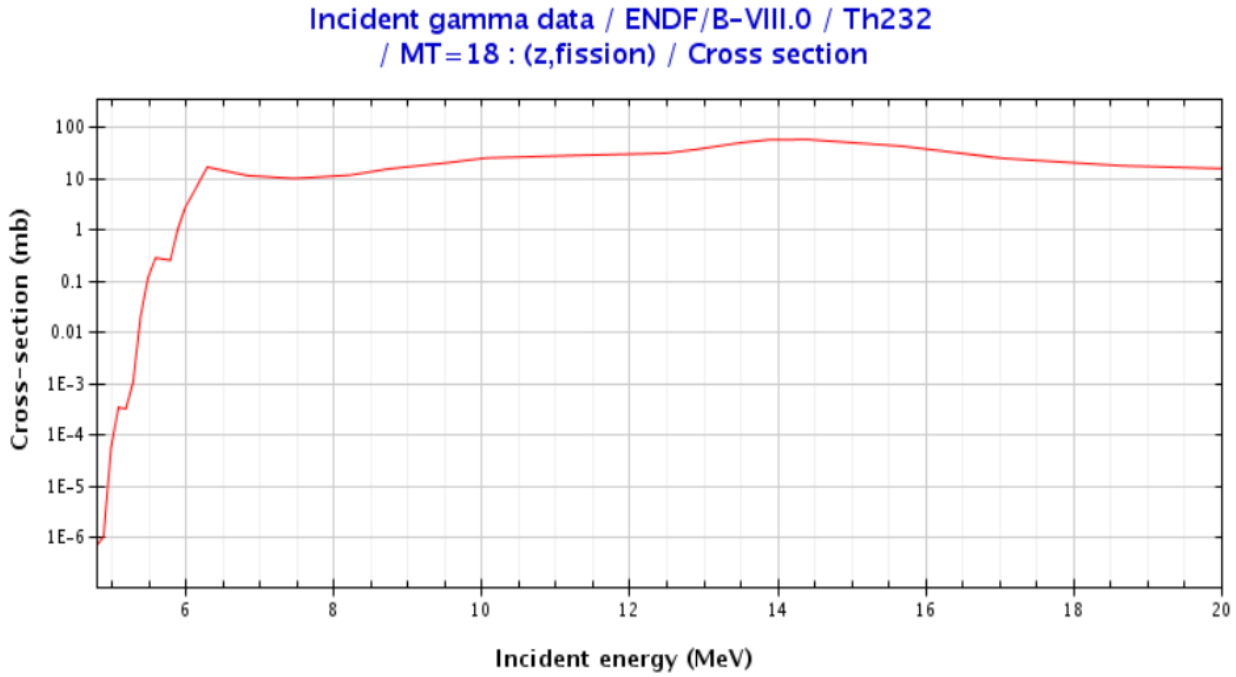

Figure 1.2: Photo fission cross-section ^{232}Th

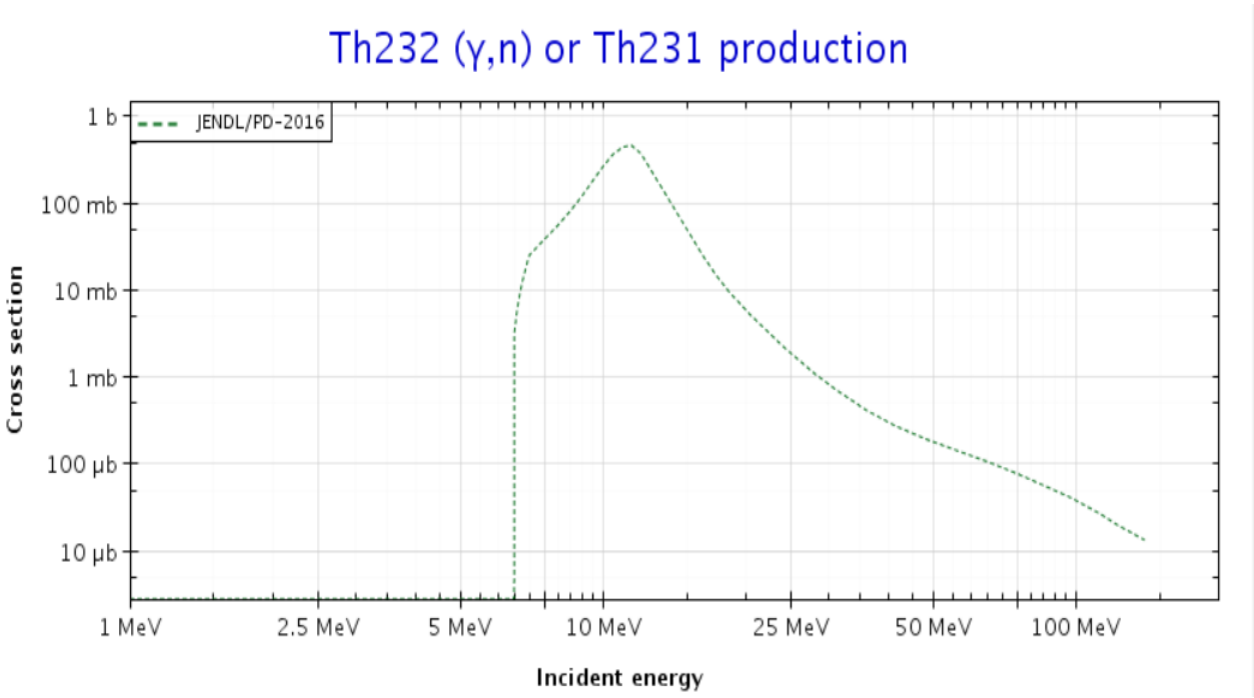

Figure 1.3: Photo neutron cross-section ^{232}Th

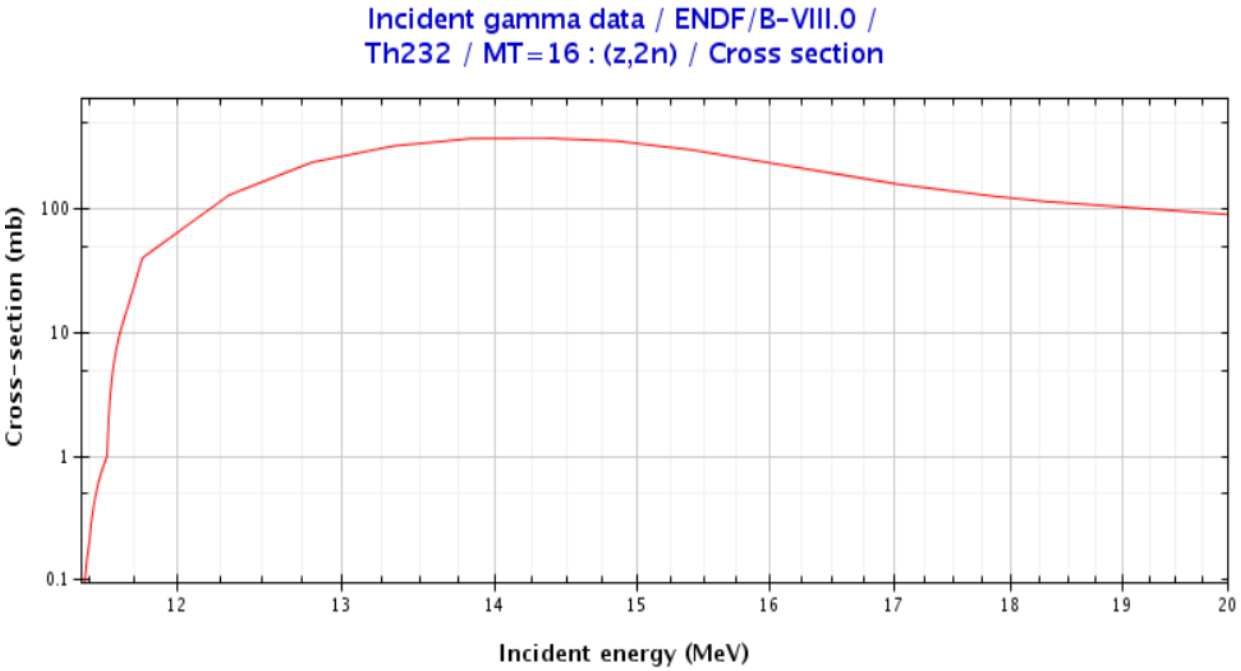

Figure 1.4: Photo 2 neutrons cross-section ^{232}Th

breakup energy threshold with photons that also produce neutrons as shown in Table 1.1 [15].

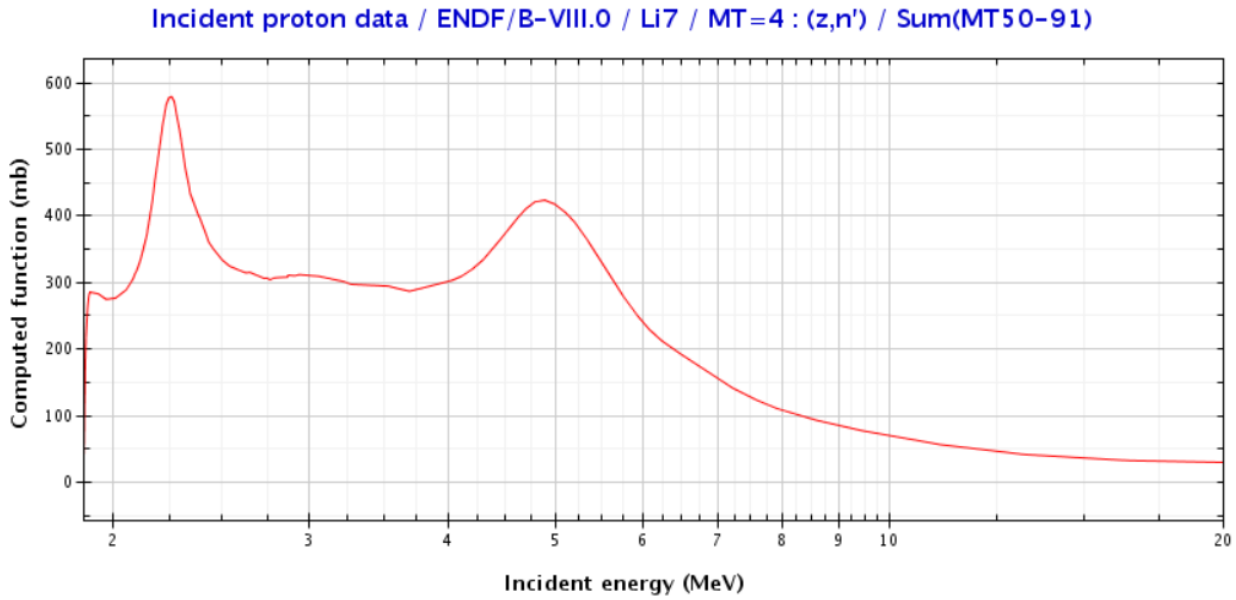

Figure 1.5: ^{7}Li(p,n) spallation reaction cross-section as a function of proton energy

Table 1.1: Lithium isotopes binding energies in MeV

Process	^{6}Li	^{7}Li
(γ,n)	5.43	7.25
(γ,pn)	3.69	11.9
(γ,2n)	————-	12.68
(γ,p2n)	————-	10.95

1.1.5 Facility Description

The accelerator driven thorium-fueled molten salt loop is a thorium-fueled molten salt test loop coupled with a proton accelerator. The facility is located at the Thermal Hydraulics Laboratory of Texas A & M University, it is composed of two sections, the proton beam; which acts as a neutron generator via spallation reactions with a solid target, and the thorium-molten salt test reactor where

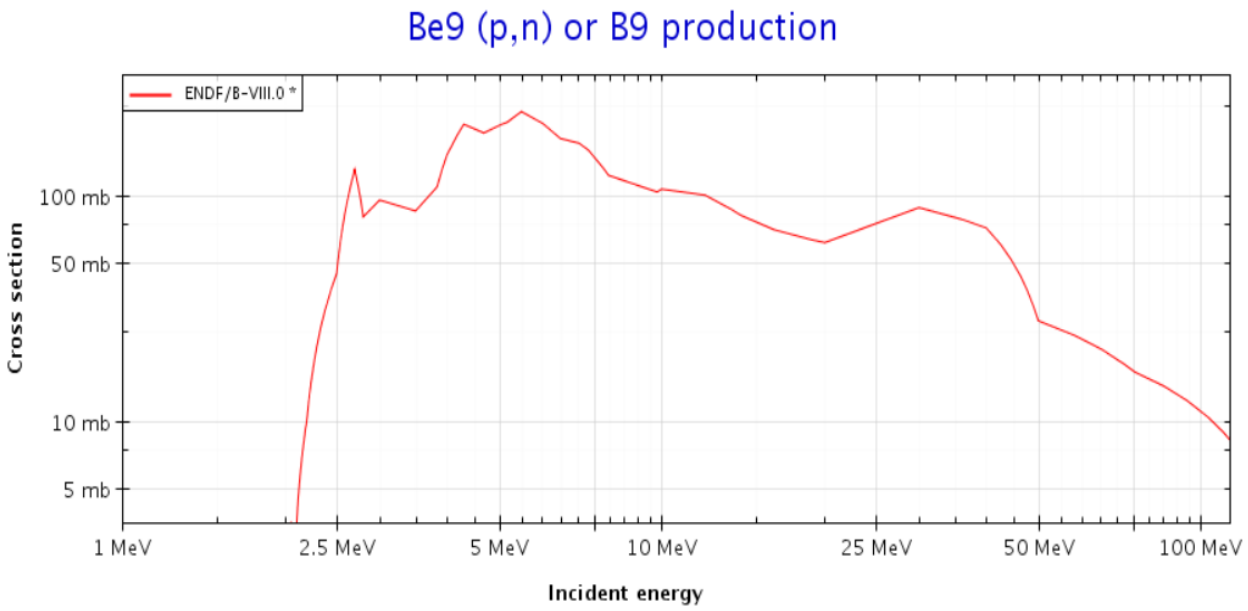

Figure 1.6: ^{9}Be(p,n) spallation reaction cross-section as a function of proton energy

the molten salt is confined in a chamber and flow through the loop piping system. These kind of facilities operate in subcritical mode system, which add inherent safety to perform experiments and studies over the conventional research nuclear reactors.

The facility was built for a couple of purposes: I. Establish a molten salt flow through the test section and impose desired boundary conditions like flow rate and temperature. II. Conduct a feasibility study consisting of an accelerator system to produce neutrons from spallation, and as a result, generate fission events in ^{232}Th within the molten salt environment.

To accomplish this, it is necessary to conduct simulations to design and optimize some of the components of the facility, including spallation target size and location, proton beam parameters, molten salt test section design, and radiation shielding. The facility can operate at high temperatures (>700 $^{\circ}C$), components are corrosion resistant, and has a state of the art instrumentation like ultra-sonic flow meter, optical fiber sensors, and flow visualization.

The proton beam model is 60 cm length void beam, surrounded by a graphite moderator, two elements were suggested as a target to produce (p,n) reactions, these are ^{9}Be, and ^{7}Li. ^{7}Li was selected based on a couple of reasons; it has a lower bombarding proton energy threshold of 1

MeV, and a high neutron yield with a soft energy spectrum relatively, as a result require less moderation. Although lithium has a low melting point, poor thermal conductivity, and reactive metal when exposed to air, the alternative ^{9}Be needs a higher and stronger current accelerator [16]. The lithium target is in a solid phase placed inside the proton beam to generate neutrons, shape and location of the target will be investigated through out the research.

Two molten salt options were also suggested, these are the LiF-BeF_2 (FLiBe) and the LiF-NaF-KF (FLiNaK) salts, due to the high toxicity of the beryllium, the alternative FLiNak molten salt was chosen as a fuel carrier for the loop. Stainless steel 316 alloy was used to build the loop components including the chamber and the piping system.

1.2 Scope And Goal

The scope of this research is to conduct parametric studies and sensitivity analysis using stochastic methods to support the design and optimization of the main components of the accelerator and molten salt test loop system. The examinations are classified under six goals;

1 - Optimize the size and location of the lithium target to maximize the utilization factor of the proton beam.

2 - Optimize the ^{232}Th concentration in the FLiNaK-ThF_4 test section.

3 - Study the possibility of maximizing the fission reactoin rate density in the FLiNaK-ThF_4 test section, and as a result maximize the fission output.

4 - Design and optimize the graphite proton accelerator shielding.

5 - Design and optimize the shielding for the molten salt loop facility.

6 - Perform a benchmark between SERPENT2 and MCNP6 Monte Carlo codes.

2. METHODOLOGY

2.1 Neutron Transport Theory

Neutrons interact with materials via several interactions, these are important in the sense of many purposes; such as detection, shielding, inducing fission, and structural displacement. Microscopic cross section is defined as the probability of a specific interaction to occur between the element nucleus and the neutron, and is a function of the neutron incident energy. Neutron interactions can be categorized under two major classes; these are scattering and absorption, major interactions also break down into minor interactions; elastic scattering and inelastic scattering under the scattering interaction, radiative capture (n,γ) reactions, neutron producing neutrons (n,2n) and (n,3n) reactions, charged particles production (n,p) reactions, (n,alpha) reactions, and fission interactions under the absorption interactions. The microscopic cross section depends on the energy of the incident neutron, the cross section decreases as the energy increases. For heavy nuclei, resonance appears clearly in the eV energy range, but in the KeV energy range these resonance become too close to be be distinguished, and in the higher MeV range resonance become broader and small. However, this is not the case for light nuclei where resonance only appear in the MeV energy range.

2.2 Stochastic And Deterministic Methods

Radiation transport analysis can be applied using two conceptual different approaches, deterministic and stochastic. Stochastic methods (Monte Carlo) apply calculations based on a pseudo random number generator to generate a certain particle history number for the interaction probability. Deterministic approach depends on discretizing the Boltzman transport equation, these methods are considered more efficient for solving differential quantities, while stochastic approach (MC) are more efficient for solving integral quantities. However, Monte Carlo can get very inefficient in case of a small number of particle history contribute into the quantity to be calculated [17].

Unlike the stochastic Monte Carlo method, deterministic codes use approximations and rely on numerical approaches that are valid under certain conditions. The major advantage of the stochastic method over deterministic methods is that it is a problem independent and can be reliable when considering complex geometry such as research reactors. The 3D model is constituents of primitive volumes that are built using surfaces of planes, boxes, sphere, cylinders, hexagons, ellipsoids cones, and polyhedrons that are bounded to form the cell. These cells are then assembled using unions and intersections to form a full detailed geometrical 3D model that considers the heterogeneity. However, Monte Carlo neutron transport codes are considered time-consuming somehow, but with the availability of multi-core computers, simulations can be done in an acceptable period of time.

2.3 Monte Carlo Methods

Neutronics calculations using one of the MC codes usually require validation of the computational model and results bench-marking with another MC code, specially when there is no experimental data like new experiment. These validations usually fall into three categories, reactor operational parameters and data, shielding design, and criticality results benchmark.

A study was conducted by Jakko Lappanen in 2013 provides a methodology using SERPENT2 Monte Carlo code to calculate the delayed neutron fractions and effective generation time. The calculations were determined based on a method introduced before by Nauchi and Kameyama in 2010 and Kiedrowski in 2011, it is called iterated fission probability [18]. The results were compared to MCNP5 simulations and also to experimental results, it included different fissile nuclei and 31 critical configurations. Results were in a good agreement with MCNP5 and the experimental data.

Argon National Laboratory (ANL) has developed a simplified method to perform burn-up analysis using Monte Carlo Reactor Burn-up System (REBUS or MCREB) code [19], which uses the MCNP to calculate the neutron fluxes, reaction cross-section, and multiplication factor, and then data is transferred to another REBUS code for the purpose of power normalization and the buildup of burnt fuel, the REBUS output data is then coupled back to MCNP for post processing.

In 2014, the National Research Nuclear University MEPHI in Moscow, Russia, established a research to study a set of test problems on the 2.5 MW IRT-MEPHI research reactor with a low enriched uranium fuel tube, high enriched uranium fuel tube, light water moderator and a beryllium reflector. The research group used three codes for the calculations and results bench marking, these are, SERPENT2 Monte Carlo code, MCNP with REBUS (or MCREB), and Monte Carlo Universal (MCU-PTR) code [19]. For core design validation, the multiplication factor was calculated for several loading patterns. MCU-PTR code with a Compact ENDF/Monte Carlo Universal (ACE/MCU) data library resulted in a better agreement of the K_{eff} value compared with MCNP.

SERPENT2 and MCNP results provided the same multiplication factor when the same cross-section data library was used. For burn-up calculations, all three codes MCREB, MCU-PTR, and SERPENT2 were in a very good agreement. This study concluded that there are some dissimilarities when considering several code for a test problem calculation, results also depend on the data library selected for each code, implementing the same cross-section data library can reduce dissimilarities. The absence of experimental data could lead researchers to use different tools and codes when performing the calculations, thus, making the obtained results more reliable.

SERPENT2 Monte Carlo code was used to model the Training, Research, Isotopes, General Atomic reactor (TRIGA) research reactor in Slovenia, 2014 [20]. The results of neutron flux and neutron reaction rates of SERPENT2 had a very good agreement with MCNP and the experimental data in the active reactor core area. This study shows that SERPENT2 Monte Carlo code can be used for a well detailed reactor model using materials and detailed configuration. However, in the outside reflector region, there were some discrepancies regarding the very detailed model, but this was neglected because the code is mainly to be model the reactor core region.

The SERPENT and MCNP Monte Carlo code have been used for modeling and simulation purpose of the GIACINT critical experimental facility and YALINA subcritical facility in Belarus [21]. The MCNP model was constructed using combinatorial geometry whereas the SERPENT model was built based on the stereolithography (STL) geometry that a couple of programming languages such as MATLAB, Python, C, and CUBIT [22]. Both codes results were in a very

good agreement for the multiplication factor, combinatorial based geometry in MCNP simulations were faster than the SERPENT STL based model, for this purpose, an adaptive mesh have been introduced to the SERPENT simulations in order to minimize the computation time.

SERPENT2 Monte Carlo code was used to build a new reactor model for the TRIGA in Vienna, neutron fluxes and burn-up calculations were implemented [23]. The results were bench-marked with the MCNP6 and experimental results, neutron fluxe in different core positions along horizontal and vertical axis were tallied. SERPENT2 and MCNP6 flux results were on a very good agreement with a difference below 10%, and below 5% for burn-up calculation inside the reactor core.

MCNP and SERPEN+NESTLE (Nodal Kinetics code for Steady-state and Transient Reactor Neutronics) combination codes were used to benchmark results in a hot zero power calculations of the Temelin VVER 1000 in the Czech Technical University (CTU) in Prague [24]. Study included multiplication factor and Moderator Temperature Coefficients (MTC). The multiplication factor resulted in a very good agreement between the two codes, and compared to the experimental results, and a reasonable agreement of the MTC values.

From literature, it is clear that using SERPENT & MCNP codes for validation and results bench marking have gained a great interest in the nuclear computational community and nuclear design, both when the experimental data exist and does not exist. This does not only serve as a strong base for the code developers and users about the fidelity and validity of their code, but also can drive researchers interest and attention toward new developments which make these codes more promising in the future.

2.4 Fundamentals of Monte Carlo Particle Transport

Monte Carlo methods follow two approaches to solve the particle transport equation, a mathematical approach; which is useful for importance sampling, variance reduction and eigenvalue problems. The second is the computer simulation which is useful for collision physics, tracking, and tallying. Monte Carlo uses the time-independent Boltzmann transport equation that is shown in Equation 2.1 [25].

$$\Psi(r,v) = \int \left[\int \psi(r',v') C(v' \rightarrow v, r') dv' + Q(r',v) \right] T(r' \rightarrow r, v) dr' \tag{2.1}$$

Where;

$\Psi(r,v)$ = particle collision rate density.

$Q(r',v)$ = source term.

$C(v' \rightarrow v, r')$ = collision kernel, change velocity at fixed position.

$T(r' \rightarrow r, v)$ = transport kernel, change position at fixed velocity.

Angular flux is defined as in Equation 2.2 [25].

$$\Psi(r,v) = \frac{\Psi(r,v)}{\Sigma(r,|v|)} \tag{2.2}$$

Scalar flux is shown in Equation 2.3.

$$\phi(r,|v|) = \int_{\vec{\Omega}} \frac{\psi(r,v)}{\sum(r,|v|)} d\vec{\Omega} \tag{2.3}$$

Monte Carlo methods display some assumptions simultaneously when simulating particle tracking and interactions [25] such as:

1- The medium is static and and homogeneous.

2- Relativistic effects, and long range forces.

3- Neglect the particle-particle interaction.

4- The next event depends on the current not on the previous event.

5- Particles reactions do not effect the materials and it's properties.

The basis of Monte Carlo methods is shown below [25].

Let

$p = (\vec{r}, \vec{v})$ and,

$R(p' \rightarrow p) = C(v' \rightarrow v, r').T(r' \rightarrow r, v)$.

Expand Ψ into components;

$$\Psi(p) = \sum_{k=0}^{\infty} \Psi_k(p), \tag{2.4}$$

and;

$$\Psi_0(p) = \int Q(r', v) T(r' \to r, v) dr' \tag{2.5}$$

By definition;

$$\Psi_k(p) = \int \Psi_{k-1}(p').R(p' \to p) dp' \tag{2.6}$$

Collision type k depends on the collision before k, which is k-1, histories are simulated as follow;

$$\Psi_k(p) = \int \Psi_{k-1}(p').R(p' \to p) dp' \tag{2.7}$$

And a graphical sketch to present how Monte Carlo methods simulate and track histories, where one history is the sequence of interactions for the same particle as shown in Figure 2.1.

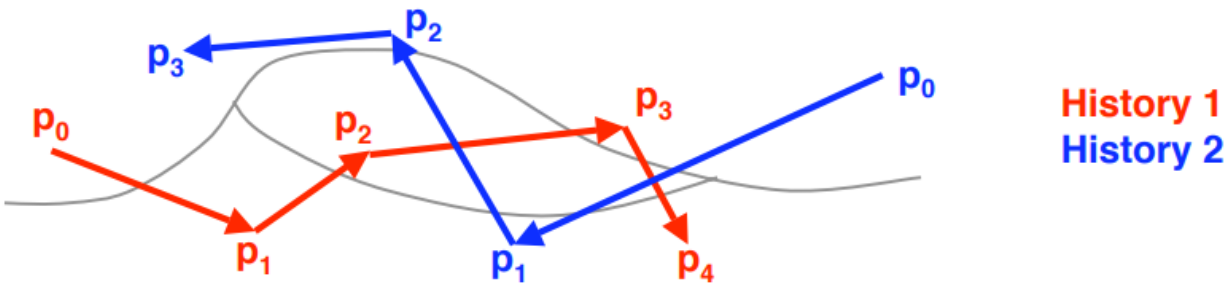

Figure 2.1: Particle histories by Monte Carlo methods
[25]

Finally;

$$\Psi_k(p) = \int ... \int \Psi_0(p_0).R(p_0 \rightarrow p_1)...R(p_{k-1} \rightarrow p)...dp_{k-1} \tag{2.8}$$

Monte Carlo simulate the single particle history from birth to death, it follows the random-walk principle, where it models the collisions using cross-section data, a free-flight between collisions, encounter for any secondary particles, analyze them, and tally the events in each region. A single particle tracking follows the random walk for particle history, where the code simulate the events with a particle from birth to death, and tallies are used to detect events of interest, on the other side, simulating a batch of histories is tracking a random walk for many particle histories, thus, tallying the aggregate behavior. Over all, Monte Carlo methods proceed with time steps and account for geometry and material changes (burn-up), such as burnable absorber, control rods, and fuel depletion.

2.5 Tools

Monte Carlo N-Particle Transport (MCNP6) code was used to run the simulations, MCNP code is easy to use and has a versatile features like external source definition, surface source, volumetric source, and criticality source. It also has a graphical user interface, where the user can visualize the the geometry, and plot the tally output, for example; the particle flux. It also contains a lot of flexible tallies that can be used for different purposes, such as point detectors, surface detectors, volume detectors, dose function, and mesh tallies. However, because there are no experimental results so far, it is important to benchmark the results using other Monte Carlo (MC) transport code. For this purpose, SERPENT2 Monte Carlo code was used, it is very similar to MCNP, similar syntax, easy to used, and both codes are used to perform results benchmark worldwide.

Because SERPENT2 - which is the latest code version - does not support proton particles, the proton source was converted to an equivalent neutron source. This was done by running a bare case geometry in MCNP6, including a proton source and solid lithium target. Protons are bombarded to a ^{7}Li target producing neutrons. The neutron energy spectrum generated "energy-weighted neutron yield" was extracted from the MCNP6 output and converted into a continuous

energy neutron source in SERPENT2, the neutron flux for each energy bin is normalized to get the probability for each energy group, and this weighted source configuration was used as an input of SERPENT2 input deck as a proton equivalent source.

MCNP6 simulations were run with both proton and neutron source, SERPENT2 was run only with a neutron source and results were compared. The research flow is based on the sensitivity analysis approach, where each phase aims to study the impact of a certain factor, material, or design of one component, to reach the optimal value.

2.5.1 MCNP6 Code

Monte Carlo N-Particle Transport Code (MCNP) is a MCNP is a general-purpose, continuous-energy, generalized-geometry, time-dependent, coupled neutron/photon/electron Monte Carlo transport code [26] over a wide particle energy range. MCNP has many nuclear applications that are used worldwide and continuously developing, such as reactor design, accelerator radiography and topography, medical physics, accelerator target spallation design, accelerator component activation, shielding design and detection technology, high energy dose calculation, accelerator-driven energy source, cosmic ray radiation investigation, nuclear security and safeguards, charged particle propulsion, transmutation and many more applications. The MCNP input file usually contains the problem set up and parameters that are divided into cards, and each card is specialized in describing some sort of information, such as the geometry, materials cross-sections data library, the source particle specification, desired tallies and any extra accuracy techniques like variance reduction techniques, there are 4 versions of MCNP, these are, MCNP4, MCNP5, MCNPX, and the latest MCNP6.

MCNP5 is a general-purpose Monte Carlo N-Particle Transport Code that can be sued for neutrons, protons, electrons, or coupled neutron/photon/electron transport, including the capability to calculate the Eigenvalue values for critical systems [27]. MCNPX is a Monte Carlo N-Particle Extended code that transport many particles over a broad range of energies. MCNP6 version has developed capabilities and features combined from the MCNP5 and MCNPX older versions. MCNP6 supports many particle types like neutrons, photons, and electrons that are supported by

MCNP5 and MCNPX,it also supports an extra of 30 particle types such as protons, positrons, pions, sigmas and muons, heavy ions like deuterons, tritons, helions, and alphas. On The Fly Doppler broadening, particle transport in unstructured mesh, Cerenkov photon production, light ion transport, correlated decay particle production, and correlated prompt particle production are also developments that have been published with MCNP6 version. All versions of MCNP can build a very detailed geometry and physical model, perform calculations on any physical quantity, unique features of criticality calculations and support an extensive V& V against experiment.

2.5.2 SERPENT2 Code

SERPENT Monte Carlo stochastic neutron transport code is a 3-D continuous energy reactor physics burn-up code, it was developed by the VTT Technical Research Center of Finland in 2004 [28]. SERPENT1 is not an open-source code but distributed through the Organization for Economic Co-operation and Development as a part of the Nuclear Energy Agency (OECD/NEA) data bank and the Radiation Safety Information Computational Center (RSICC) since 2009 [28]. SERPENT2 version has an an extra capabilities exceeding reactor modeling, these are, multi-physics simulation like coupled calculations with thermal hydraulics or Computational Fluid Dynamics (CFD), and dose rate calculations, fusion, shielding, or medical physics.

SERPENT2 is available to registered users only upon request from the code developer. SERPENT2 is widely used for 3 purposes, radiation shielding, radiation detection, and to validate the deterministic neutron transport codes. When the deterministic methods are hard to apply, stochastic methods are usually applied instead. Moreover, the stochastic methods have some inherent randomness unlike deterministic where the output is fully determined by initial conditions.

SERPENT2 has various reactor analysis capabilities that can be utilized, like generating group constants, the capability to adapt to geometry complexity and reactor physics without major approximations, the code can be used to model any reactor type and any fuel configurations. However, Monte Carlo stochastic methods face some computational challenges time-wise, burn-up calculations are slower and can take days when compared with deterministic codes.

SERPENT2 Monte Carlo code does not only address the group constant generation and burn-

up calculations, but also external source simulations and reaction rate calculation. The SERPENT2 code has two applications for typical users: research reactor modeling, where the simulations serve as a full-scale problem solution, and the group constants generation where the simulation outputs serve as a source for the deterministic input. For burn-up calculations, the user has to define the burnable isotopes and material, then, the code produce the fission products and daughter nuclides automatically.

2.5.3 Nuclear Data

Three main energy regions exist for neutron cross sections data, the resolved region, unresolved region, and high energy range. Each measurement generate a different type of data, cross sections are independently measured, data obtained also include some related parameters such as finite temperature, finite size of a sample, and a finite resolution. Many advantages arise from evaluated data that participate in the theoretical understanding of cross sections behavior, and determining all available uncertainties for experimental data; like the cross section shapes and the relationships for different reactions. The evaluated data also allows temperature, energy, and reactions extrapolation. For simulations, MCNP code provide the definition of materials, atomic or weight density, and composition in the material data card, MCNP uses the Evaluated Nuclear Data Library (ENDF) as a data library source. The data library version used in this research for this MCNP model is ENDF/B-7, ENDF provides neutron data, decay data, covariance data, thermal scattering data, proton data, triton data, deutron data, atomic data and photonuclear data. SERPENT Monte Carlo code can uses both EDNF and the Joint Evaluated Fission and Fusion (JEFF) data library, but libraries have to be converted from -xsdata to -xsdir extension, the data library used in this research for the SERPENT2 model is the JEFF3.1.1 version.

3. RESULTS

3.1 MCNP6 Simulation Results

Simulations were run depending on the sensitivity analysis approach, all simulations were divided into phases; each phase aims to study a specific factor of the facility design as shown in Table 3.1. The old version MCNP5 does not support protons, a more recent version MCNPX does not support the FMESH tally, and the last distributed upon request version MCNP6 support both. For these reasons, at the early stages of research, when the MCNP6 license was not obtained yet, it was not convenient to go back and forth between MCNP5 and MCNPX taking the advantage of each version capabilities, once the license was obtained, all simulations were done using the last updated version MCNP6 through the inspect of ORNL cluster.

Table 3.1: MCNP phases

Phase	Goal
Phase 1	Optimization of the proton beam graphite shielding design
Phase 2	Proton source current and energy impact on the neutron generation via spallation
Phase 3	Adding FLiNaK-ThF_4 test section to simualtions
Phase 4	Effect of lithium target presence on thorium fission rate density
Phase 5	Comparison between proton source and equivalent neutron source
Phase 6	Optimization of thorium fraction to maximize the fission rate density
Phase 7	Target thickness and location impact on neutron flux inside test section
Phase 8	Optimization of lithium target thickness and location
Phase 9	Selection of material composition for the loop shielding
Phase 10	Optimization of the loop shielding design

3.1.1 Phase 1

Different initial cases were run to study, understand, and build an image about the problem setup, geometry design of the proton beam, and the source parameters. This phase included six cases as shown in Table 3.2. A 3D model of the proton beam was modeled ,a graphite cylinder surrounding the accelerator for shielding purposes, Figure 3.1 shows the initial geometry set up for graphite shielding, proton source, and the lithium target. Eleven detectors have been placed along and normal to the proton beam center line, lithium target is placed at the center of the void beam with 0.2 mm thickness, and a sphere of 80 cm radius filled with air surrounds the proton beam.

Table 3.2: Phase 1 cases

	Source configuration	Source position (cm)	Source anglular specification	Source weight	Source particle	Source energy (MeV)
Case 1	Volumetric	Distributed	-	0	Protons	3
Case 2	Circular disc (r = 1.27 cm)	-29.9	Mono-directional	0	Protons	3
Case 3	Square disc (0.6*0.6 cm)	-29.9	Isotropic	6.2410e+12 P/s $\sim 1\mu Amps$	Protons	3
Case 4	Square disc (0.6*0.6 cm)	-29.9	Mono-directional	6.2410e+12 P/s $\sim 1\mu Amps$	Protons	3
Case 5	Square disc (0.6*0.6 cm)	-29.9	Isotropic	12.48+12 P/s $\sim 2\mu Amps$	Protons	3
Case 6	Square disc (0.6*0.6 cm)	-29.9	Mono-directional	12.48+12e+12 P/s $\sim 2\mu Amps$	Protons	3

External source is defined as a square surface source with dimensions of $0.6 * 0.6 cm^2$, the beam is 1.27 cm radius, and 60 cm length, the proton disc source (aperture) and is placed at the beginning of the beam (at Z = -29.9 cm in the simulations). This configuration is to describe the squared aperture geometry of the proton accelerator facility. The beam is a void cylinder with a radius of 1.27 cm, source strength can be increased from 1 $\mu Amps$ to 2 $\mu Amps$, as current increases with a certain factor,generated neutron population increases with the same factor (relationship is

linearly proportional between source strength and generated neutron population). However, the 2 $\mu Amps$ will be the proton source strength used in the rest of simulations. For the source energy, 3 MeV was tested in this phase, but there is a capacity for the energy to be increased from 3 to a maximum of 4.5 MeV. Regarding angular preference, cases in this phase also aim to study the directional preference of the proton source assuming both isotropic and mono-directional , of course, the facility is a linear proton beam.

Hence, a mono-directional angular preference was applied for the proton source. This phase also covered the graphite shielding thickness sensitivity analysis, radii tested are 6.5 cm, 13 cm, 26.27 cm, 30 cm, 35 cm, 40 cm, 45 cm, 50 cm, 55 cm, 60 cm, and 65 cm to obtain the optimum graphite shielding thickness with the minimum cost. FMESH tally was used to visualize the neutron flux and proton particles in the geometry, F4 tally was used to calculate the average neutron flux in the detectors placed at different locations, F2 tally was used to detect the average neutron flux at two surfaces; first is at the varying surface of the graphite shield, and second is a fixed cylinder surface at radius of 26.27 cm radius. The code only calculates the side area of the cylinder surface neglecting top and bottom faces. The full analytically calculated surface area, and the surface area calculated by the code are shown in Table 3.3 and in Table 3.4, respectively.

Table 3.3: Analytical full surface area

Graphite radius (cm)	65	60	26.27	13	6.5
Surface area (cm^2)	51050	45239	14239	5961	2715

Table 3.4: MCNP code cylindrical area

Graphite radius (cm)	65	60	26.27	13	6.5
Surface area (cm^2)	24504	22619	9903	4900	2450

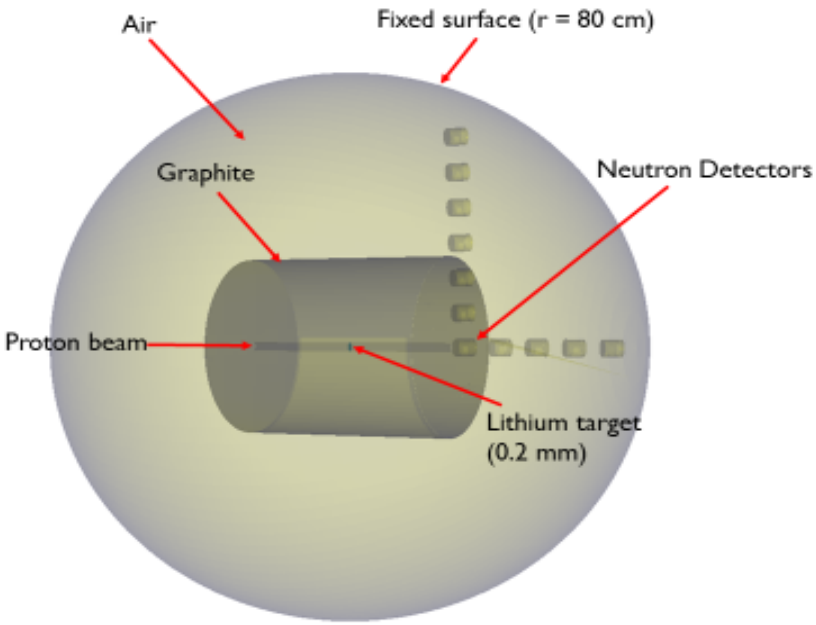

Figure 3.1: 3D MCNP model for neutron detectors

3.1.1.1 Case 1 Results

Neutron flux in unit of ($neutrons/cm^2.s$) was calculated for case 1 at two different surfaces, a fixed surface with radius of 26.27 cm, and a varying graphite surface (as the graphite shielding thickness varies) at four values, these are 0 (no shielding), 6.5 cm, 13 cm, and 26.27 cm. Figure 3.2 shows the neutron energy spectrum at a fixed surface, Figure 3.3 shows the neutron energy spectrum at the varying graphite surface. Here, the source is defined as a cylinder volumetric distributed at the lower part of the void proton beam, with 3 MeV energy and 1.27 cm radius.

Figure 3.4 shows the integrated neutron flux at the fixed, and varying surface, it is expected that as the graphite shielding radius increases, the surface neutron flux decreases, and this is shown below. However, for the fixed surface case at 26.27 cm, the behavior is different, neutrons leak from the void proton beam in different directions and may never reach the surface of the tally.

When MCNP6 detects neutrons at a fixed surface, it only accounts for neutrons that reach the pre-defined surface. Hence, as the graphite thickness increases, neutron scattering toward the defined surface increases, so that more neutrons make it to the surface tally. This is the behaviour

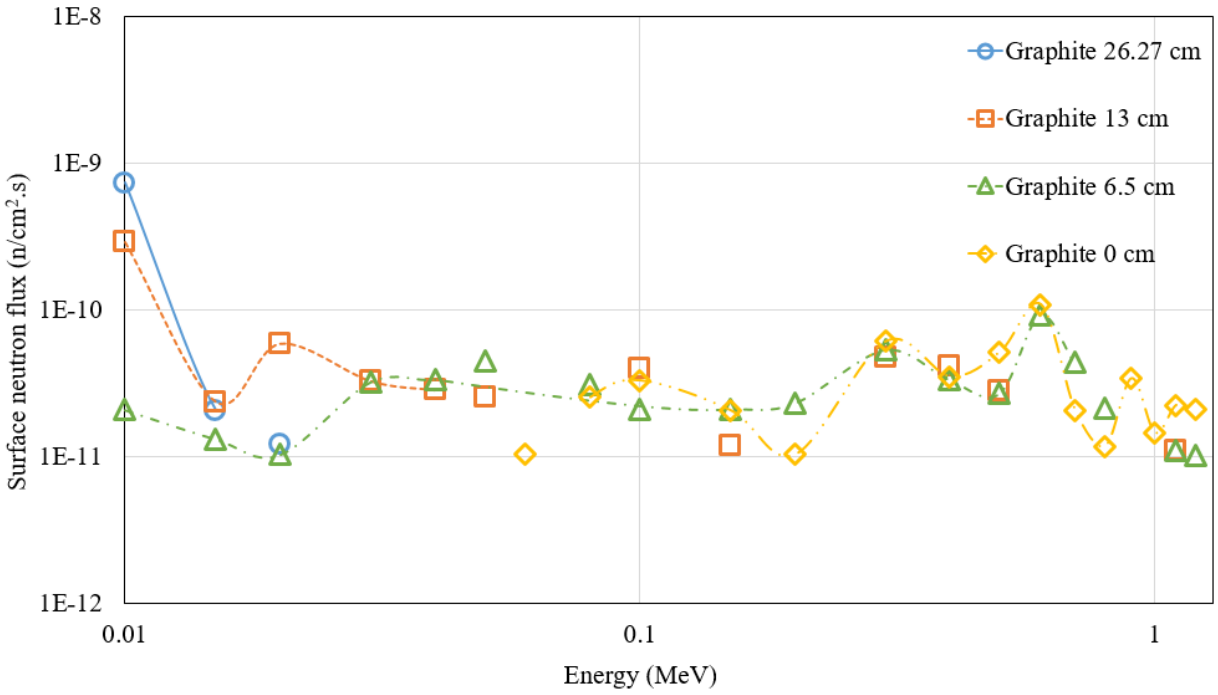

Figure 3.2: Neutron energy spectrum at a fixed surface (26.27 cm) with volumetric source

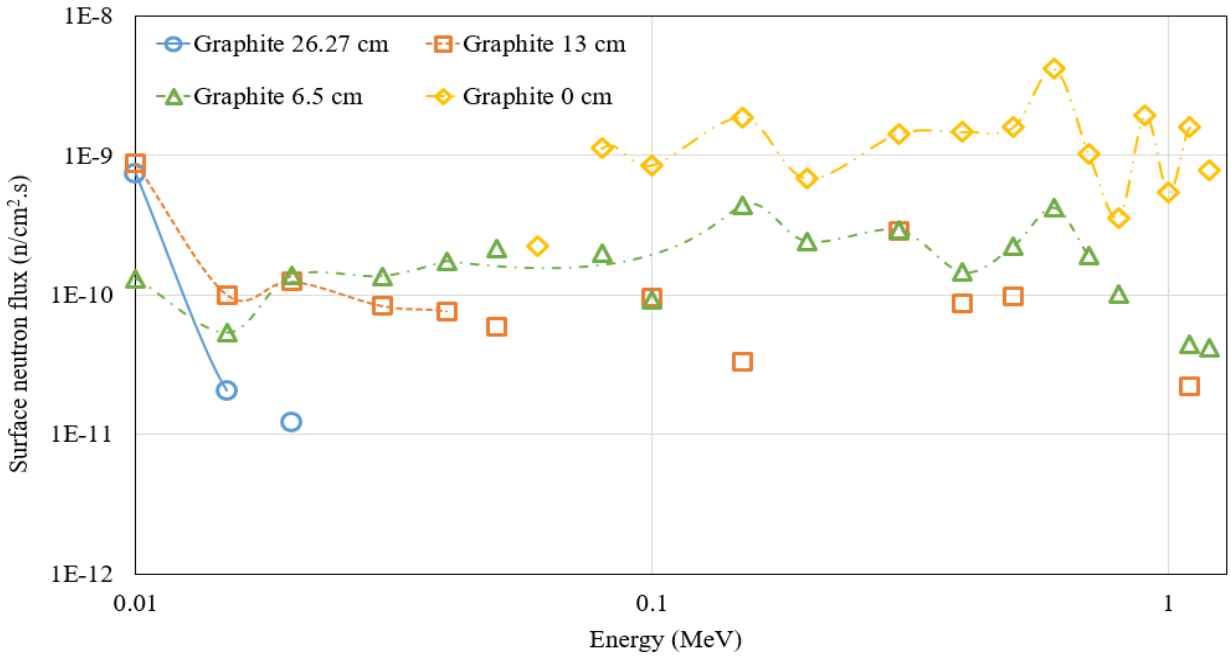

Figure 3.3: Neutron energy spectrum at the varying graphite surface with volumetric source

when tallying over a fixed surface regardless the external source definition, because this is the technique that MCNP6 code follow for the surface flux tally (F2). It has to be noted that fluxes are in order between 10^{-10} and 10^{-7}, this is because the source strength ($neutrons/s$) is not applied yet, the code assume a default value which is $1 neutron/sec$, and the energy is defined as 3 MeV.

3.1.1.2 Case 2 Results

Source was defined for this this case as a mono-directional circular surface source, with a radius of 1.27 cm, the same radius as the proton beam, with the default source strength, Figure 3.5 shows the fixed surface neutron spectrum.

Figure 3.6 shows the surface neutron spectrum at the varying graphite radii. When comparing these results to the previous case, it is noticed that case 2 has larger and more continuous fluxes throughout the energy bins.

As shown in Figure 3.7, the integrated surface neutron flux for the source is slightly larger in order of 10^2 than the integrated neutron flux for the volumetric source. This is because the angular specification force all the proton particles to move in one direction, which results in more

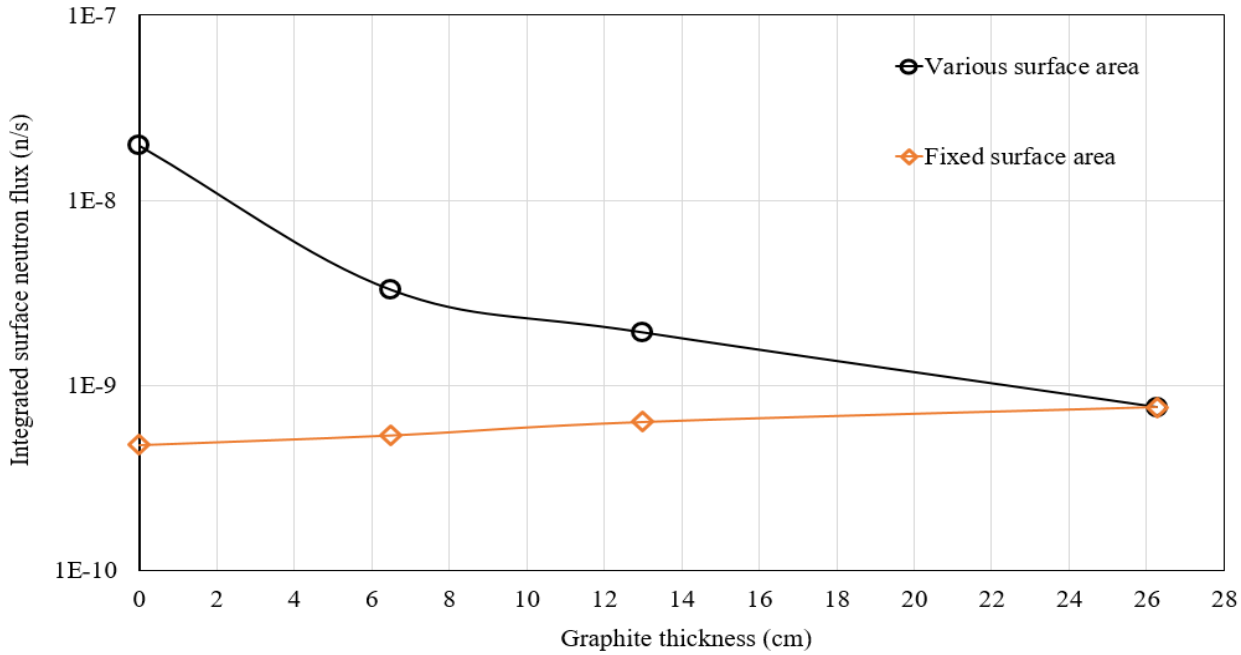

Figure 3.4: Integrated neutron flux as a function of graphite thickness with volumetric source

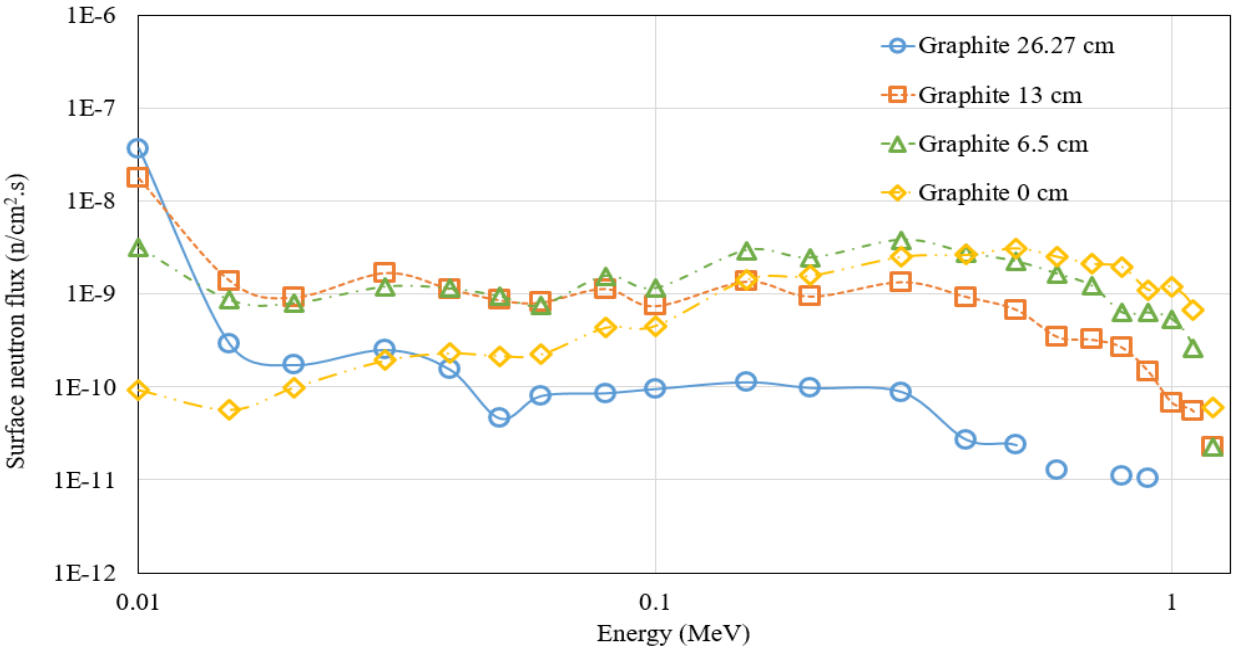

Figure 3.5: Neutron energy spectrum at a fixed surface (26.27 cm) with surface source

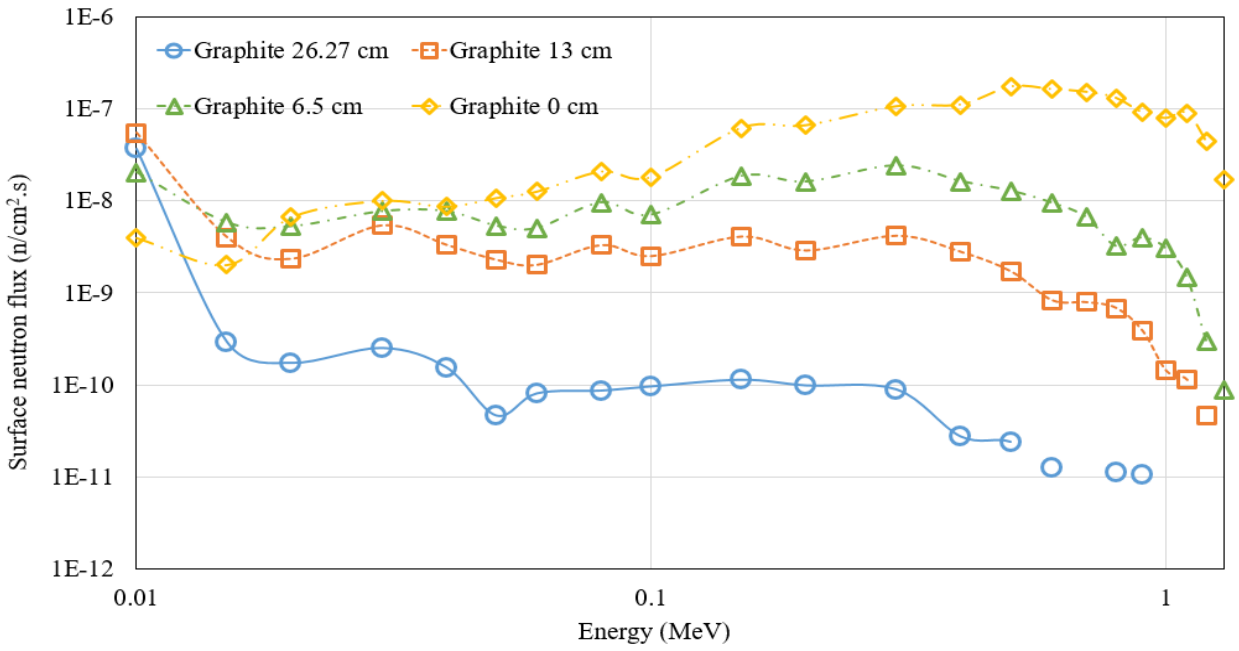

Figure 3.6: Neutron energy spectrum at the varying graphite surface with surface source

spallation reactions, and as a result, larger neutron flux. Proton disc source for this case is shown in Figure 3.8, the red dots denote the proton source particles defined as a surface source, located at the bottom face of the proton beam, and the blue dots denote the neutrons generated via spallation in the upper part of the void beam.

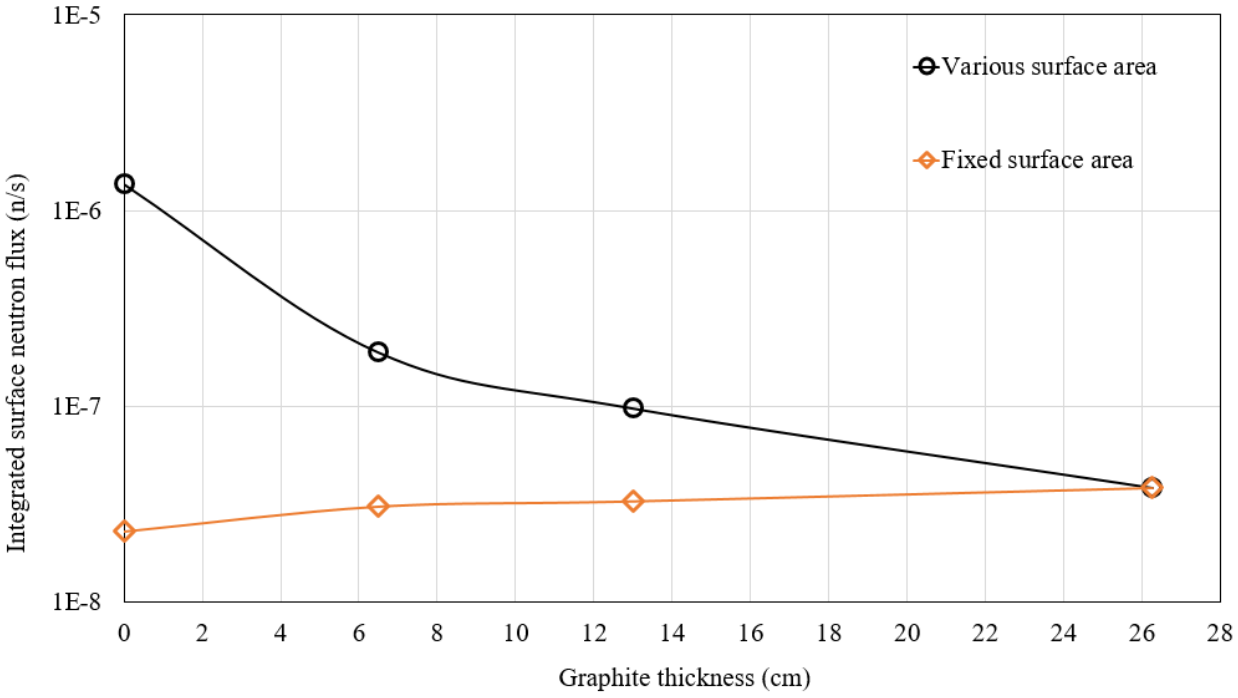

Figure 3.7: Integrated neutron flux as a function of graphite thickness with surface source

3.1.1.3 Cases 3, 4, 5, and 6 Results

After selecting a surface source geometry for proton beam that gives a continuous energy neutron flux, the neutron flux will be tallied at the surface of the graphite shielding as it changes. The proton source at the facility is described earlier as 6*6 mm^2 squared aperture, a sensitivity of the source strength and the angular preference was performed. Two source strengths were tested, these are 1 μ Amps which is equivalent to 6.2410E+12 $protons/s$, and 2 μ Amps which is equivalent to 12.48E+12 $protons/s$. Also, two source angular specifications were tested, isotropic surface proton source, and a mono-directional surface proton source. A comparison between the two source

strengths was done to investigate the effect on neutron flux at the graphite surface, this is shown in Figure 3.9.

It is clear in the figure shown above that the neutron flux at 2 $\mu Amps$ is twice as at 1 $\mu Amps$ with the smallest graphite size, the neutron flux difference between the two currents decrease as the graphite thickness increase, at a sufficient graphite thickness, the neutron flux get fixed and independant on the source current anymore. Figure 3.10 shows the angular distribution effect on the flux as a function of graphite thickness. The two angular specifications have a minimal gap at the minimum graphite shield, but overlap as the thickness increases. This small difference is due the mono-directionality of the proton particles, which minimize the leakage phenomena that is more dominant for the isotropic source, as a result, more neutron are produce via spallation. The rest of the research will investigate more about the source strength, it should be noted that simulations in this case were run with a mono-energetic source of 3 MeV. At this stage, previous simulations resulted in some conclusions that are used in the next simulations; the source should be defined as a square surface source, mono-energetic, and mono-directional subjected to the lithium target, so

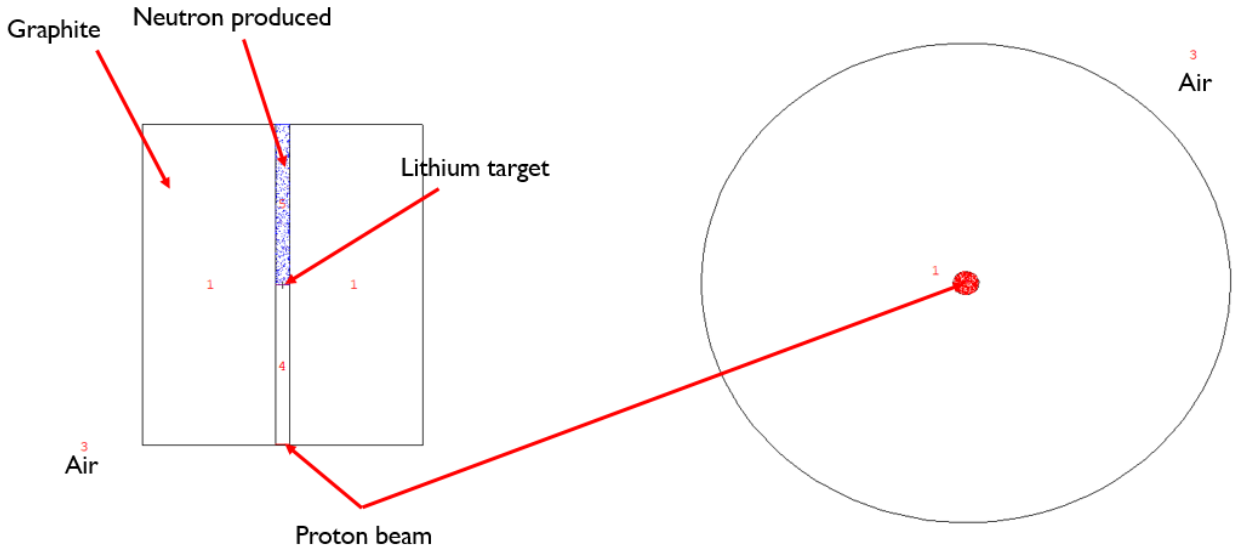

Figure 3.8: MCNP6 2D model for the proton beam, the proton circular disc source, the lithium target, the graphite shield, and the neutrons produced

it simulate the real physical configuration of the proton accelerator aperture at the lab.

The neutron flux was calculated at the graphite surface for 6 graphite thicknesses in this case. It was expected that the optimum graphite thickness would be at radius of 26.27 cm (about 10.5 in), so half of this value, quarter of this value, and two more values were tested as shown in Figure 3.11.

The lithium target is located at the center of the proton beam (Z = 0 cm in simulations) so far, another sensitivity analysis will be done in this regard later. Figure 3.11 shows some discontinuities starting to show up at the 13 cm radius, this is because some of the neutrons generated at higher energies are slowed down to a lower energies. The max energy is 1.2 MeV at 13 cm, while is is 1.3 MeV at 6.5 cm thickness. The case where the radius is 26.27 cm, it is shown that the maximum neutron energy s less than 1 MeV, and for the thicker graphite at 60 cm and 65 cm, it is shown that all neutrons are slowed down to 10^{-2} MeV, so these thicknesses show the minimum neutron energy values.

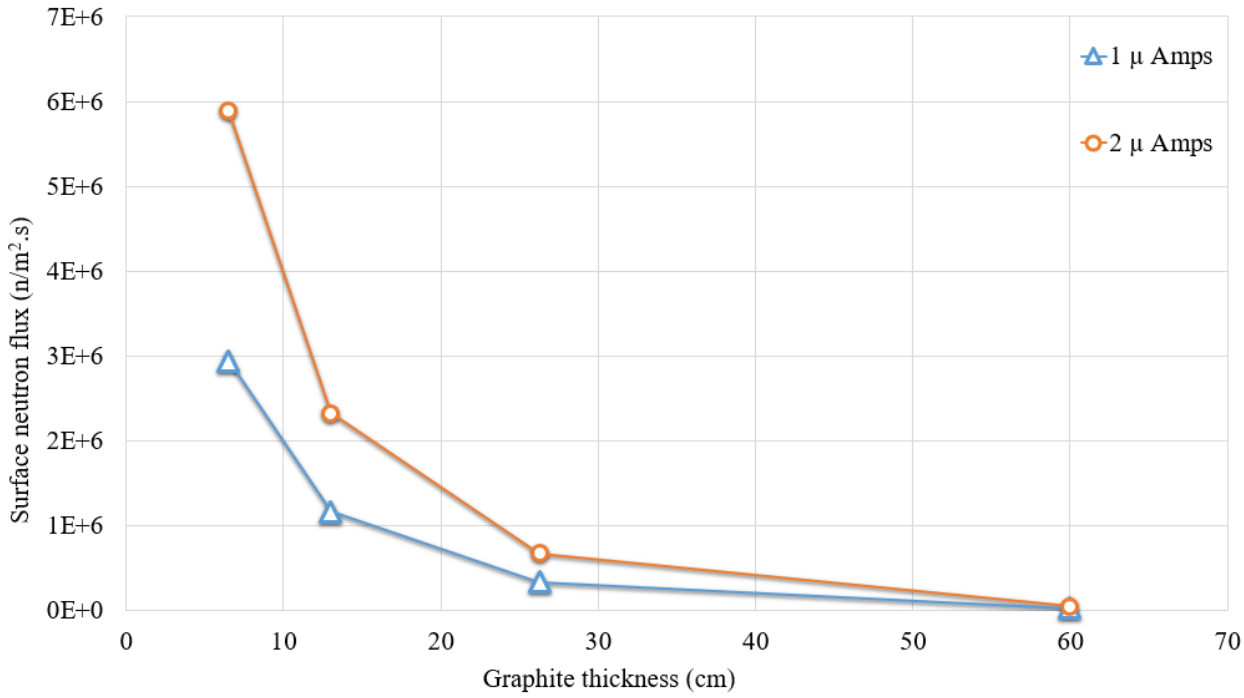

Figure 3.9: Two source strengths impact on the surface neutron flux as a function of graphite thickness

It should be mentioned that for all of the simulations, the proton beam is 60 cm starting at Z = -30 cm to Z = 30 cm in the simulations, the source was located at the beginning of the proton beam, which is Z = -29.9 cm. In Figure 3.12 below, F2 tally was used to calculate the surface neutron flux in unit of $neutrons/cm^2.s$ at the graphite surface. A large cylinder detector was placed in front of the proton beam to detect the neutron flux leak. The MCNP6 model is shown in Figure 3.12, the red cell denotes the graphite shield surrounding the void proton beam, the large cell in front of the beam denotes a cylindrical detector filled with air (yellow), and the sphere is the outer air atmosphere (yellow). FMESH tally was used for this purpose in units of ($neutrons/cm^2.s$).

Figure 3.13 shows a contour plots for five graphite thicknesses, FMESH tally takes a form in the Cartesian coordinates, where four points were taken horizontally, starting at X = -100 cm and ending at X = 100 cm, 100 points vertically, starting at Z = 2.15 cm (2.14 cm away from the lithium target) and ending at Z = 427.85 cm.

As shown below, in the range between Z = 2.15 cm and Z = 60 cm (which is the end of the

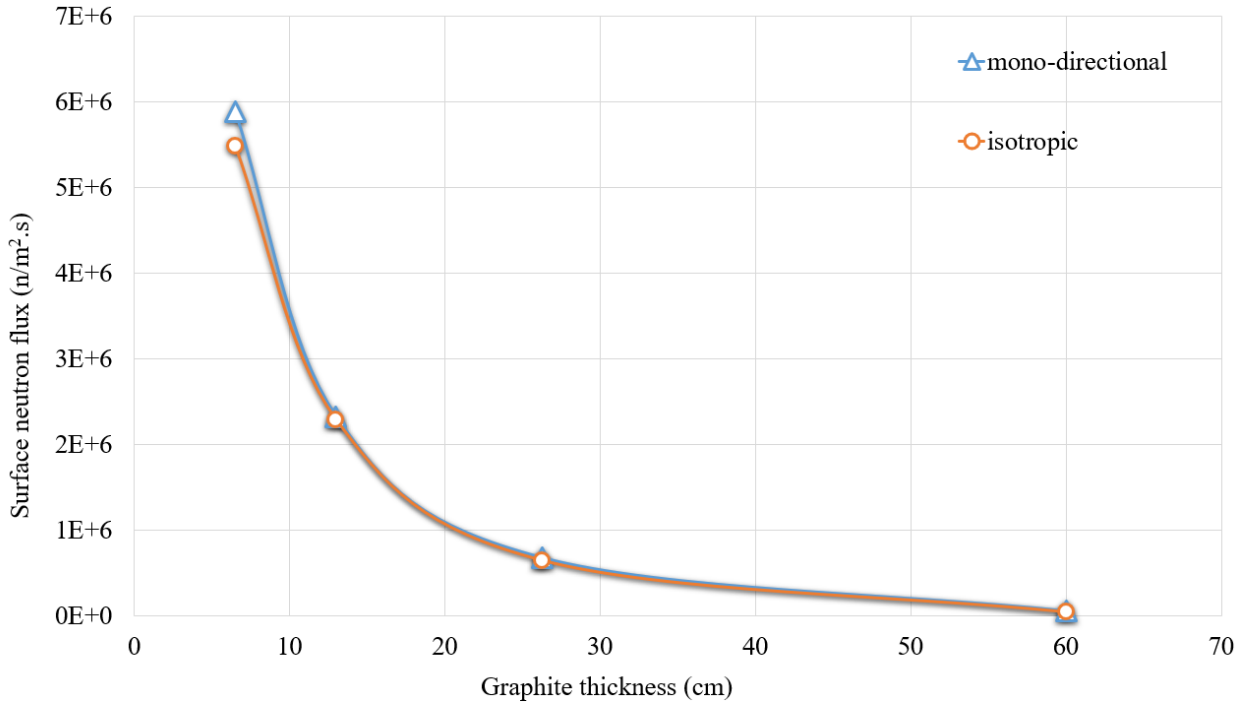

Figure 3.10: Angular specification impact on the surface neutron flux as a functions of graphite thickness

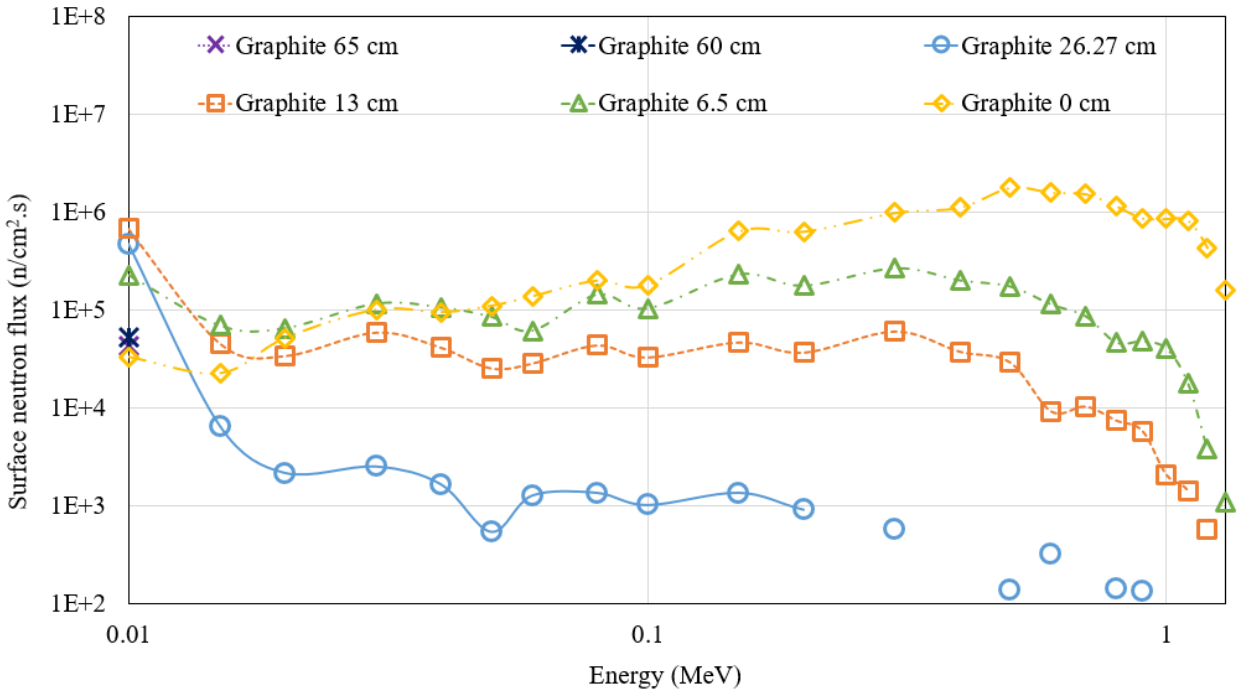

Figure 3.11: Neutron energy spectrum at a varying graphite surface with mono-directional, squared disc, 3 MeV, and 2 $\mu Amps$ proton source

proton beam), the neutron flux is at it's highest (inside the beam). Then the contour shows that flux starts to decay as neutron lake out to the surrounding (vertically), and leak toward the edges of the detector (horizontally). This is because detector starts to lose tracks when neutrons travel out of he detector into the outer air atmosphere, where neutrons experience interactions, or get lost.

3.1.1.4 Phase 1 conclusion

So many graphite shields were tested, yet, no optimum value was achieved. It was necessary to test more shields in order to obtain the finest and most suitable design for the proton beam shielding. Detailed sensitivity of graphite thicknesses was applied, 6 more radii were tested, these are, 30 cm, 35 cm, 40 cm, 45 cm, 50 cm, and 55 cm as shown in Figure 3.14. Starting at thickness of 45 cm and higher, results show the minimum neutron energies. However, large load of graphite can be quite expensive, hence, it is important to optimize the best shielding design with the minimal cost. From the figure below, it can be said that the optimal shield design for the accelerator shielding

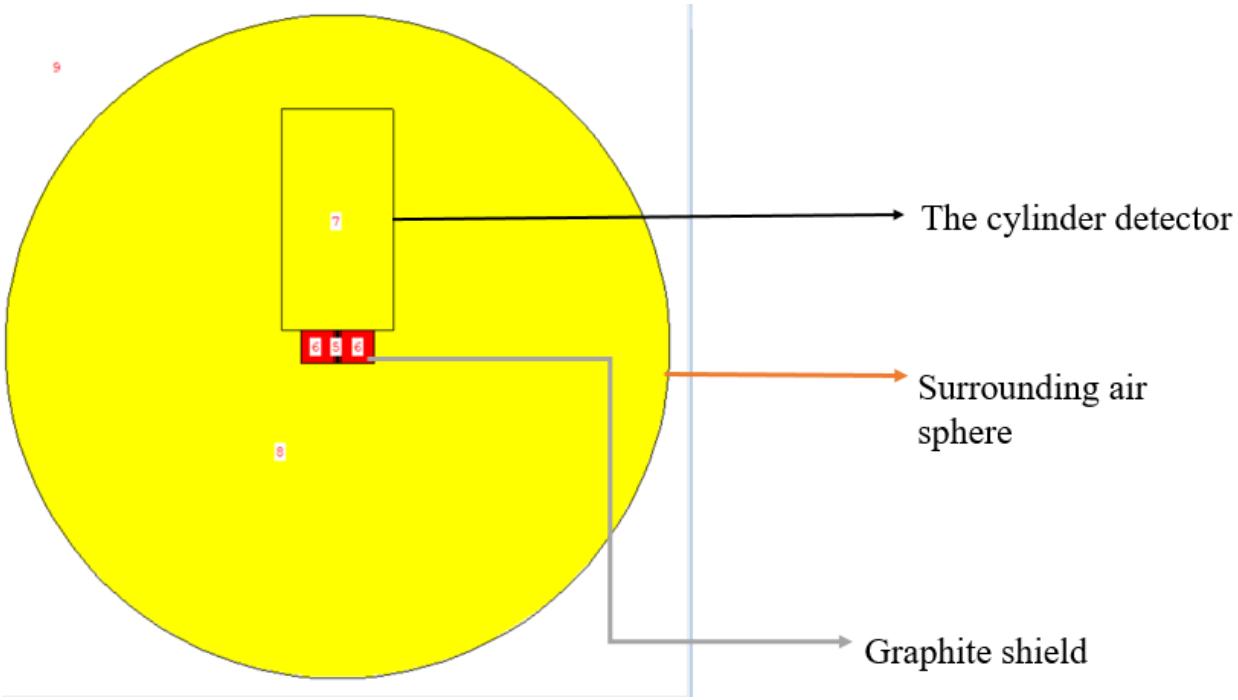

Figure 3.12: 2D MCNP6 model for the proton source with graphite shielding

with the minimal cost is at 45 cm.

3.1.2 Phase 2

To study how the produced neutron energy spectrum changes as a function of the proton source energy and strength, it was necessary to run several cases with different currents and different energies, as shown in Table 3.5, so we can reach the most desirable source parameter to induce the maximum fission events.

Table 3.5: Phase 2 cases

	Case 1	Case 2	Case 3	Case 4
Eneregy (MeV)	3	3	4.5	4.5
Strength (μ $Amps$)	2	10	2	10

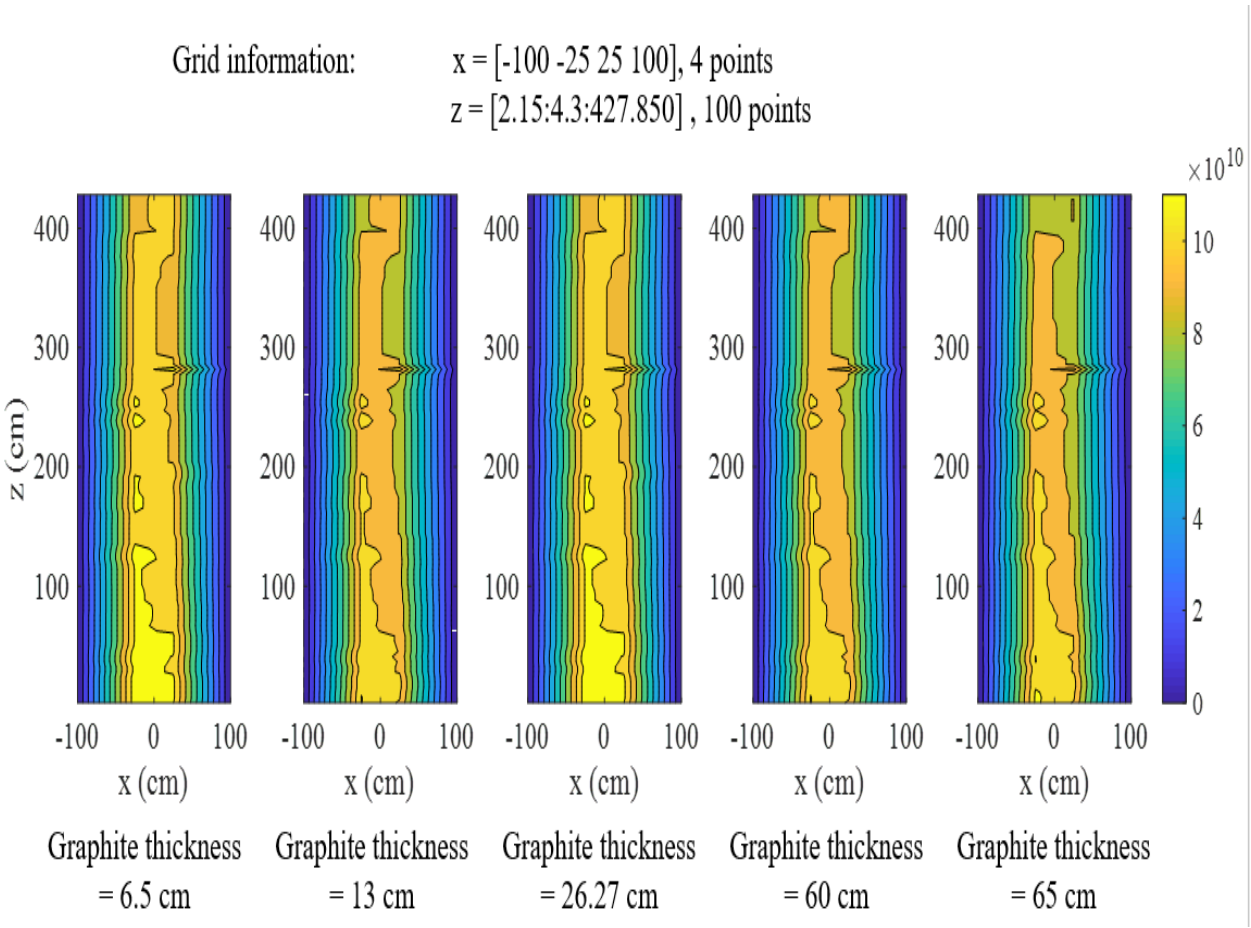

Figure 3.13: Contour plot for neutron flux as a function for five tested graphite shields

3.1.2.1 Phase 2 Results

The source strength increment shows a linear proportional behavior for the generated neutron flux, however, increasing the source energy shifts the generated neutron spectrum to higher energies, which is more beneficial for the ^{232}Th fast fission events, the maximum energy and current the proton beam can operate at is 4.5 MeV and 2 $\mu Amps$, hence, these parameters will be used in the simulations.

As shown in Figure 3.15, the source strength increment shows a linear proportional behavior with the neutron flux generated but does not affect the energy spectrum. However, increasing the source energy shifts the generated neutron spectrum to a higher energies, the neutron energy peak when 3 MeV source energy was used is at 0.5 MeV and the max is at 1.3 MeV, while using the

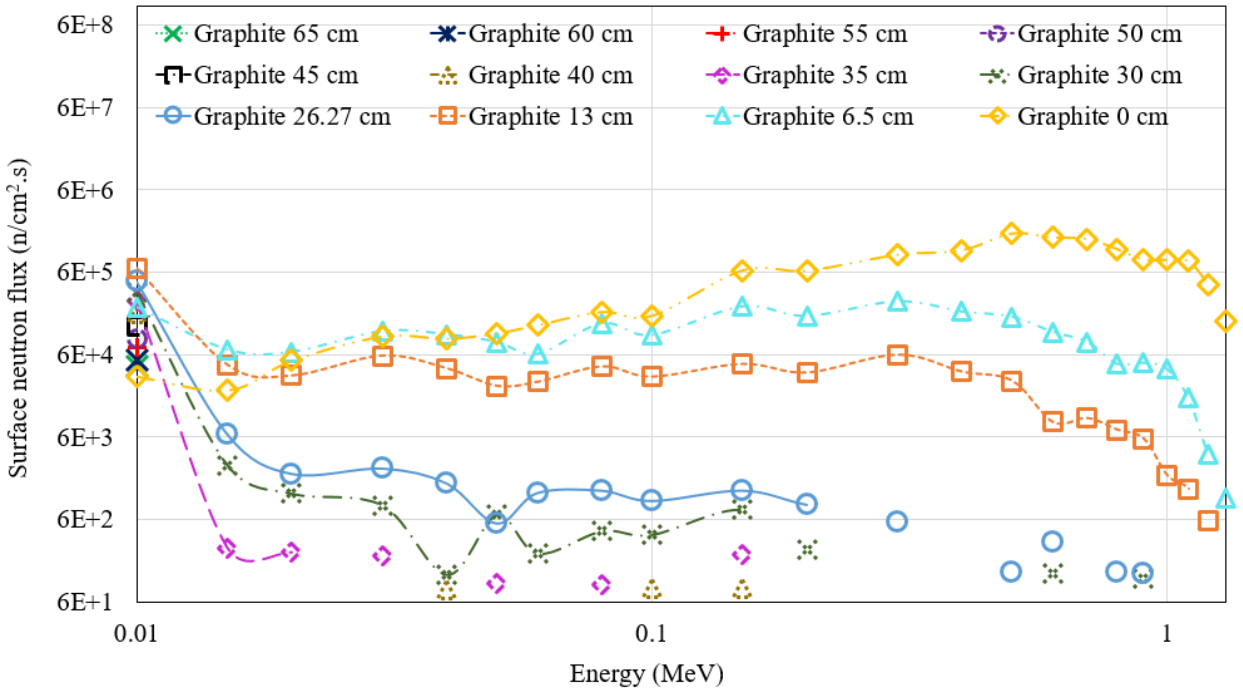

Figure 3.14: Neutron energy spectrum at a varying graphite surface with mono-directional, squared disc, 3 MeV, and 2 $\mu Amps$ proton source

4.5 MeV source energy, the peak is at 1.3 MeV and the max is at 2.9 MeV. Knowing that the ^{232}Th fast fission threshold is at 1 MeV, fast fission events will be minimal if the 3 MeV source energy is to be used. Although there are some neutrons with energy of 1.3 MeV, the reaction cross section at this less than 0.1 barn. When using a higher energy source, the energy peak is shifted to a peak at 1.3 MeV and a max of 2.9 MeV.

Figure 3.16 shows the vertical neutron flux at the center line of the proton beam, as strength increase by a factor of 5, the integrated generated neutron flux increases by the same factor. It is shown that the maximum flux is at Z = 0, which is the location of the ^{7}Li target inside the beam, in other words, where the spallation reactions ^{7}Li(p,n)take a place.

From here, and in order to maximize the possibility of fission events with molten slat, the energy 4.5 MeV with 2 $\mu Amps$ will be the parameters used for the proton source definition.

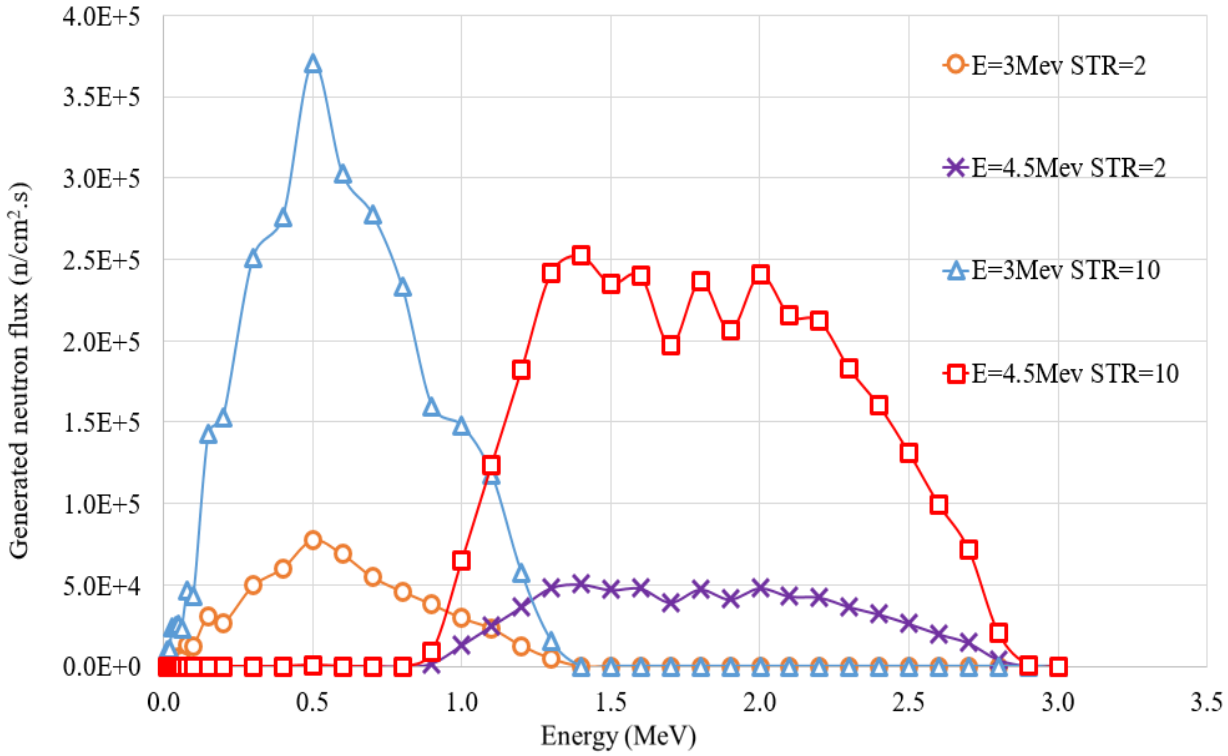

Figure 3.15: Generated neutron spectrum for different proton source configurations.

3.1.3 Phase 3

FLiNaK-ThF_4 test section was added to the simulations in this phase, the molten salt is confined in a stainless steel 316 piping, with outer diameter (OD) of 6.6802 cm, inner diameter (ID) of 5.3288 cm, and 50 cm length. The stainless steel piping thickness is 0.6757 cm and is composed of 10 elements with weight fraction as shown in Table 3.6[29]. The FLiNaK molten salt has a mole fraction of: LiF = 46.5%, NaF = 11.5%, KF = 43%. A MATLAB code was built to convert mole fraction to a weight fraction, the weight fraction for each element was calculated to be as follow: Li = 8%, Na = 6%, K = 40%, F = 46%. All the compounds of thorium are quadrivalent; accordingly, the use of thorium in molten fluoride must be in the form of ThF_4.

ThF_4 was added to the FLiNaK, the mole fraction of the fuel salt is: LiF = 40.5%, NaF = 9.5%, KF = 38%, ThF_4 = 12%. Weight fraction for each element is: Li = 3.75%, Na = 3%, K = 20.15%, Th = 38%, F = 35.1%. Lithium target initial depth was taken to be 0.02 cm, located at the center

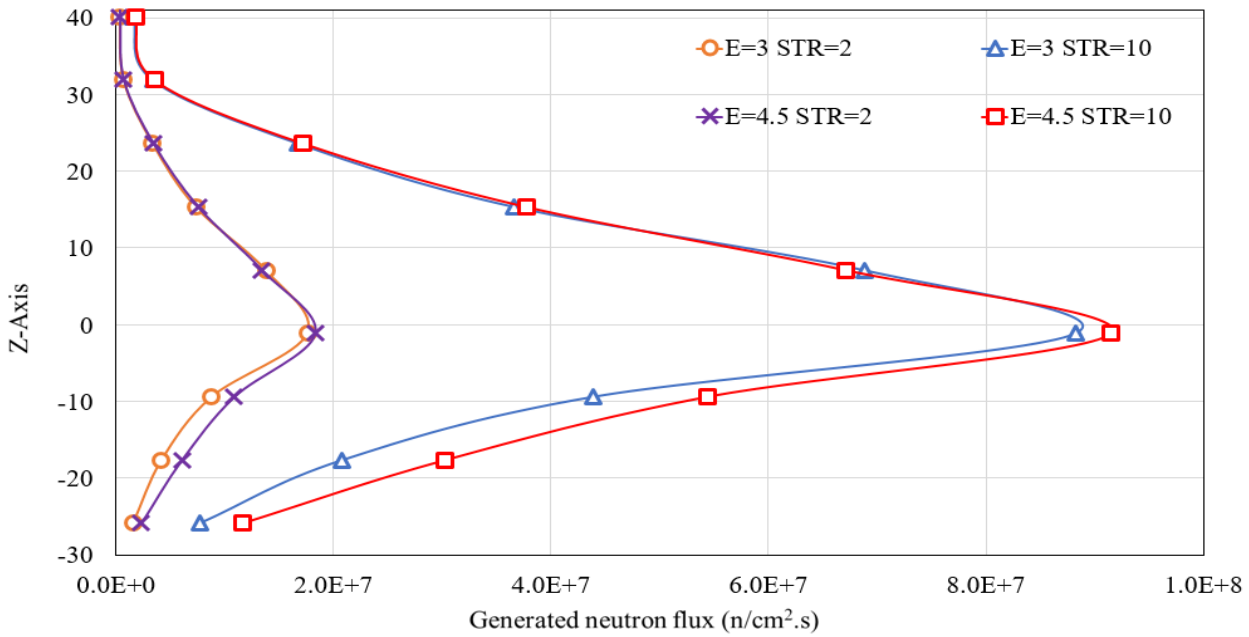

Figure 3.16: Axial neutron flux at the proton beam center using FMESH tally

Table 3.6: Stainless steel 316

Element	Weight percent (%)
Chromium	18
Nickel	14
Molybdenum	3
Carbon	0.08
Manganese	2
Phosphorous	0.045
Sulfur	0.03
Silicon	0.75
Nitrogen	0.1
Iron	61.995

of the proton beam (Z = 0 cm in simulations). Shown in Figure 3.17 is a 2D MCNP model for the FLiNaK-ThF_4 pipe section.

Figure 3.18 shows a 3D MCNP model .The lithium target in this phase is placed at the center of the proton beam, graphite shielding has a radius of 45 cm.

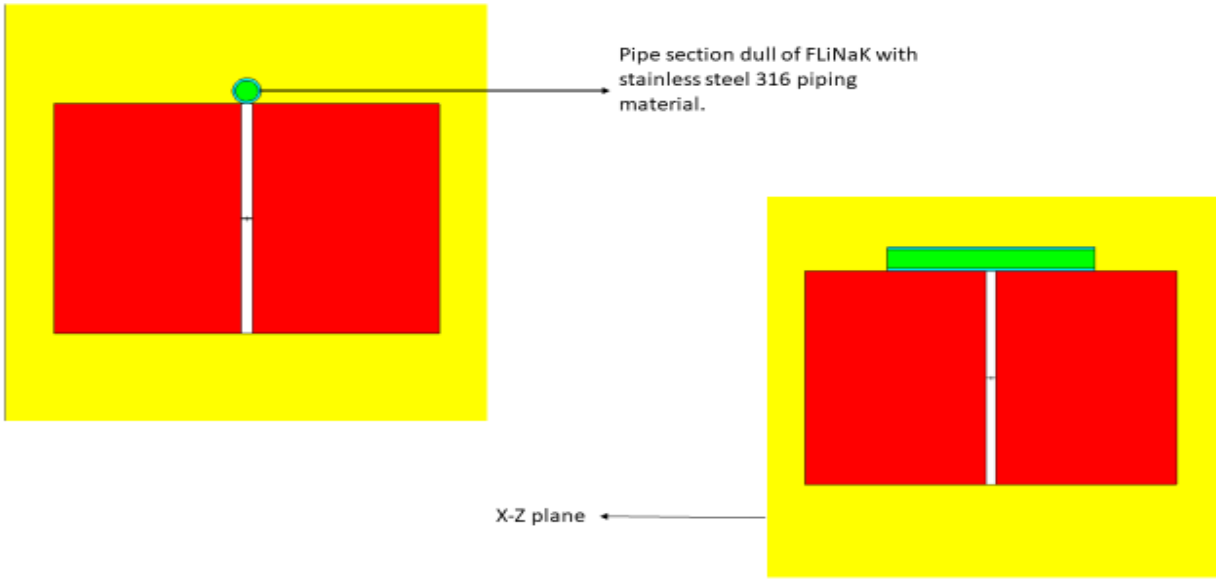

Figure 3.17: 2D MCNP model FLiNaK-ThF_4 test section

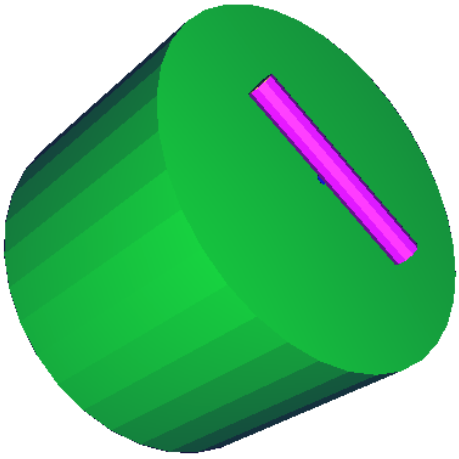

Figure 3.18: 3D MCNP model FLiNaK-ThF_4 test section

3.1.3.1 Phase 3 Results

Figure 3.19 shows the ^{232}Th paths after neutron absorption. Neutrons can also be produced not only by fast fission, but also via the photo-fission and photo-neutron reactions of ^{232}Th as mentioned in chapter 2. FMESH tally was used to calculate the vertical neutron flux at the center line of the proton beam to visualize the flux behaviour.

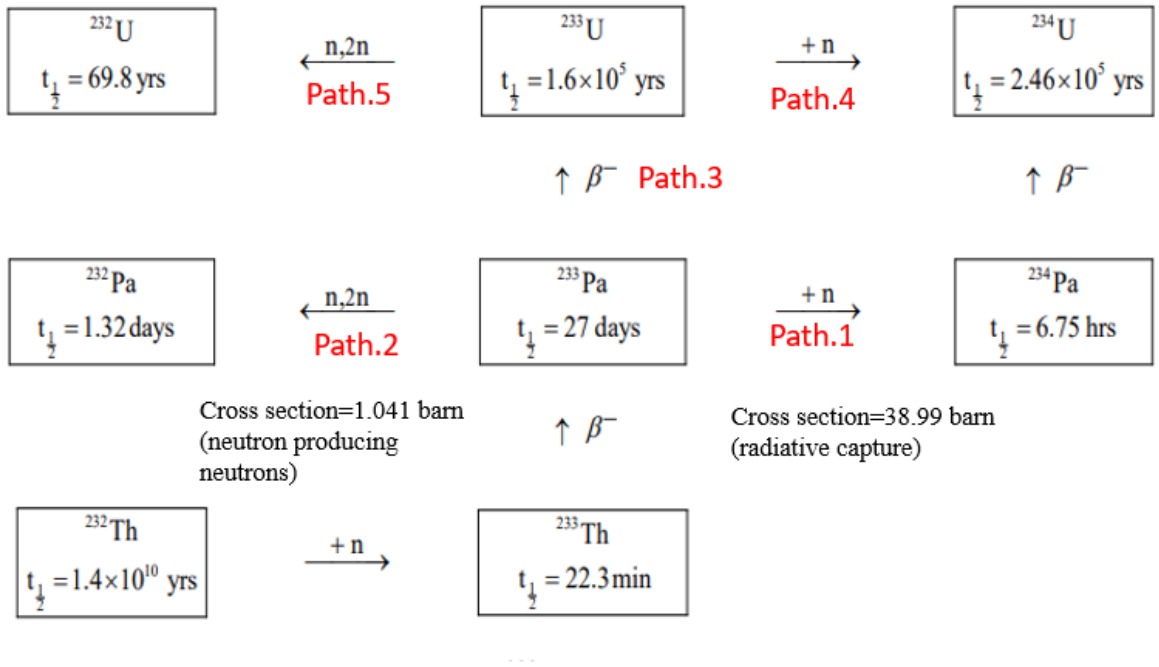

Figure 3.19: ^{232}Th paths after neutron absorption
[1]

Figure 3.20 shows the vertical neutron flux for the model (proton beam and FLiNaK-ThF_4), the maximum flux is at the location of the lithium target. However, when proton particles are subjected to the target, neutrons are produced isotropically, but with a little angular preference with respect to the protons particles ejection direction. So far, minimal fission events were recorded inside test section, as a result, a negligible induced fission neutrons .

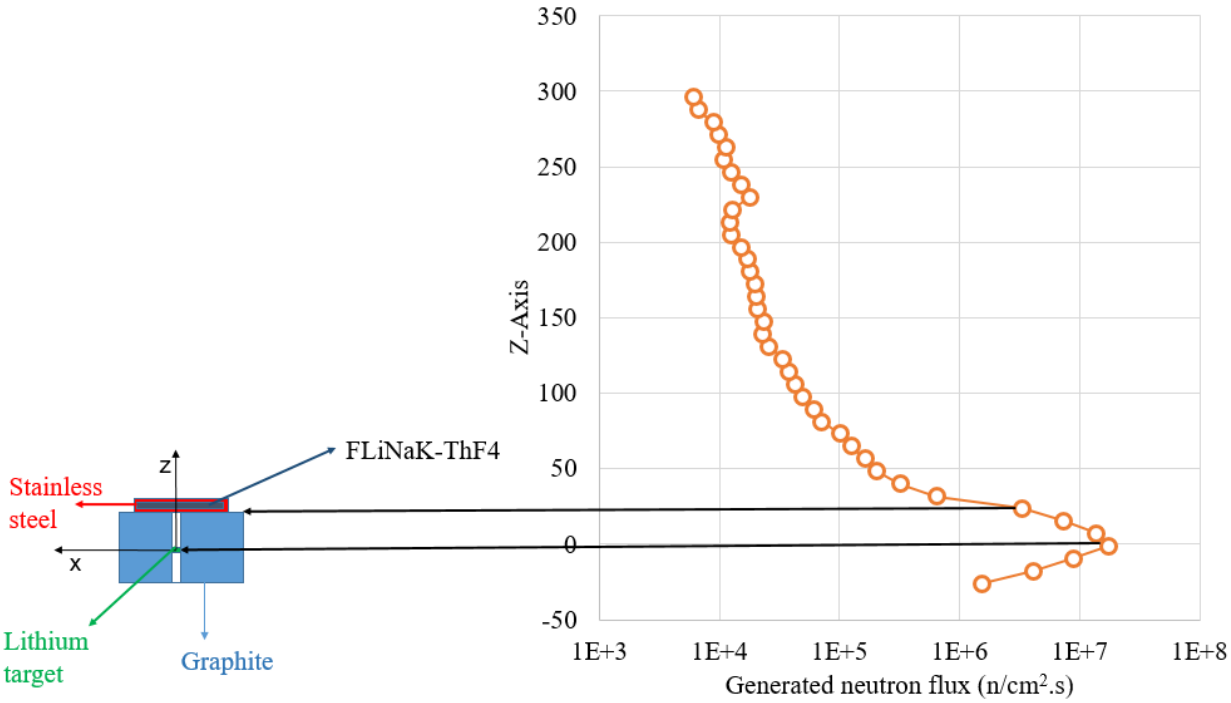

Figure 3.20: Axial neutron flux at the proton beam center with FLiNaK-ThF_4

^{232}Th fast fission cross section threshold is at 1 MeV, two proton source energies were tested, 3 MeV and 4 MeV, generate a max of 1.3 MeV and 2.9 MeV neutron energy, respectively. Although ^{232}Th fast fission has 1 MeV threshold, the cross section is less than 0.1 $barn$ and about 0.13 $barn$ at 1.3 MeV and 2.9 MeV, respectively.

3.1.4 Phase 4

Fm tally multiplier card was applied to calculate and visualize the ^{232}Th radiative capture, and the ^{232}Th fission reaction rate density ($interactions/cm^3.s$) inside the FLiNaK-ThF_4 test section. Higher neutron particle history was run in order to reach symmetry for the reaction rate density in test section. Since ^{7}Li is also one of the molten salt components, it might be unnecessary to place a lithium target inside the proton beam. Thus, this phase also investigate the effect of the lithium target existence on the generated neutron flux inside the test section. Table 3.7 shown the 4 cases that were examined in this phase.

Table 3.7: Phase 4 cases

	Case 1	Case 2	Case 3	Case 4
Eneregy (MeV)	3	3	4.5	4.5
Strength ($\mu Amps$)	2	2	2	2
Lithium target	Exist	Do not exist	Exist	Do not exist

3.1.4.1 Phase 4 Results

When the source energy was set to 3 MeV, eliminating the lithium target did not result in any fission events. This is because the particles can not penetrate the stainless steel piping. Placing the target at the center of the beam, with the same source energy (3 MeV) generated an infinitesimal fission events as shown in Figure 3.21. When the energy is increased to 4.5 MeV, proton particles will have enough energy to penetrate the stainless steel piping, but still no sufficient fission events were detected. However, the lithium target existence is beneficial, because the total neutron flux generated was larger when the target was placed, regardless the source energy.

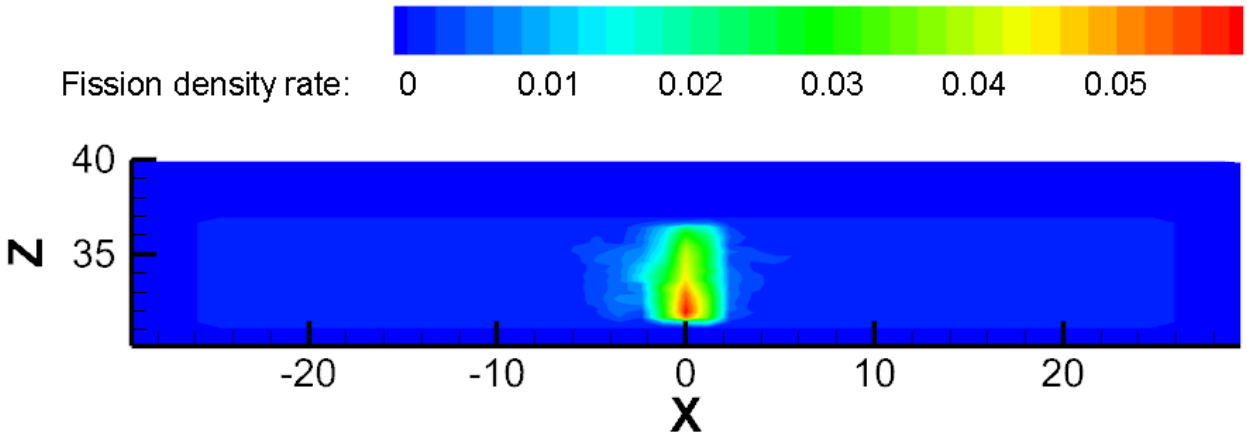

Figure 3.21: ^{232}Th fission rate density in units of ($reactions/cm^3.s$) for case 1

It was noticed that the radiative reaction rate density among the FLiNaK-ThF_4 test section is asymmetric as shown in Figure 3.22. So far, simulations that were run up to this stage were set at

10^7 neutron particle history, to pass the MCNP6 10 statistical checks and assure symmetry among the test section, a 10^9 neutron particle history was run, and the capture rate density reached a symmetrical contour among the test section as shown in Figure 3.23.

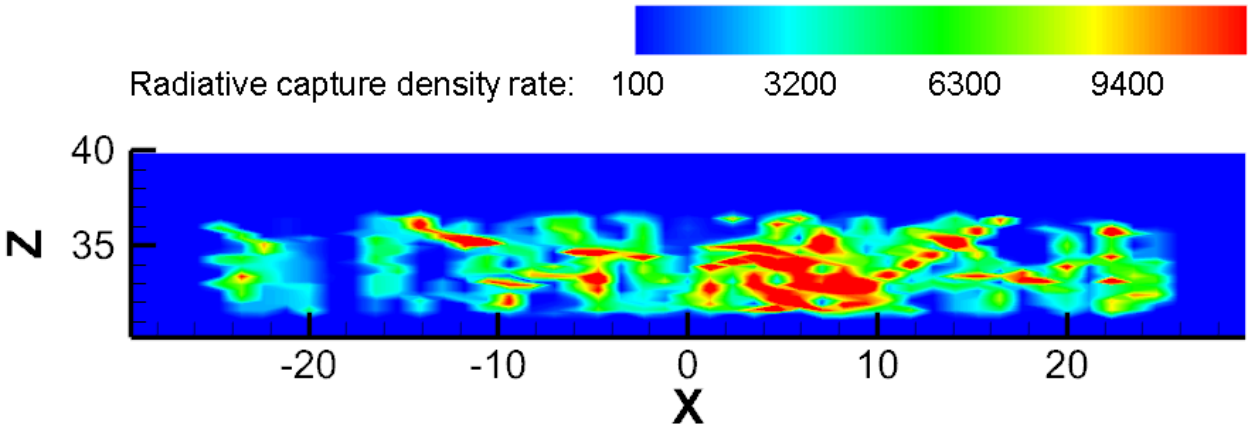

Figure 3.22: ^{232}Th radiative capture rate density with 10^7 nps for case 1

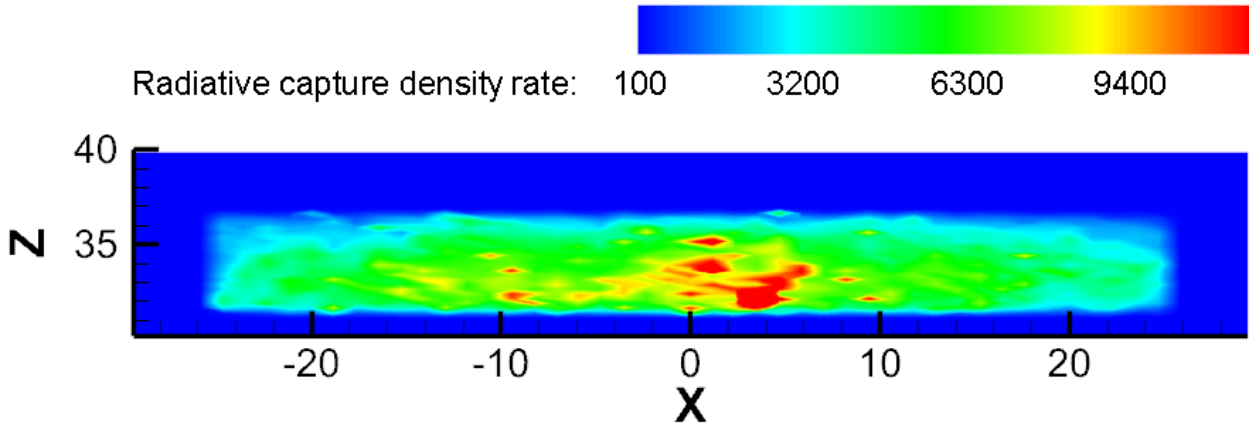

Figure 3.23: ^{232}Th radiative capture rate density rate with 10^9 nps for case 1

3.1.5 Phase 5

The focus of this phase is to replace the proton source with an equivalent neutron source to study the effect of the source particle type on the ^{232}Th fission events, and induced fission neutrons production. Different types of neutron source were simulated, isotropic, mono-energetic, and mono-directional neutron source replaced the proton source as shown in Table 3.8.

Table 3.8: Phase 5 cases

	Case 1	Case 2	Case 3
Strength ($neutrons/s$)	3.8585E+09	3.8585E+09	3.8585E+09
Angular specification	Isotropic	Isotropic	Mono-directional
Energy (MeV)	weighted energy	Mono-energetic	Weighted energy

The source configurations shown above were selected to investigate the angular and energy of the neutron source impact. The isotropic, weighted energy neutron source definition was extracted from a bare case geometry, where a proton source (4.5 MeV, 2 $\mu Amps$) was subjected to a lithium target and produce neutrons via spallation. The total neutrons generated was set as the source strength, with the normalized probability for each energy bins, in units of ($neutrons/s$). The same definition but mono-directional source was applied in one case, and mono-energetic, isotropic was applied in the other case. The mono-energetic neutron source eject all neutrons having the same energy (which is the maximum produced neutron energy), it is more likely to detect induced fission neutrons than the first case, because all neutrons carry energy above the fission threshold. However, The case where the neutron source is mono-directional, the neutrons leakage probability out of the proton beam is very low, in such a case, almost all neutrons reach out to the test section, thus, it is even more probable to induce fast fission events.

3.1.5.1 Phase 5 Results

The first case resulted in a negligible fission events as shown in Figure 3.24, and a radiative capture events is shown in Figure 3.25.

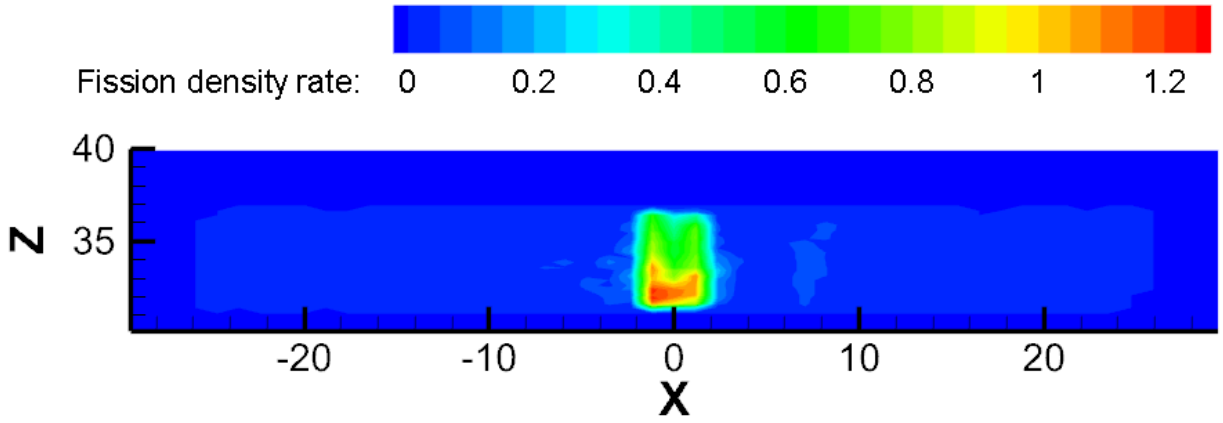

Figure 3.24: ^{232}Th fission rate density for isotropic, energy weighted neutron source.

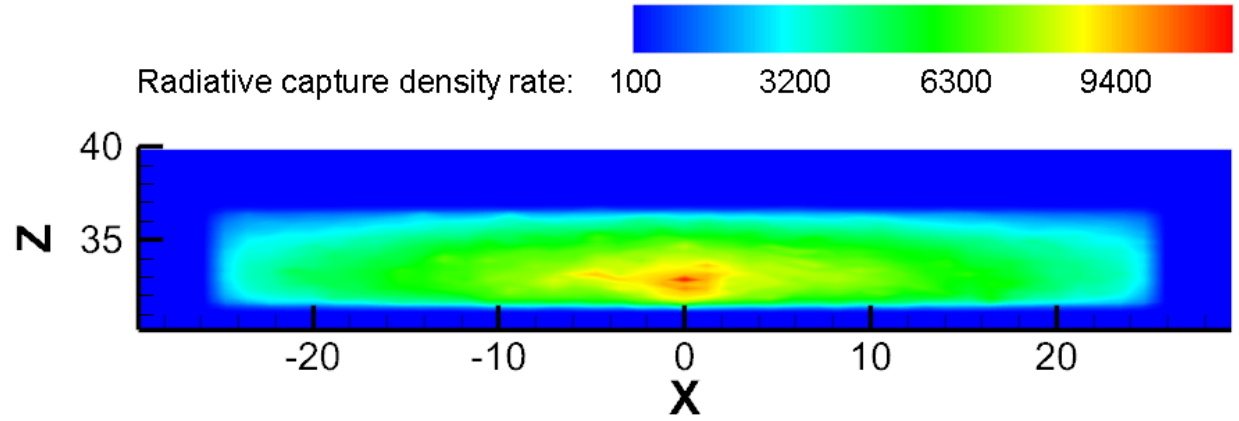

Figure 3.25: ^{232}Th radiative capture rate density for isotropic, energy weighted neutron source

Recalling the fission energy threshold of ^{232}Th at 1 MeV, fission events are almost rare with this source configuration. Replacing with mono-energetic source (with energy that equals to the peak energy which is 1.3 MeV) increase the reaction rate density for both capture and fission.

This is because when all the neutrons carry an energy of 1.3 MeV, which is larger than the threshold for the ^{232}Th fast fission threshold, as a result, fission events probability will rise, thus, fission rate density will increase slightly as shown in Figure 3.26, and in Figure 3.27.

The plots show the XZ-plane cross section for the reaction rate density inside the test section.

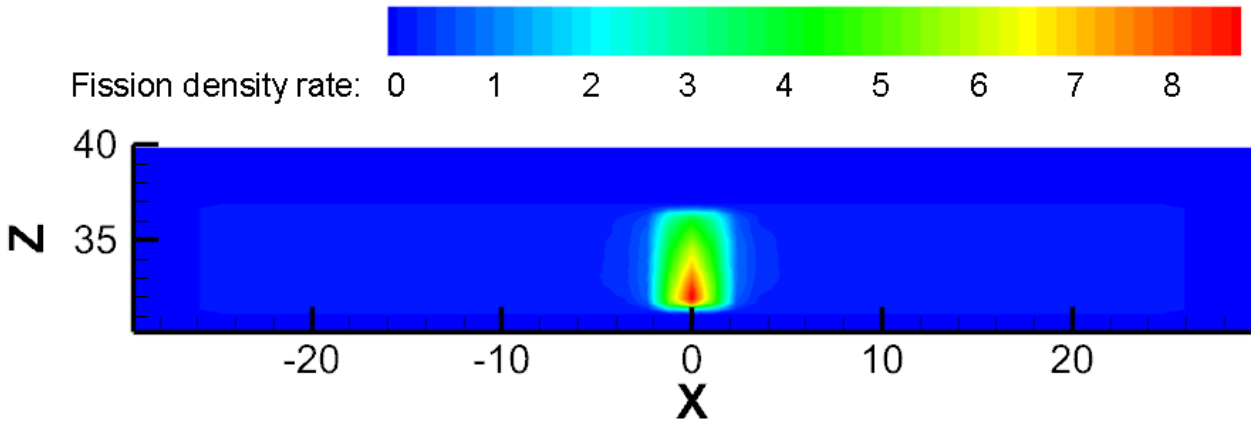

Figure 3.26: ^{232}Th fission rate density for isotropic, mono-energetic neutron source

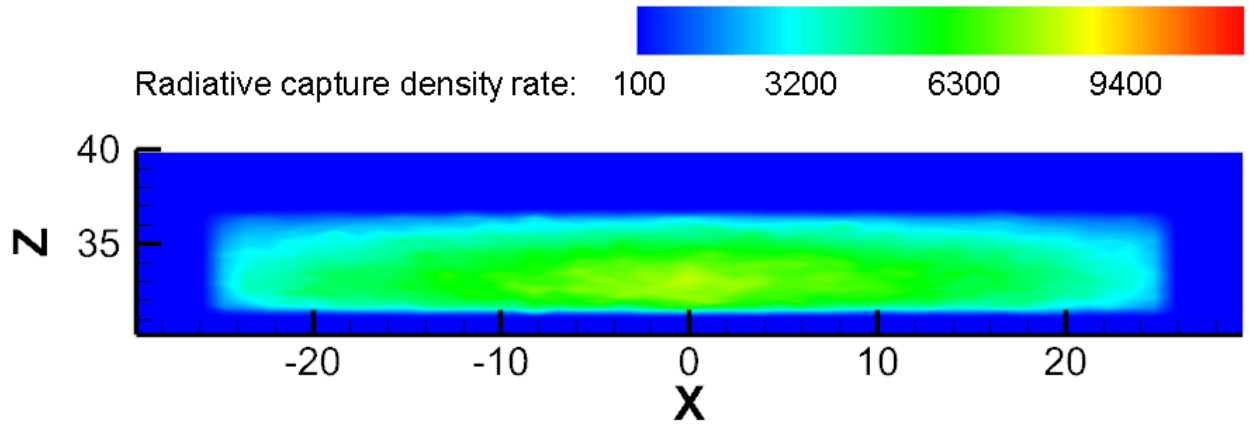

Figure 3.27: ^{232}Th radiative capture rate density for isotropic, mono-energetic neutron source

In the simulation, the FLiNaK-ThF_4 tube starts at X = -25 cm, and ends at X = 25 cm, and has an ID of 5.3288 cm, OD of 6.6802 cm. However, the fission rate density for the mono-energetic neutron source is not sufficient enough, forcing all the neutrons to travel in one direction, regardless the source energy, will minimize the neutron leakage and expected to result in even more fission events. Setting the source to mono-directional resulted in a larger fission rate density as expected, this is shown in Figure 3.28, and Figure 3.29, respectively.

So far, the definition where the neutron source is set to a mono-directional source resulted in the most fission and radiative capture events among the three configurations. However, the physical

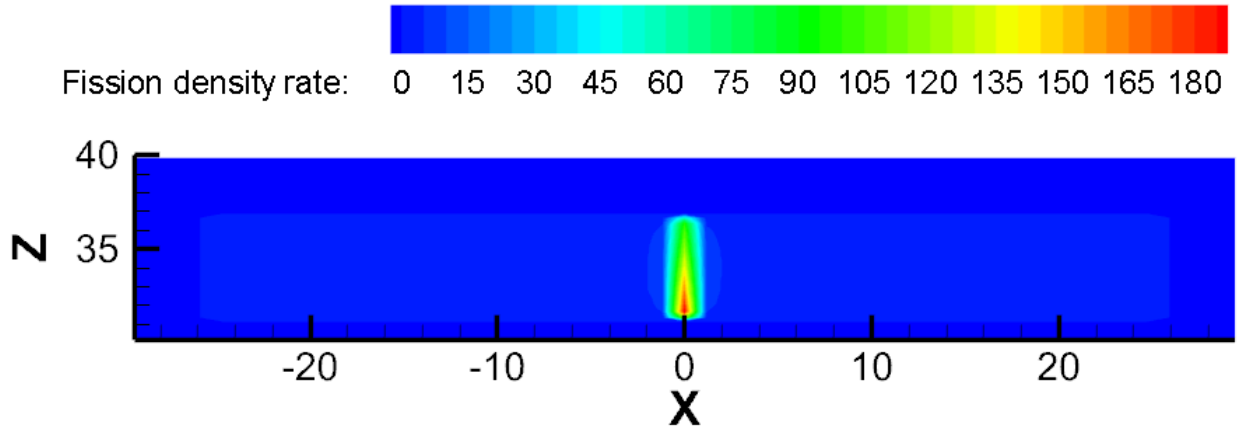

Figure 3.28: ^{232}Th fission rate density for mono-directional, energy weighted neutron source

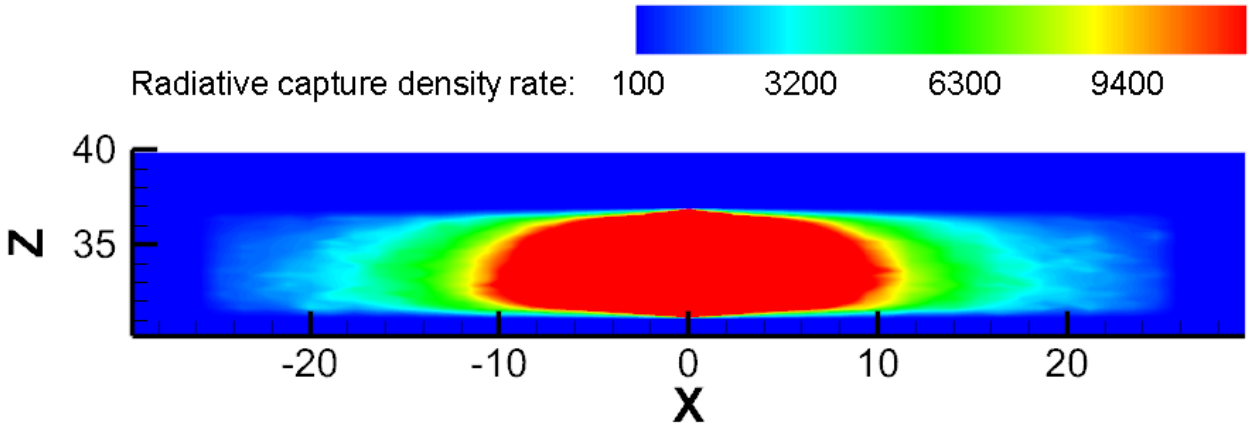

Figure 3.29: ^{232}Th radiative capture rate density for mono-directional, energy weighted neutron source

source particle in the molten salt loop facility is a proton beam and not a neutron source, hence, a proton particle type should be used when defining for the source in simulations. To detect some fission neutrons with a proton source, a very strong and high energetic proton beam simulation was run. This was done to know the strength and the energy threshold the proton source should operate at in order to induce fission events.

A 20 $\mu Amps$, 100 MeV proton source with 45 cm graphite shield, S316 stainless steel pipe was filled with FLiNaK-ThF_4 (12%), although these values are dramatically large compared to

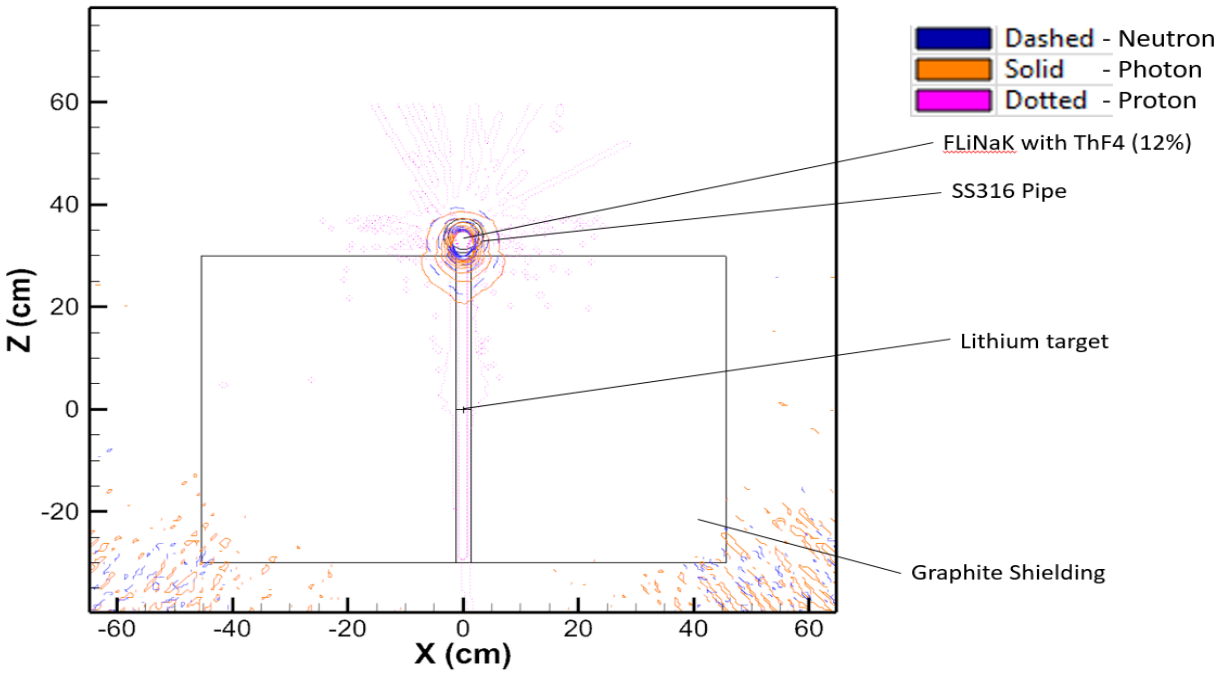

Figure 3.30: Contour plot of particles generated in 2D MCNP6 model

the accelerator operation capacity, this simulation was run to study the probability of detecting neutrons with proton source. Figure 3.30 shows a contour plot for neutrons, protons, and photons for this simulation, it is shown that the lithium target is located at the center of the proton beam, the proton particles (pink dots), travel in one direction until particles reach the target and start producing neutrons via spallation interactions.

Protons start scattering and interacting with the target, although neutrons are produced isotropically, there is some angular preference associated with proton particles ejection direction. The neutron spectrum generated inside the FLiNaK-ThF_4 is shown in Figure 3.31. And contour plot of the neutron flux for the above condition is shown in Figure 3.32. It is shown below that neutrons are reflected within the graphite shield, and start to leak once the flux reach the graphite edges. Two more simulations were run; one is to study the lithium target presence impact on the neutron flux generated in FLiNaK-ThF_4, where the target was removed, and another one where the test section was only filled with thorium with a mole fraction of (12 $\%$). Figure 3.33 shows all of the three simulations that were run twith 100 MeV, 20 $\mu Amps$ proton source.

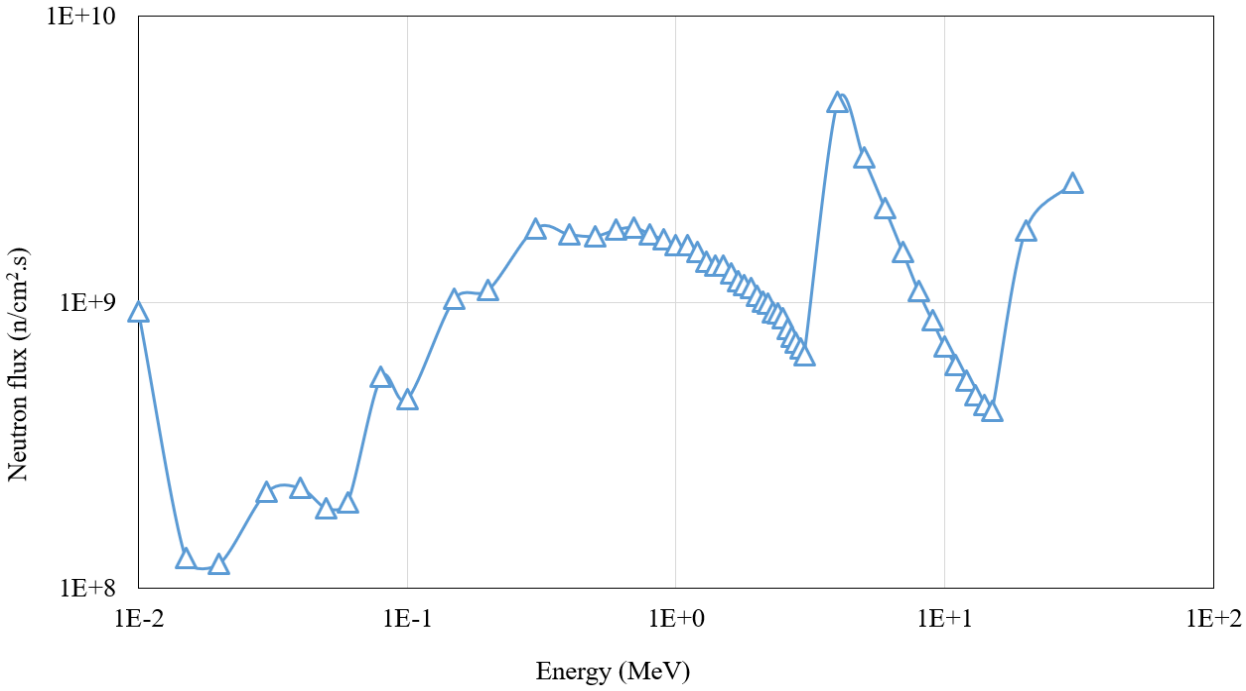

Figure 3.31: Neutron flux inside FLiNaK-ThF4 with 100 MeV, 20 $\mu Amps$ proton source

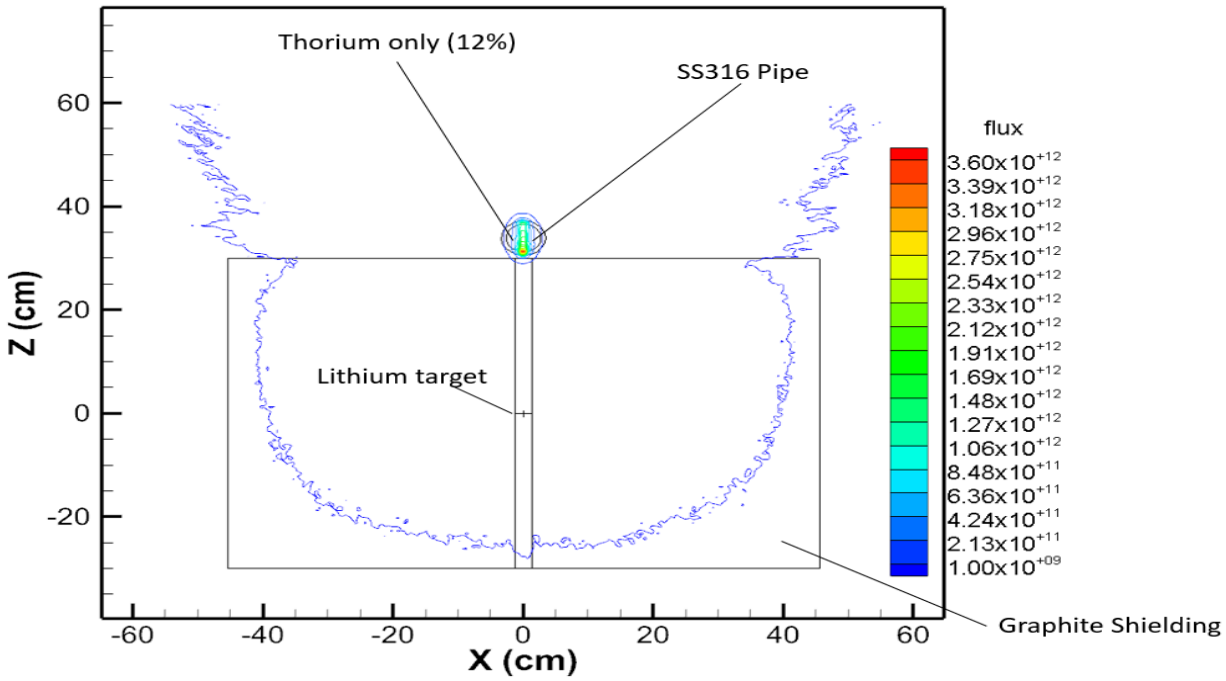

Figure 3.32: Contour plot of the neutron flux generated in 2D MCNP6 model

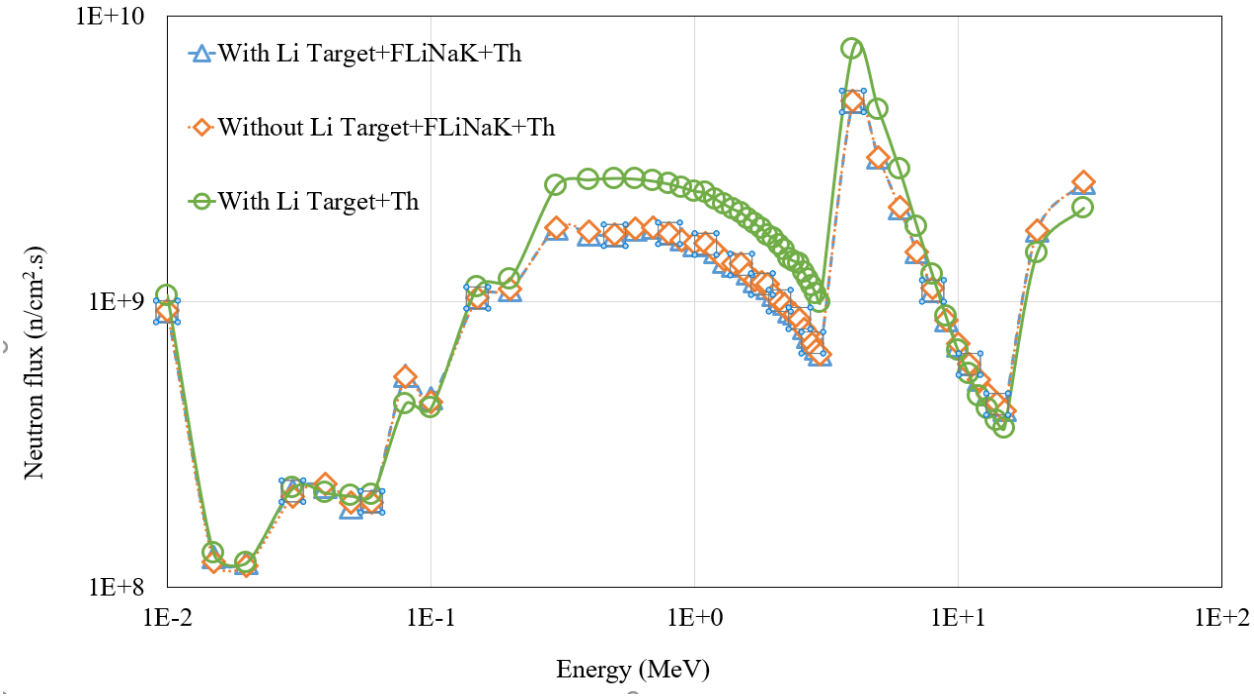

Figure 3.33: Neutron flux inside FLiNaK-ThF_4 with 100 MeV, 20 $\mu Amps$ proton source

3.1.6 Phase 6

So far, fission neutrons were only detected with a neutron or a very strong bigh enery proton beam. This phase apply the realistic source specifications, which is 4.5 MeV, 2 $\mu Amps$ proton source, and introduce new perturbations to try maximizing the ^{232}Th fast fission reaction rate density. Perturbations were done for target thickness, location, and the thorium concentration in the molten salt as shown in Table 3.9.

Table 3.9: Phase 6 cases

	Li target thickness (cm)	Li target location z = (cm)	^{232}Th mole fraction (%)
Case 1	0.02	0	12
Case 2	None	None	12
Case 3	0.02	28	12
Case 4	3	0	12
Case 5	0.02	0	38

For example, including and excluding the target from the proton beam and then comparing the results will give the required feedback on target utilizing factor. Applying a thicker target may affect the proton particles penetration through the target, and locating the target at a position that is closer to the test section is expected to minimize the neutron population leakage when produce, thus, all the generated neutron will be able to travel and reach the molten salt with a minimum leakage, interactions, or back scattering. Increasing the ^{232}Th mole fraction in the FLiNaK-ThF_4, may or may not, increase the fission events or the induced fission neutrons. This phase will determine the importance of each factor, and the most efficient one that leads to maximizing the production of fission neutrons.

3.1.6.1 Phase 6 Results

From the examinations that were run in this phase, Table 3.10 below shows the total neutrons gain due to nuclear interactions, total neutron gain due induced fission, and total neutron creation. From here, it can be concluded that it is now a trusted fact that placing a lithium target inside the proton beam is essential for induced fission neutrons production.

Table 3.10: Neutron production for phase 6

	Due to interaction per source particle	Due to fission per source particle	Total neutron creation per source particle
Standard settings	2.4960E+04	0.000000	4.5553E+09
No lithium target	1.1207E+07	0.000000	1.1207E+07
Closer lithium target	3.7440E+04	2.6643E+06	4.5552E+09
Thicker lithium target	0.000000	0.000000	1.0768E+10
Larger thorium mole fraction	2.4960E+04	0.000000	4.5553E+09

As shown a 3 cm target thickness is acting like a barrier for proton particles to penetrate through, so that particles are not able to pass through and reach out to the test section. Increasing the thorium mole fraction in the molten salt is also not beneficial for fission production, thus no fission events were detected.

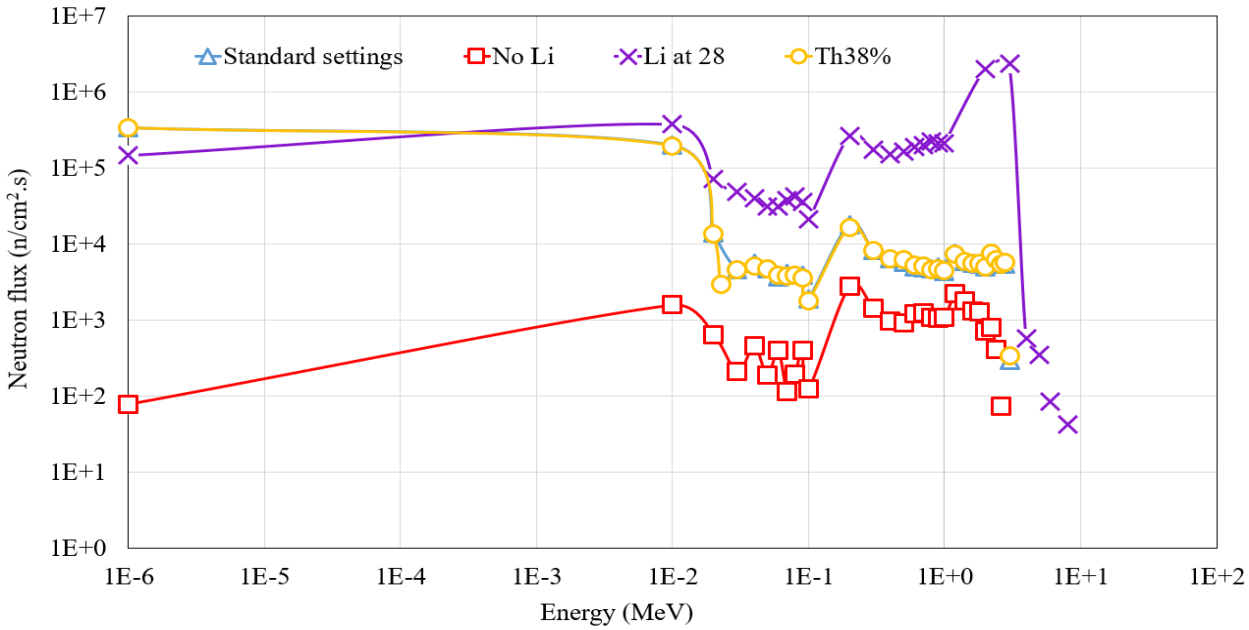

Figure 3.34: Neutron flux inside FLiNaK-ThF_4 with 4.5 MeV, 2 $\mu Amps$ proton source for different perturbations

The only case that reported fission neutrons is the one where the lithium target was placed at a location very close to the test section, which drastically decrease the neutron leakage. It can be said that when the target was placed at the center of the beam did not result in any induced fission neutrons, this is because neutrons leak, scattered, and moderated is high relatively, so that the neutron flux portion that reach to the test section is very small, and may carry energies under the ^{232}Th fast fission threshold.

Figure 3.34 shows the Neutron spectrum inside the FLiNaK-ThF_4 test section for the cases of phase 6, as shown, the highest neutron flux is the one with the closest target location in the beam.

Figure 3.35 shows the axial generated neutron flux at the beam center line, the maximum flux is at the center (Z = 0 cm) - where the target is placed - for the standard setting and Th 38$\%$ cases, where the maximum is shifted to Z = 28 cm when the target is moved to the same location, and the maximum is inside the test section when the target is removed, due to the neutron multiplication. It should be noted that increasing the thorium mole fraction in the salt does not affect the the generated neutron flux, where this case and the standard setting (12 %), fluxes are very similar.

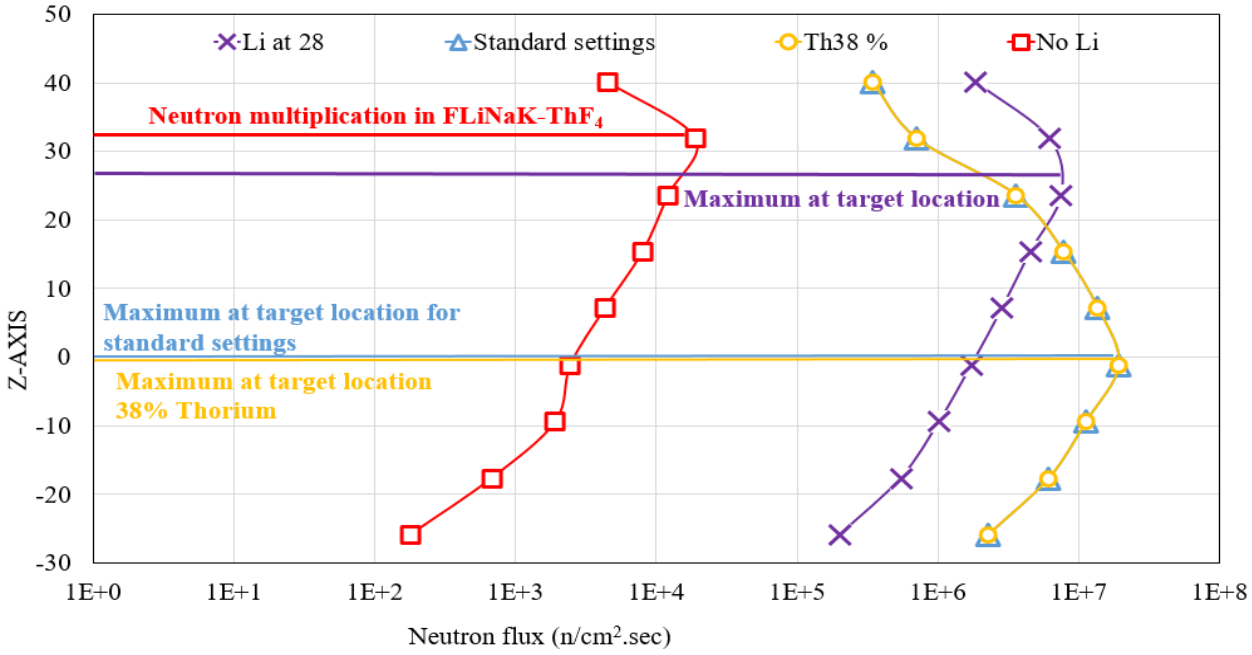

Figure 3.35: Axial neutron flux at the proton beam center with 4.5 MeV, 2 $\mu Amps$ proton source for different perturbations

3.1.7 Phase 7

The leakage of the produced neutron flux is a function of lithium target location inside the proton beam with the respect to the test section, and the target thickness. This phase perform a thickness and location perturbation to investigate the effect of each of these factors.

Four thicknesses were applied, each at two locations inside the proton beam as shown in Table 3.11. To obtain the effect of the target thickness, cases that share the same location are compared. Similarly, to see the location impact on the fission neutrons production, cases that share the same target thickness are compared. It is expected that the thicker the target, the less penetration probability for proton particles. On the other hand, it might be effective to use a thick target, in order to maximize neutron production via spallation, and place it at a close location to the test section. Hence, the generated neutron population can travel to the test section with a lower scattering and leakage probabilities.

Table 3.11: Phase 7 cases

	Lithium target thickness (cm)	Lithium target location (cm)	Source specification
Case 1	0.02	Z = 0	Proton source Eneregy = 4.5 MeV Strength = 2 μA
Case 2	0.02	Z = 28	Proton source Eneregy = 4.5 MeV Strength = 2 μA
Case 3	1	Z = 0	Proton source Eneregy = 4.5 MeV Strength = 2 μA
Case 4	1	Z = 28	Proton source Eneregy = 4.5 MeV Strength = 2 μA
Case 5	2	Z = 0	Proton source Eneregy = 4.5 MeV Strength = 2 μA
Case 6	2	Z = 28	Proton source Eneregy = 4.5 MeV Strength = 2 μA
Case 7	3	Z = 0	Proton source Eneregy = 4.5 MeV Strength = 2 μA
Case 8	3	Z = 28	Proton source Eneregy = 4.5 MeV Strength = 2 μA

3.1.7.1 Phase 7 Results

The same proton source definition -4.5 MeV, 2 $\mu Amps$- was used for the simulations in this phase. Figure 3.36, and Figure 3.37 shows the neutron spectrum inside the test section at different locations for the minimum, and the maximum thickness tested, 0.02 cm, and 3 cm,respectively.

It can be noticed that at thickness of 0.02 cm, the maximum neutron energy inside the test section is 8 MeV, while the maximum neutron energy at 3 cm is 7 MeV, both the target is located at Z = 28 cm. From these results and the results provided in phase 6, it can be concluded that the target needs to be placed at a position close enough to reduce neutron leak. Shown in Table 3.12 the induced fission neutrons production for each case.

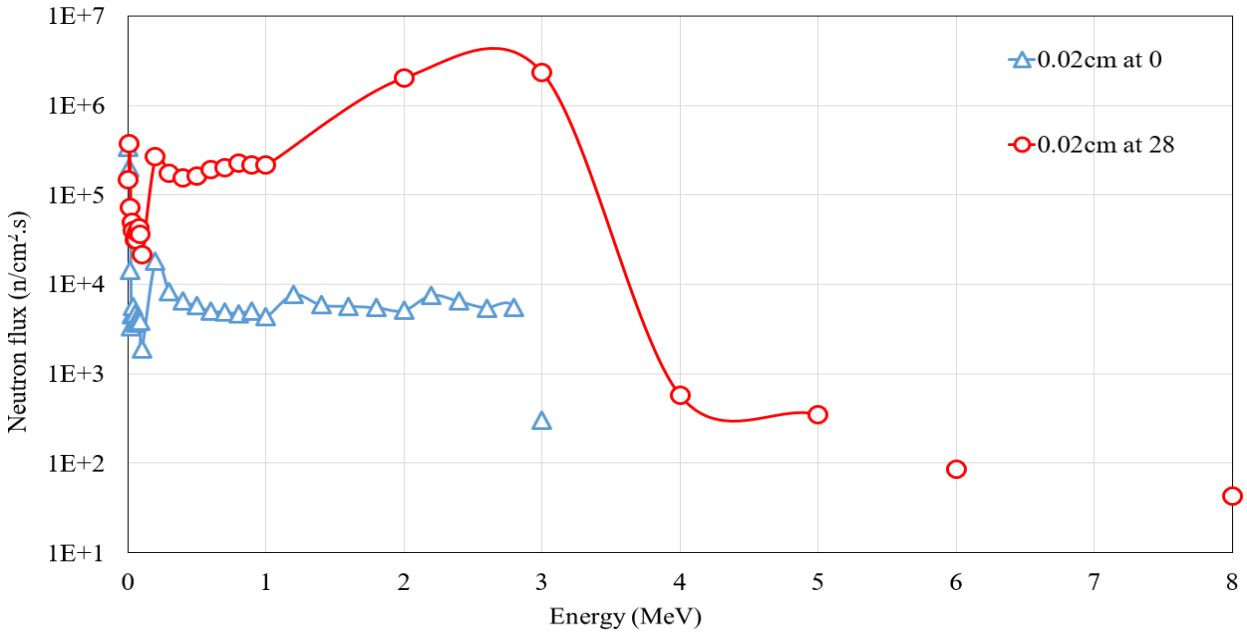

Figure 3.36: Target location effect with 0.02 cm on the neutron flux inside FLiNaK-ThF_4

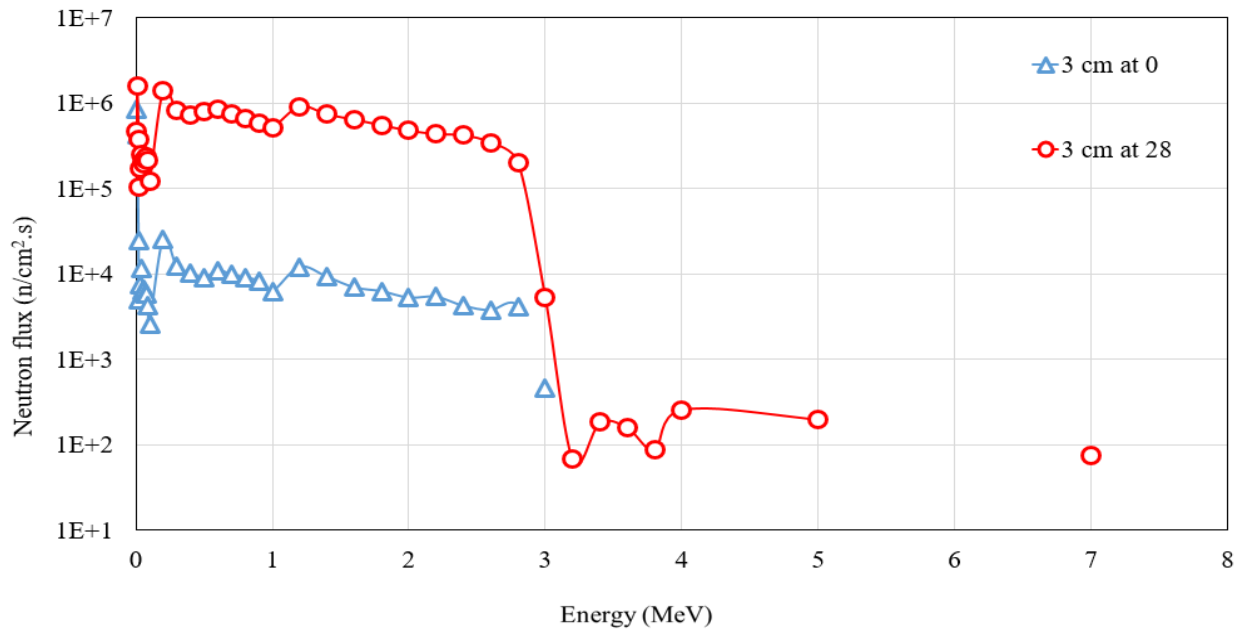

Figure 3.37: Target location effect with 3 cm on the neutron flux inside FLiNaK-ThF_4

Table 3.12: Induced fission neutron production for phase 7

Cases	Target thickness (cm) Target location (cm)	Fission neutrons produced created (per source particle)
Case 1	Thickness = 0.02 cm location = 0 cm	0.000000
Case 2	Thickness = 1 cm location = 0 cm	0.000000
Case 3	Thickness = 2 cm location = 0 cm	0.000000
Case 4	Thickness = 3 cm location = 0 cm	0.000000
Case 5	Thickness = 0.02 cm location = 28 cm	2.6643E+06
Case 6	Thickness = 1 cm location = 28 cm	2.5094E+06
Case 7	Thickness = 2 cm location = 28 cm	1.9428E+06
Case 8	Thickness = 3 cm location = 28 cm	1.7840E+06

Figure 3.38 and Figure 3.39 shows the sensitivity at the center of the beam abou 30 cm away (Z = 0), and at a closer location about 2 cm away (Z = 28), respectively. Clearly, when that target is placed far away, not only neutrons leak, but also the maximum neutron energy inside the test section is 3 MeV, at this energy, the ^{232}Th fission cross section is about 100 mb.

On the other hand, just by minimizing the distance between the target and the molten salt, it will not only cut down the leakage probability, higher energetic neutrons will reach out to the salt, and the flux will carry a maximum energy at 8 MeV, which is above the fast fission threshold and have a fast fission cross section peak of 450 mb.

So far, and based on the results of the previous examinations, it can be said that the target must be placed in the proton beam at a position that is close enough to diminish the leakage, and that as target thickness increase, not only the induced fission neutrons production decrease, but also the total neutron flux in the test is less.

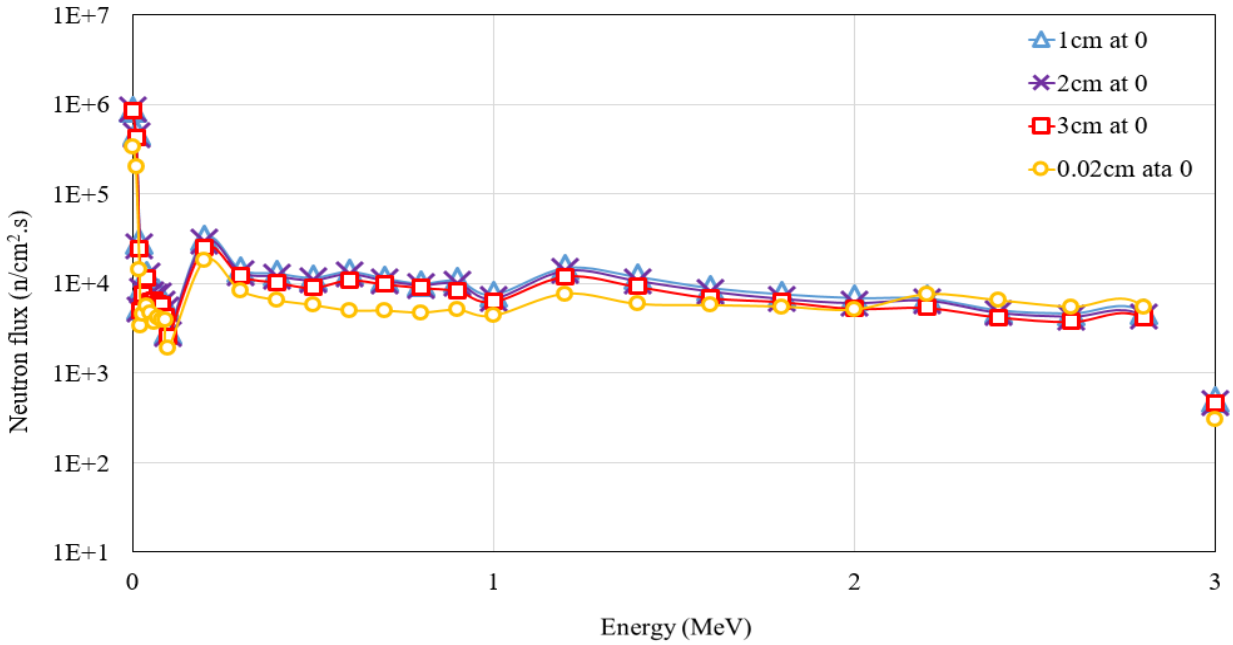

Figure 3.38: Thickness sensitivity at the beam center (Z = 0 cm)

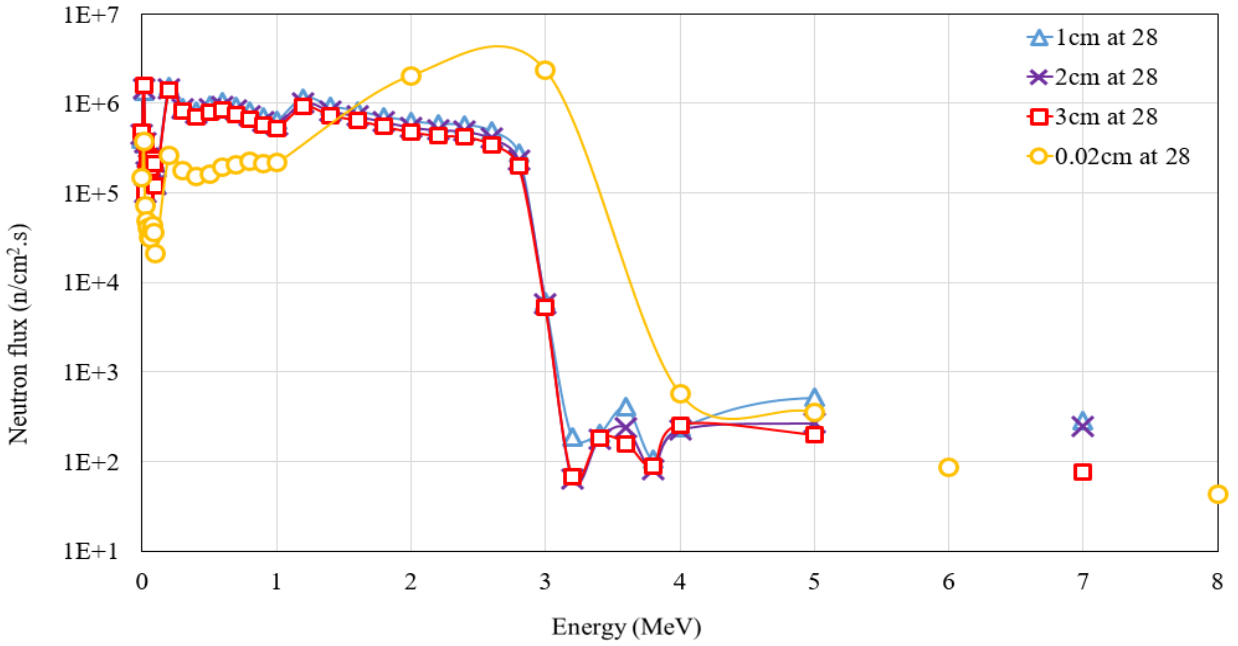

Figure 3.39: Thickness sensitivity at the end of the beam (Z = 28 cm)

3.1.8 Phase 8

Since the target depth is controversial factor, this phase aims to perform a detailed sensitivity analysis on the lithium thickness that most fulfill the operation of the molten salt loop facility. To achieve the optimum value, it was essential to perform a very small thickness increment, which was chosen to be 0.01 cm at a location nearby the test section (Z = 28 cm in the simulation), about 2 cm away from the test section. After obtaining the peak depth of the target, location is also a factor that have to be consider, it is important to locate the lithium as close as it can be located to the test section to reduce the neutron leakage, cases for this phase are shown in Table 3.13. As shown, a target depth starting at 0.01 cm and up to 0.1 cm, with a 0.01 cm increment sensitivity was performed to obtain the optimal thickness.

Table 3.13: Phase 8 cases

Cases	Target thickness (cm)
Case 1	0.01
Case 2	0.02
Case 3	0.03
Case 4	0.04
Case 5	0.05
Case 6	0.06
Case 7	0.07
Case 8	0.08
Case 9	0.09
Case 10	0.1

In the range between 0.01 cm and 0.1 cm, it is expected that protons are capable of passing through the target and producing neutrons at all depths in this range, neutrons production via spallation have a linear proportional relationship with thickness up to a certain value, after a value, the target depth will begin to behave as an obstacle to the proton particles to pass through. Hence, neutron production will decrease, and less fission events will occur. The purpose of this phase is to try to figure out the target depth that ensure protons penetration and producing the most neutrons.

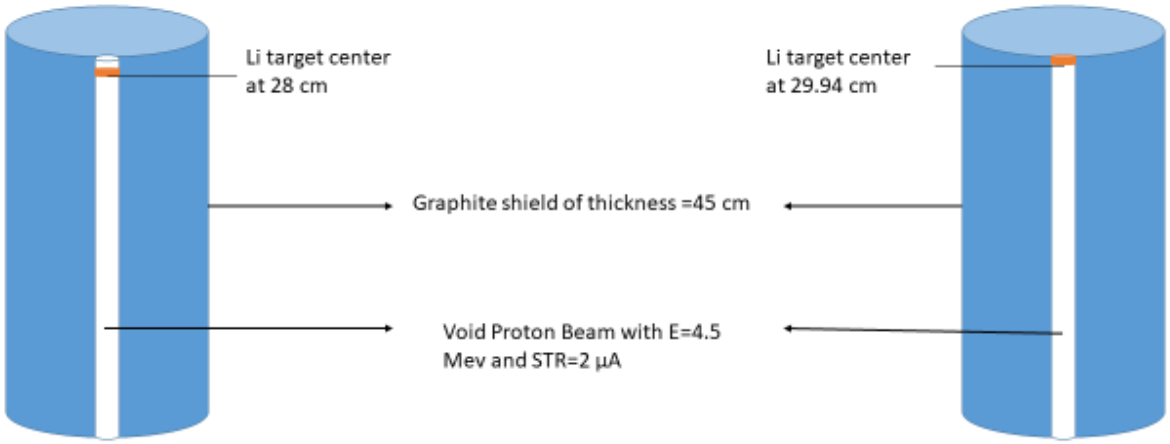

Figure 3.40: The two tested locations for the Li target

As mentioned above, neutron leakage is a phenomena that should be avoided as much as possible, so the closer the lithium to the test section, the less neutron leakage. Thus, the target was located at position that is attached to the FLiNaK-ThF_4 test section (Z = 28.94 cm in the simulations). This is shown in Figure 3.40, almost all of the neutrons produced will travel and make it to the test section with the minimal leak, interactions, or scattering.

3.1.8.1 Phase 8 Results

Table 3.14 shows the number of fission neutrons produced, fission neutrons tracks, and the total neutron flux inside FLiNaK-ThF_4 test section. As shown, the thickness at 0.06 cm resulted in the largest number of fission neutrons production, after this value, it is clear that the number of fission neutrons start to decrease. Hence, this is the optimal value for the lithium target depth.

However, and as mentioned earlier, the target width is not the only important factor that impact the fission neutrons production and the fission events, lithium location inside the beam is an effective factor ad well.

Table 3.14: Neutron production for different target depths

^{7}Li thickness (cm)	Fission neutrons	Flux inside FLiNaK-ThF_4	Fission neutrons tracks
0.01	1.2844E+06	3.86E+06	104
0.02	2.6643E+06	7.09E+06	216
0.03	2.6726E+06	1.03E+07	217
0.04	2.8829E+06	9.32E+06	235
0.05	2.9564E+06	1.90E+07	240
0.06	2.9812E+06	1.98E+07	242
0.07	2.9191E+06	1.98E+07	237
0.08	2.8945E+06	1.98E+07	235
0.09	2.8698E+06	1.97E+07	233
0.1	2.8205E+06	1.97E+07	229

As a matter of fact, and as was proved in phases 6 and 7, the location plays a bigger role on the production of fission events and induced fission neutrons.

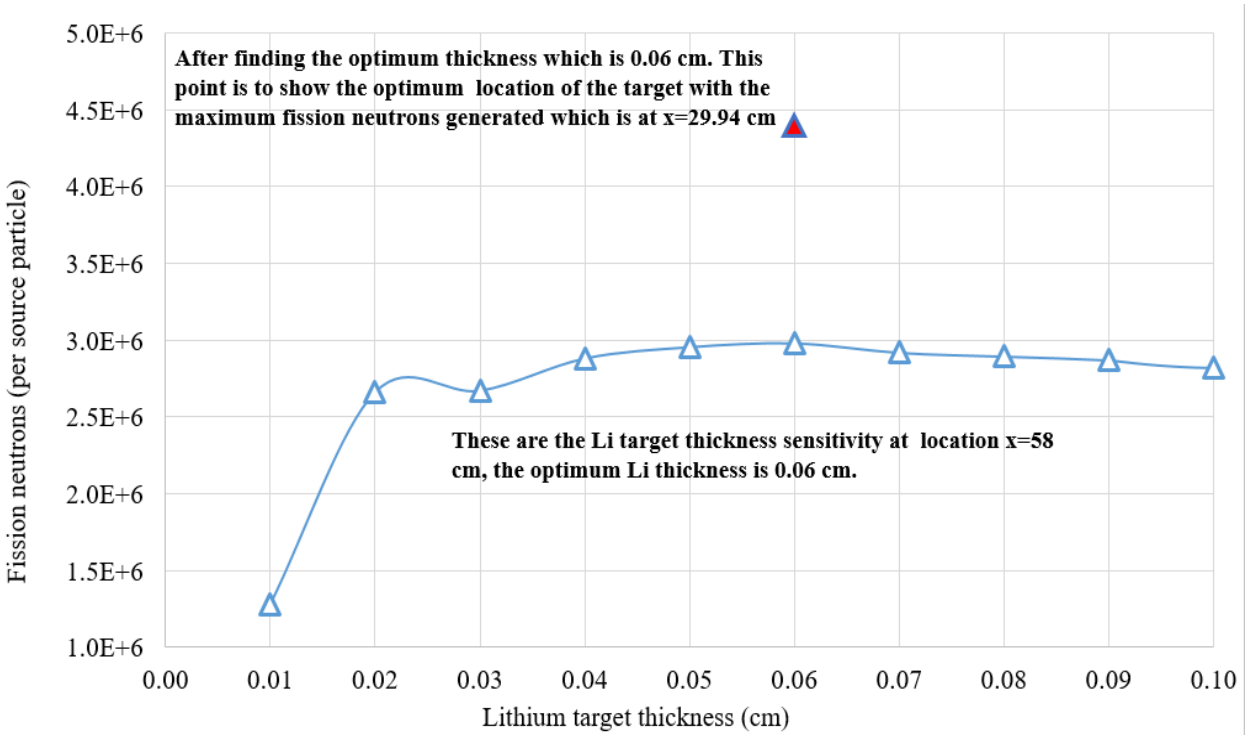

Figure 3.41: Target thickness sensitivity at the end of the beam

From here, the target was moved to the closest location, where it is attached to the test section (Z = 29.94 cm), to maximize the fission rate density. As shown in Figure 3.41, the blue curve shows the the number of fission neutrons at (Z = 28 cm), and the red point shows the number of fission neutrons for the optimum depth when target is attached to the test section (Z = 29.94 cm).

3.1.9 Phase 9

This phase studies the material options for the facility shielding, materials that were tested are: Poly-ethylene (PE) and borated poly-ethylene (BPE) (10%-B)[30]. The decision of selecting a shielding material and design was based on the results of the neutron flux in unit ($neutrons/cm^2.s$) and dose rates in detectors in unit of (Sv/yr and $mrem/hr$), detectors were placed both inside and outside of the facility shielding as shown in Figure 3.42.

A shielding box design of the tested materials with an initial thickness of 5 cm were tested, the full FLiNaK-ThF_4 loop with the chamber, stainless steel 316 piping, proton beam, and graphite shielding were built in the model of this phase. Cylindrical volume detectors and point detectors were added to measure the neutron flux on the both sides of the shielding. Wall dosimeters are placed outside the shielding to calculate the average dose rate, wall dose detectors are shown in Figure 3.43.

3.1.9.1 Phase 9 Results

Th 3D MCNP6 model is shown in Figure 3.44. At this stage, and after designing and obtaining the optimum proton accelerator shielding design, it is a necessity to build a shielding for the full facility including the beam, the beam shielding, and the molten salt loop, a 5 cm thickness wall for each material as an initial case was tesed, Figure 3.45 shows the neutron spectrum that leak out of the loop but still confined inside the shielding wall.

Figure 3.46 shows the neutrons spectrum for both materials in the surrounding air sphere. It is shown that the PE serves as a better shielding material; this is because the carbon concentration is larger than in the BPE, carbon has a large scattering cross section, hence, PE serves a a better moderator and reflector than BPE.

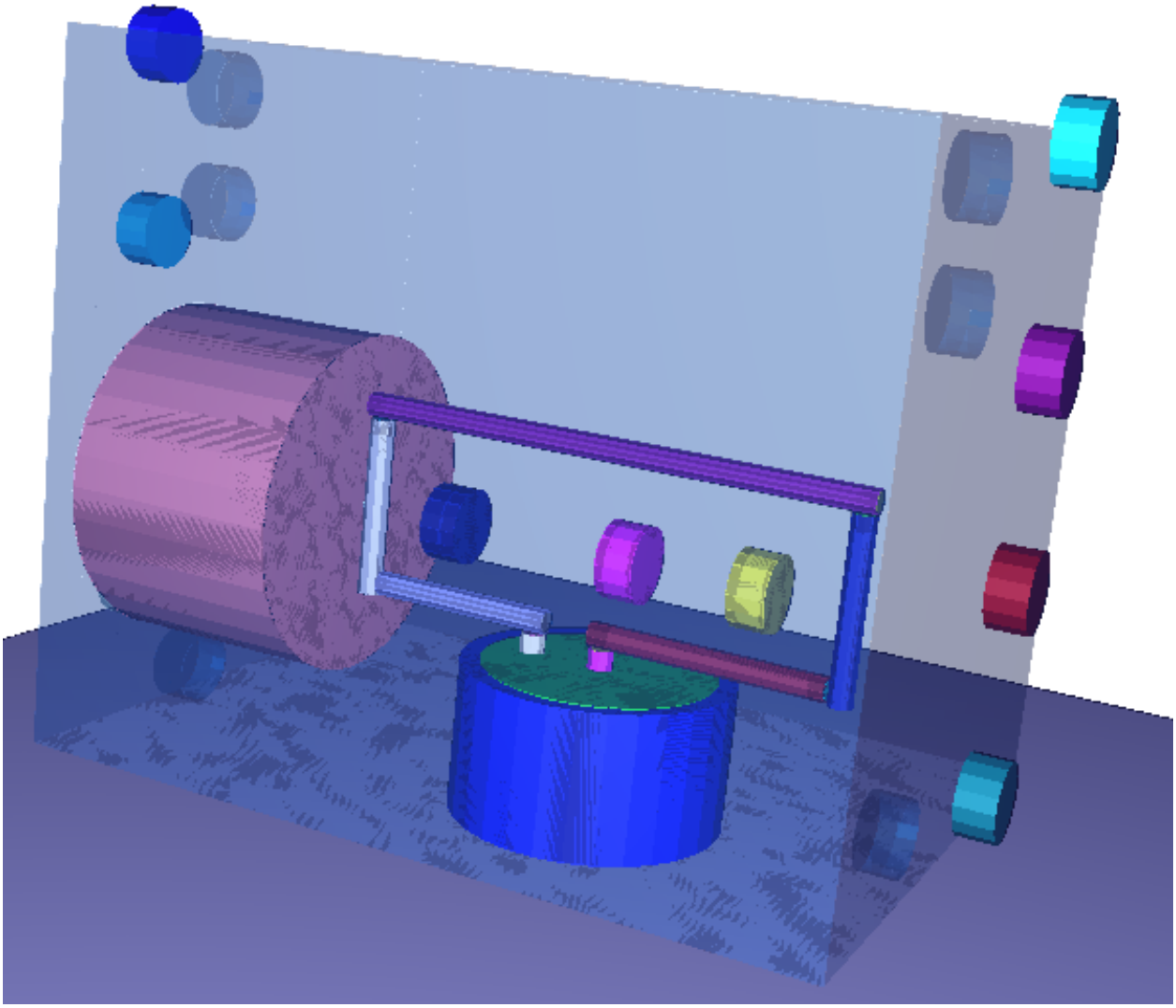

Figure 3.42: Cylindrical volume detectors placed on both side of the shielding

PE is composed of carbon and hydrogen, BPE is composed of carbon, hydrogen, and boron. The figures show neutron spectrum inside, and outside the shield.

It is shown at 4 MeV, the PE material seems to absorb neutrons more than the BPE, this is because at this energy, boron, carbon, and hydrogen have an absorption cross section of 5E-7 b, 2E-5 b, and 4E-5 b, respectively [31], and as a result, neutrons at this energy are absorbed by PE more than BPE.

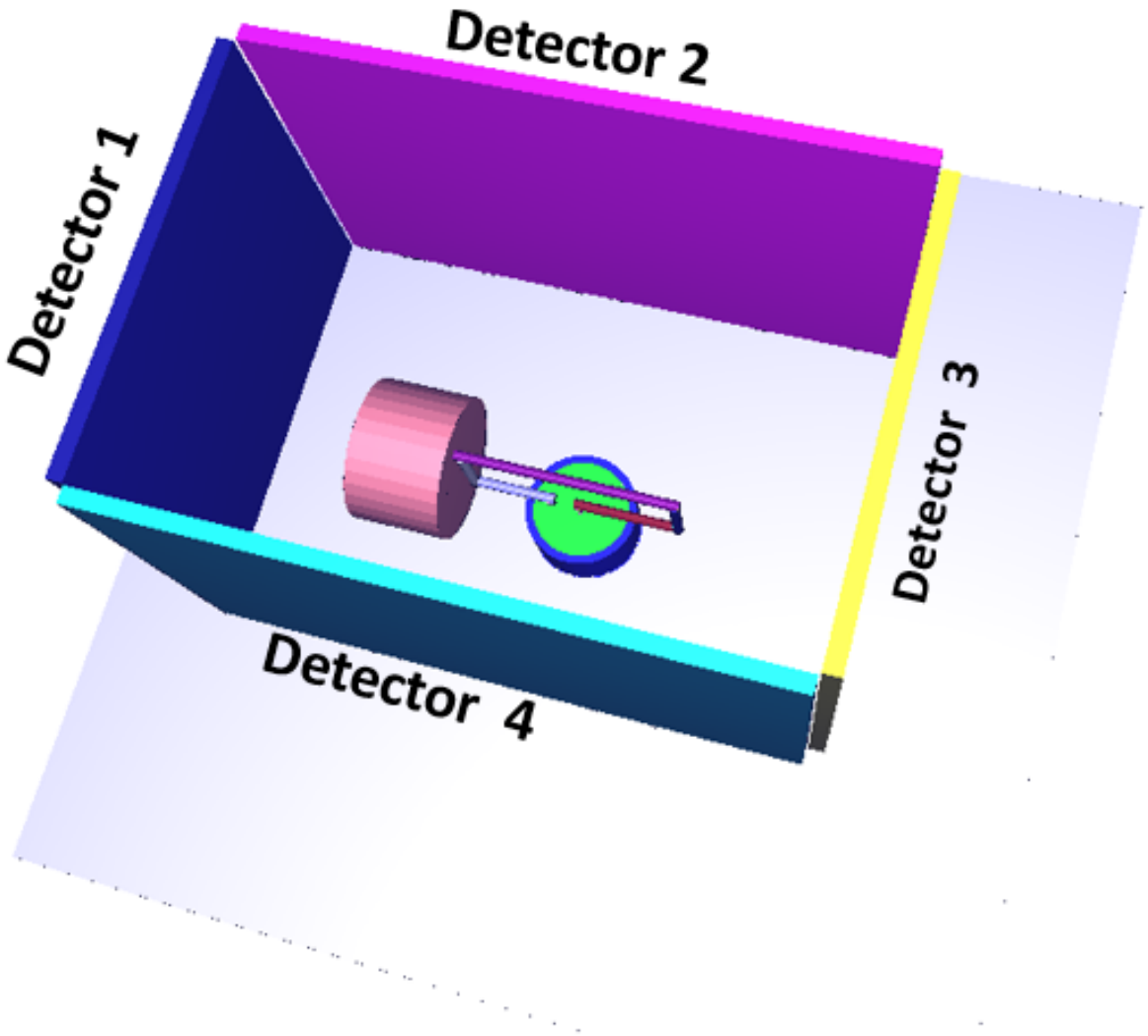

Figure 3.43: Four wall detectors placed outside the shielding

As shown from the results, the neutron energy spectrum is shifted to a lower energies when using the PE. PE is composed of 85% carbon and 15% hydrogen, not only carbon has a large moderation of neutrons, but also, carbon and hydrogen has a larger neutron absorption cross section than boron for energies between 1E-6 MeV and 8 Mev. From here, it can be said that PE was selected for the facility shielding. Thickness sensitivity was performed, five thicknesses were tested, starting at 10 cm, up to 50 cm with a 10 cm increment.

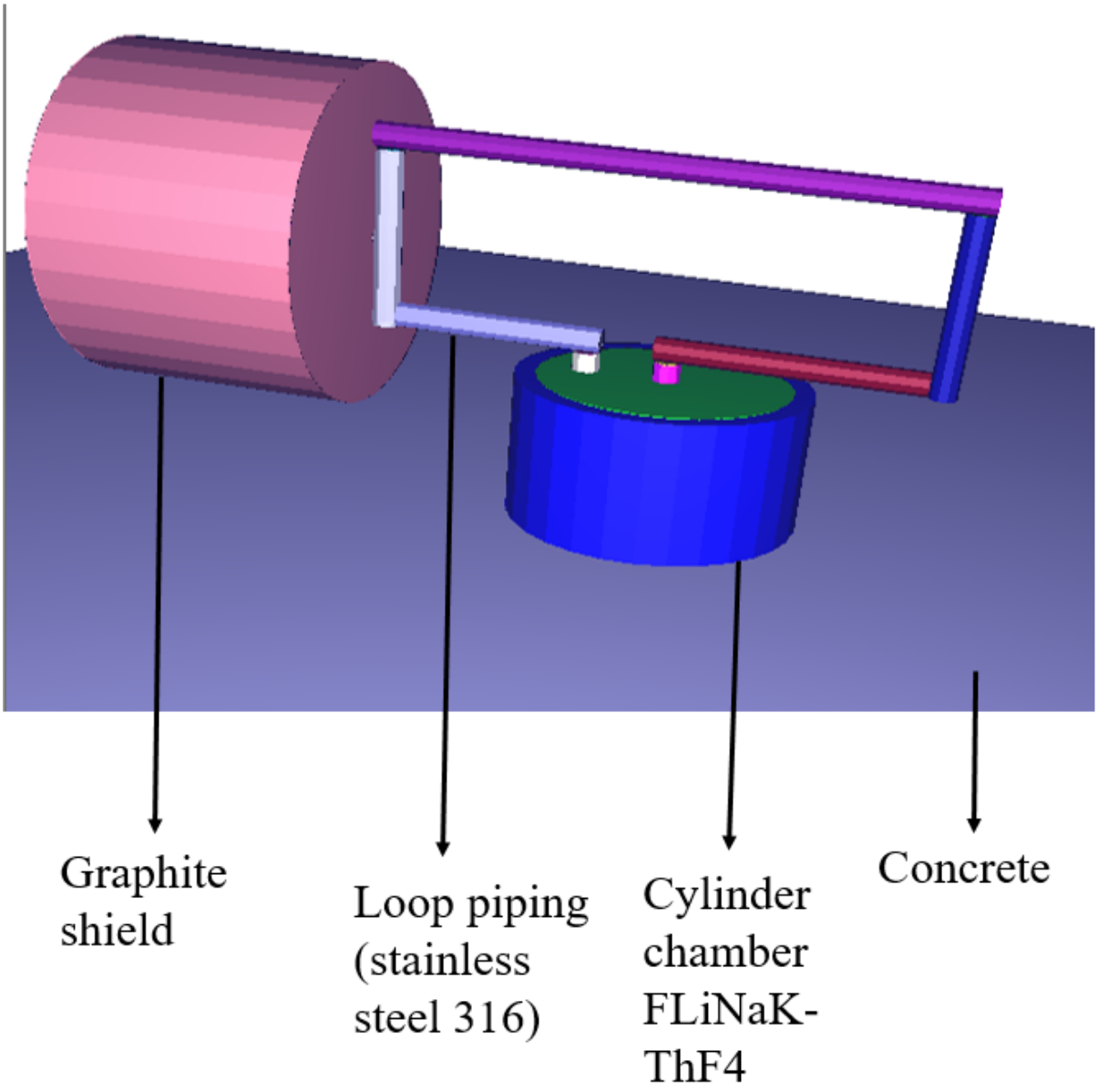

Figure 3.44: 3D MCNP6 model for the proton accelerator driven molten salt loop

Point detectors (F1 tally in MCNP6) were placed along the proton beam center line, 14 point detectors were distributed inside and outside the shield to calculate the dose rate in Sv/hr. Figure 3.47 shows 2D XZ cross-section of the molten salt loop facility, surrounded by the shield, and attached to the dose rate plot at each of the point detector for different thicknesses. It is clear that as the thickness increases, the dose rate at the point detectors decreases, it also shown how the

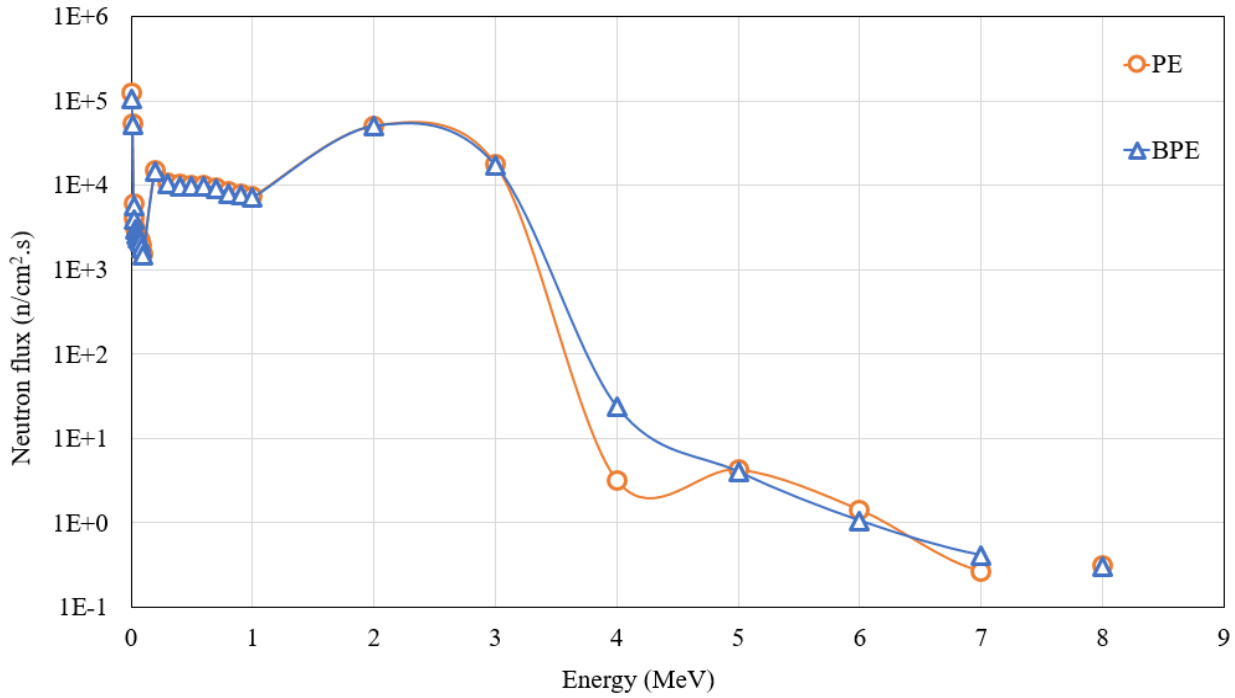

Figure 3.45: Neutron spectrum leak out of the loop

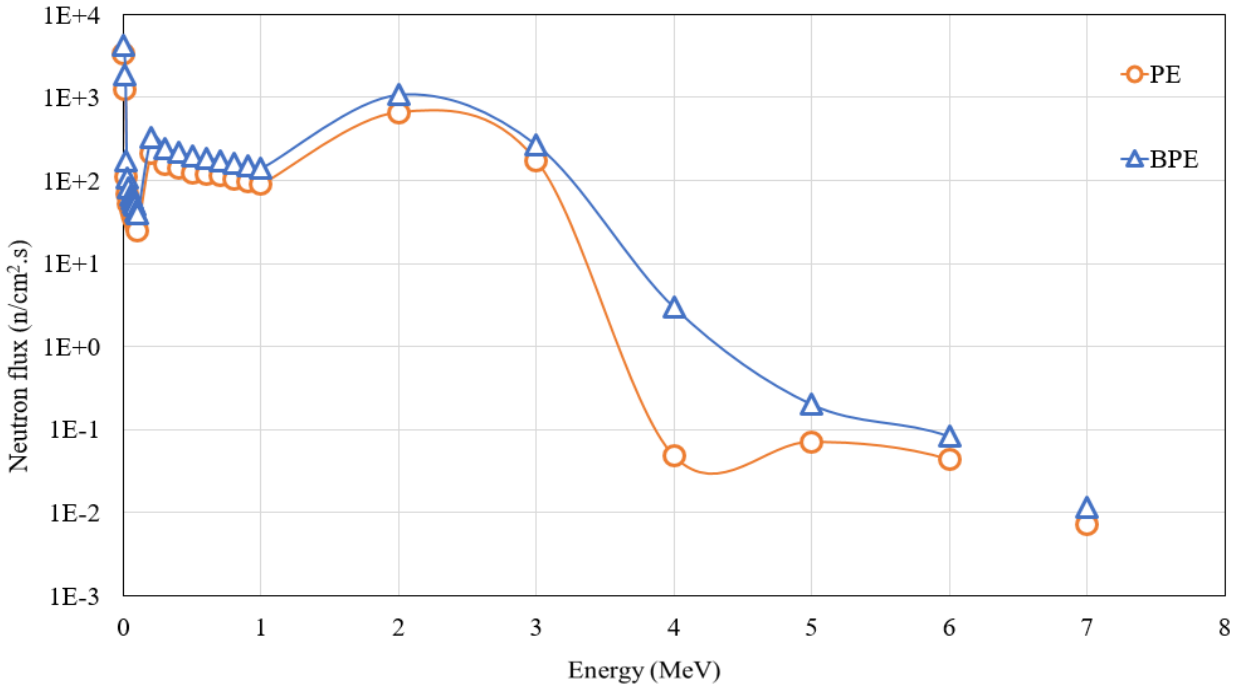

Figure 3.46: Neutron spectrum leak out of the shielding

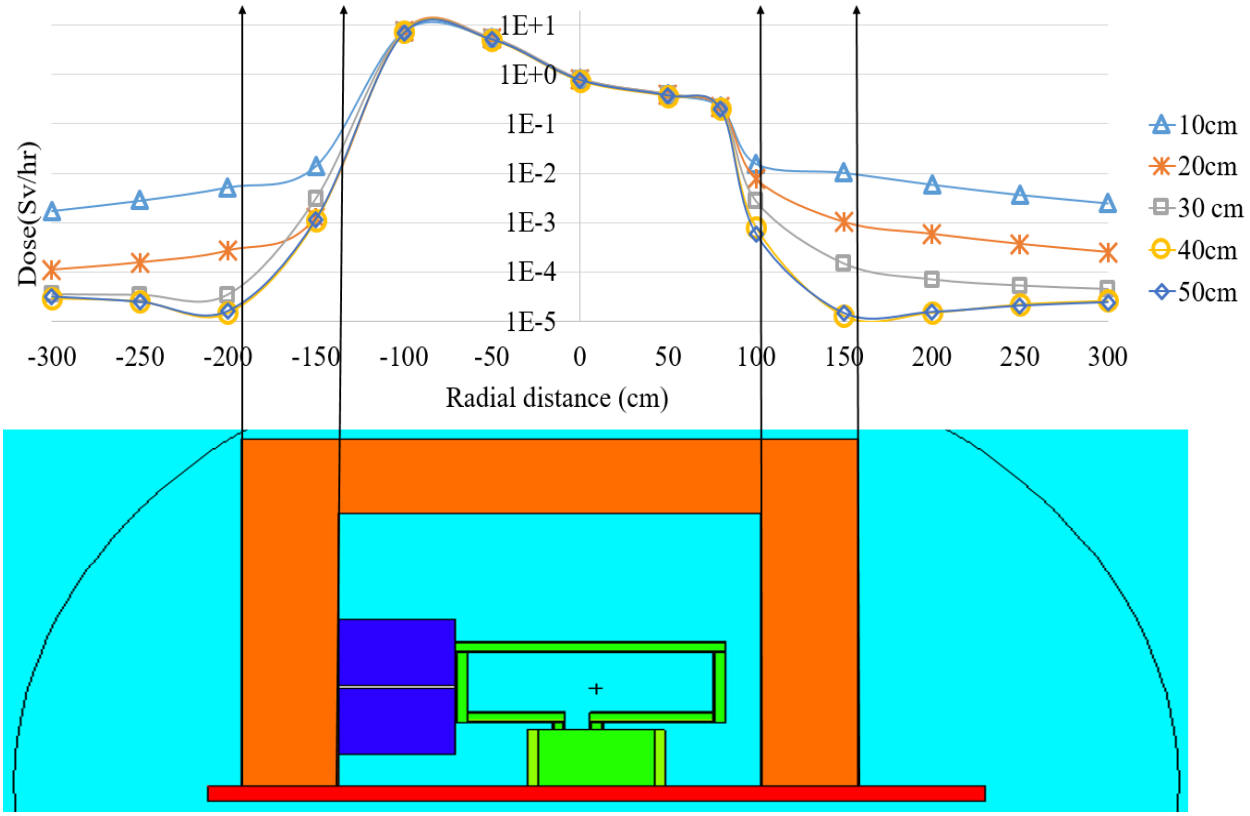

Figure 3.47: Point detectors dosimeter along the beam center line

dose rate curve behave when moving from the inner side of the shield (loop) to the outer side of the shield (outside atmosphere), the dose rate reduces drastically in the shielding environment.

However, another simulation with the borated-polyethylene was run, but with a lower boron concentration, where the percentage was reduce from 10% to 5%. A this stage, wall detectors design were used instead of the point detectors to calculate the average dose rate at the outer side of the shielding, four wall detectors were placed at the four sides of the shielding room.

Thickness perturbation for the shielding was performed for each of the three compositions, which are PE, BPE (10%B) , and BPE (5%B). Starting from 10 cm, up to 50 cm, with 10 cm increment for each of the three material configuration, the average dose was calculated in the wall dosimeters and results were compared together. Table 3.15 shows the carbon, hydrogen, and boron weight fraction for each of the shielding materials that were tested.

Comparing the results with the exposure limits defined by the International Commission on

Radiological Protection (ICRP), the annual dose was calculated. It was assumed that occupational workers (nuclear workers) work 2 hours a day, 3 days a week, 4 weeks a months, and 12 months a year, a total of 288 hours a year. Figure 3.48 shows the annual dose in unit of Sv/yr.

Table 3.15: Weight fraction for different shielding compositions

Composition	Carbon concentration (%)	Hydrogen concentration (%)	Boron concentration (%)
Poly	85.6284	14.3716	
Borated poly (10%)	77.4645	12.5355	10
Borated poly (5%)	82	13	5

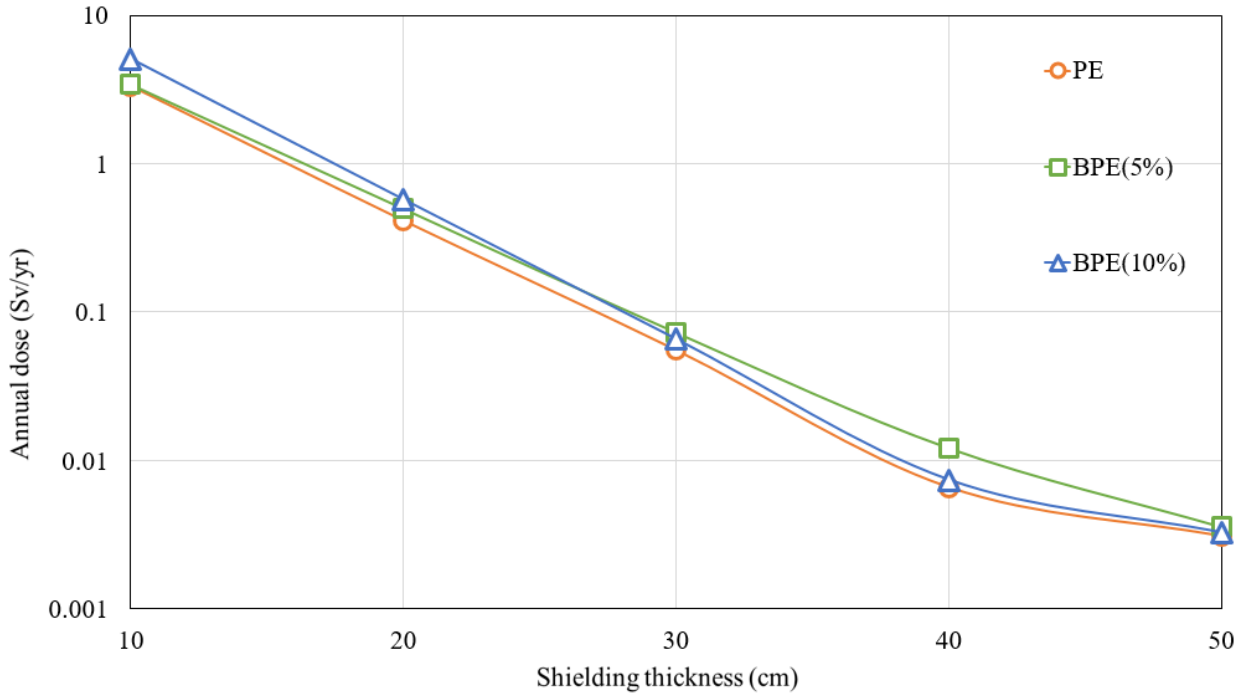

Figure 3.48: Annual dose (288 hours/year) as a function of shielding thickness

The ICRP exposure limits published in publication 60 [32] is shown in Figure 3.49, taking the ICRP occupational exposure limit, the annual dose should not exceed 20 mSv. Table 3.16 shows

the average annual dose exposure at different thicknesses assuming workers spend 288 hour/year being exposed to radiation caused by the test loop facility. It is shown from the table below, and as proved earlier, the PE is the best shielding material, and 40 cm thickness and is the optimum design. It has to be noted that the dose rate calculated by the MCNP6 code is in unit of Sv/hr, values in the table are for the number of hours assumed above. However, these numbers can change based on the number of hours per year a worker get exposed to radiation.

The PE composition at thickness of 40 cm can be a challenge cost-wise and space-wise. As mentioned above, this can be controllable by changing a several factors; either by minimizing the number of working hours, decreasing the proton beam energy, strength, or changing the target location. One of the suggested approaches is to reduce the number of working hours will be analyzed in phase 10.

Criteria	NCRP-116	ICRP-60
Occupational Exposure		
Effective Dose Annual	50 mSv	20 mSv
Effective Dose Cumulative	10 mSv × age (y)	100 mSv in 5 years
Equivalent Dose Annual	150 mSv lens of eye; 500 mSv skin, hands, feet	150 mSv lens of eye; 500 mSv skin, hands, feet
Pregnant	5 mSv	2 mSv
Public Exposure		
Effective Dose Annual	1 mSv if continuous 5 mSv if infrequent	1 mSv; higher if needed, provided 5-y annual average ≤ 1 mSv
Equivalent Dose Annual	15 mSv lens of eye; 50 mSv skin, hands, feet	15 mSv lens of eye; 50 mSv skin, hands, feet

Figure 3.49: Exposure limits fro NCRP report No.116 and ICRP publication 60 [32]

Table 3.16: Annual dose for different shielding compositions at different thickness

Thickness (cm)	PE annual expouse (Sv/yr)	BPE annual expouse ($5\%B$)(Sv/yr)	BPE annual expouse ($10\%B$)(Sv/yr)
10	3.328 >0.02	3.417 >0.02	5.056 >0.02
20	0.411>0.02	0.497 >0.02	0.570 >0.02
30	0.055 >0.02	0.073 >0.02	0.065 >0.02
40	0.006 <0.02	0.012 <0.02	0.007 <0.02
50	0.003 <0.02	0.003 <0.02	0.003 <0.02

3.1.10 Phase 10

A Poly-ethylene shielding design sensitivity is carried out in details, Figure 3.50 shows an XY cross-section of the shielding thickness perturbation using the PE composition. A comparison of the average neutron spectrum between the inside and outside the shield was performed. Also, since detectors are located at different positions and orientations with the respect to the proton beam angle, each side will have a different shield thickness depending on its location. Annual dose rate (Sv/yr) obtained from dosimeter that were located outside the shielding were compared to the annual exposure limits set by ICRP-Publication 60 [32], not only that, but also the hourly dose rate ($mrem/hr$) was obtained and compared to the exposure limits followed by the Nuclear Science Center (NSC) staff.

3.1.10.1 Phase 10 Results

A comparison for the average neutron spectrum was performed between the area inside the PE shield, and outside in detector number 3 as shown in Figure 3.51. The plot shows the inversely proportional relationship between the neutron spectrum in detector 3, and the PE shield thickness, it is shown that at 40 cm, neutrons at energies larger than 5 MeV disappear, and at 50 cm, the maximum neutron energy is 4 MeV, while the spectrum in the inner region (inside shielding) has a maximum energy of 8 MeV.

As said earlier, 40 cm PE wall is a little challenging regarding cost and space, a new assumption was considered in order to meet the ICRP annual exposure limit.

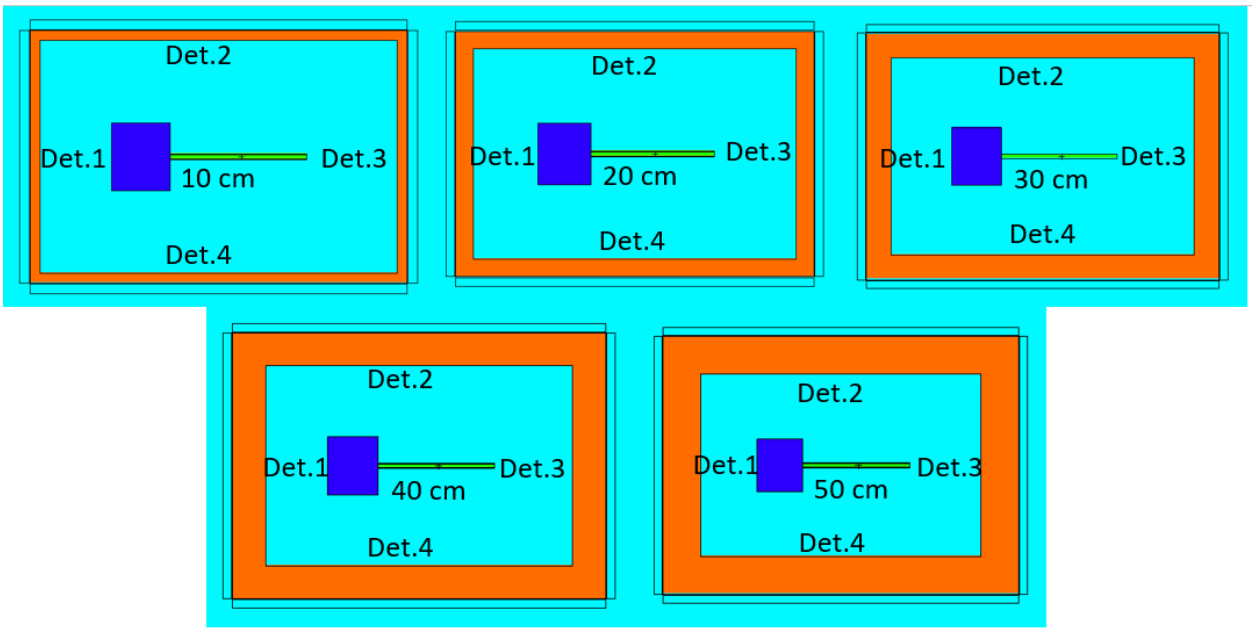

Figure 3.50: Four wall detectors placed outside the shielding

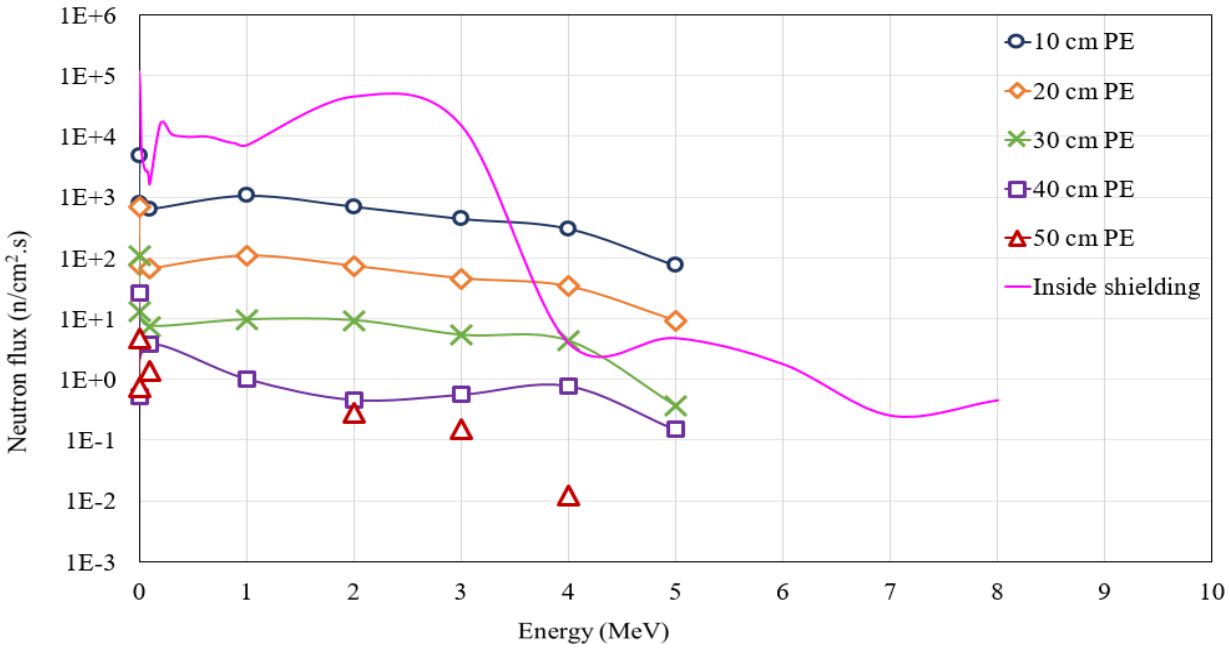

Figure 3.51: Comparison for the average neutron energy spectrum inside and outside the shield (detector)

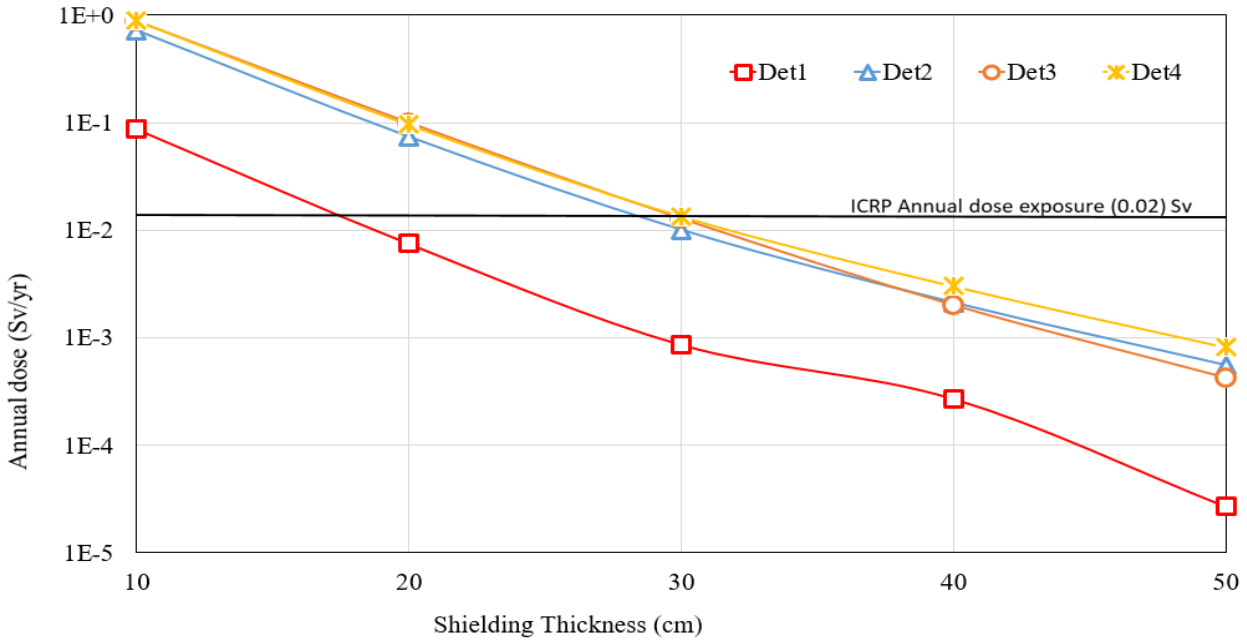

Figure 3.52: Annual dose (100 hours/year) as a function of shielding thickness

Nuclear workers are assumed to work no more than 100 hours a year instead of 288 hours a year. Figure 3.52 shows the annual dose rate in Sv/yr for a total of 100 working hours. When reducing the number of hours per year, the annual dose rate is shifted tremendously to lower values, as a results, reduce space and cost of required shielding.

However, it is more conservative to account for the hourly dose rate to ensure extreme safety for occupational workers. For safety purposes, shielding will be designed and optimized based on the hourly dose rate exposure limit followed by the Nuclear Science Center (NSC) at the Texas A& M University which is 1.25 $mrem/hr$, Figure 3.53 shows the hourly dose rate for the four detector surrounding the facility.

The facility will need about 30 cm (or slightly less) on the side behind the beam, about 40 cm (or slightly less) on the front and the right side of the beam, and more 50 cm of PE at the side of the second detector. Also, another approach was followed, as mentioned in the previously, to try minimizing the PE shielding load required, which is the proton beam energy, it is an effective factor that can shift average dose rate workers get exposed to.

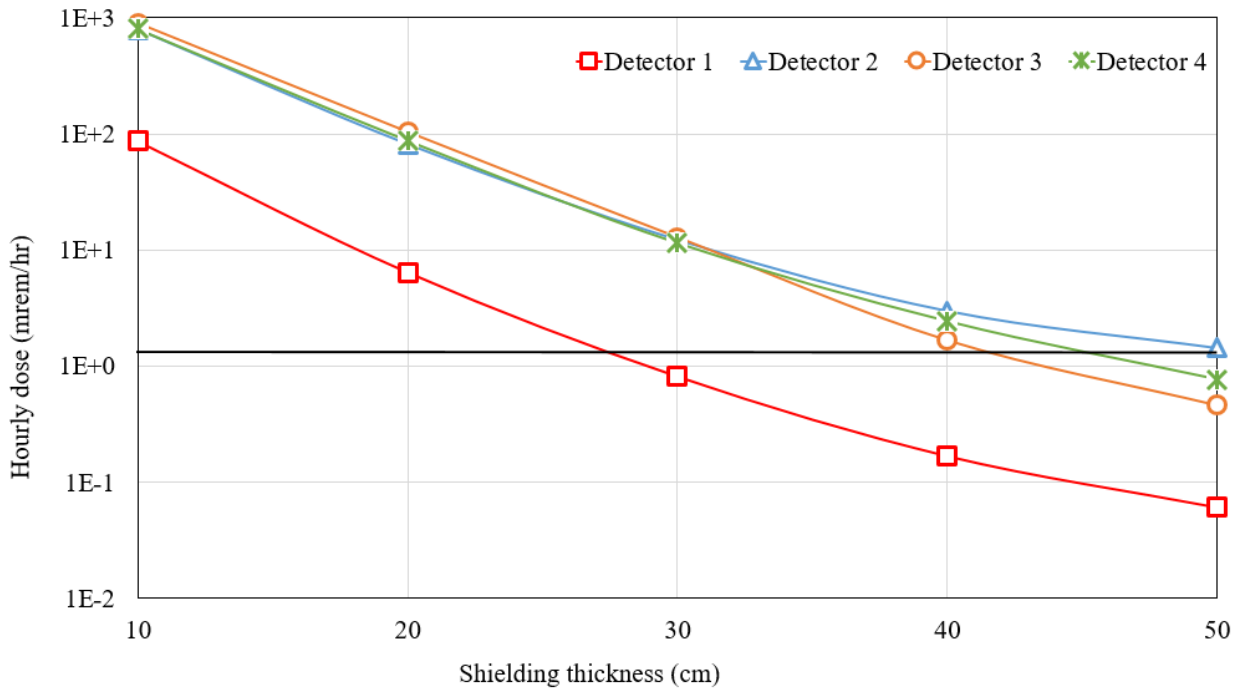

Figure 3.53: Hourly dose rate as a function of shielding thickness for 4.5 MeV source energy

Hence, the beam energy is reduced from 4.5 MeV to 2.5 Mev, so that lower energy neutron flux FLiNaK-ThF_4 is produced, and as a result, a lower dose rate regardless of detector location. Another sensitivity was run for 2.5 MeV proton source. Figure 3.54 shows the hourly dose rate for a 2.5 MeV proton beam, at this source energy, 20 cm PE wall will suffice behind the proton beam, and a 30 cm PE wall for the other 3 detectors. From here, it can be concluded that this shielding design is the optimum design for the molten salt loop facility at a proton beam energy of 2.5 MeV.

As mentioned in the early stages of the research, the proton beam should be operating at high energy relatively to produce neutrons carrying energies above the fast fission threshold, and as a result, maximize the fast fission events probability. So, other approaches may also be followed to try reducing the amount of PE shield load that should be installed at the facility, like building a complex geometry design for the shield, or use a double shielding slabs with different material composition, or enhance shielding at the corners where neutron may escape.

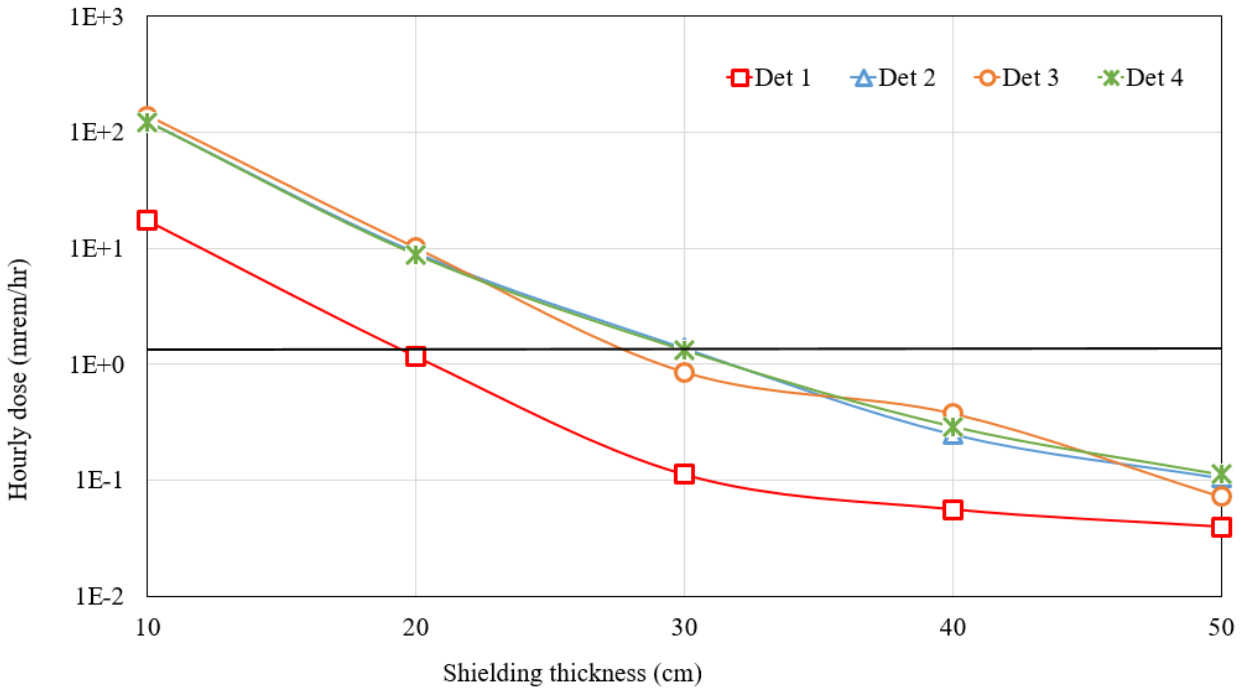

Figure 3.54: Hourly dose rate as a function of shielding thickness for 2.5 MeV source energy

3.2 SERPENT2 Simulations Results

Some SERPENT2 simulations were run to validate the MCNP6 model and benchmark the results of the MCNP6 code. To compare the two codes, it is necessary to apply the same input data such as; geometry design, materials, number of particle history, tallies, and the same source configuration in the input deck. The SERPENT2 geometry model was built using surface and cell cards, dimensions and parameters as the same as in the MCNP6 models. Geometry parameters, problem set up and source structure are shown in the Table 3.17. Same materials were used but different cross section data library, in MCNP6, calculations are done using ENDF-B7 cross section data library. However, JEFFF3.1.1 cross section data library is the database used in SERPENT2 calculation. Several cases were run in order to validate and benchmark the MCNP6 model and results. The mesh plotter feature in SERPENT2 Monte Carlo code was used to plot the neutron energy spectrum, this capability can be used in reactor physics applications to visualize the neutron thermalization on fission rate, bright and dark indicate low and high values, respectively.

Table 3.17: Characterization of SERPENT2 Model

Source structure	Beam design	Target specification	Loop shielding
Neutron	Radius of 1.27 cm	^{7}Li	Box design
Isotropic	Length of 60 cm	Radius of 1.27 cm	Thickness sensitivity
1.0758E+10 n/s	Stainless steel 316	Thickness sensitivity	PE and BPE
Square disc	Graphite shielding	location sensitivity	Detectors inside and outside

3.2.1 Source Conversion And Geometrical Design

SERPENT2 Monte Carlo code does not support protons, hence, a bare case geometry for proton source was run in MCNP6, the output file was extracted and converted to an input data in SERPENT2 input deck. Results from SERPENT2 are compared with results from both neutron and proton source in MCNP6. Running simulations with SERPENT2 Monte Carlo code was used for two purposes; first is to validate SERPENT2 model with the MCNP6 model, and second is to benchmark the results from MCNP6, hence, making the results reliable, this is important specially when there are no experimental results. SERPENT2 simulations were run to benchmark results of the shielding material composition, shielding design, and the target optimum thickness and location to maximize the ^{232}Th fast fission reaction rate.

To convert the proton to neutron source, a bare case geometry was run in MCNP6, 4.5 MeV, 2 $\mu Amps$ proton source was subjected into a ^{7}Li target with the optimum thickness obtained, which is 0.06 cm located at the very end of the proton beam, surrounded by a 400 cm air sphere radius. The output was extracted and converted into energy weighted neutron source for SERPENT2, the produced neutron energy spectrum form MCNP6 is shown in Figure 3.55, and the energy probability is shown in Figure 3.56.

As shown above, the maximum neutron energy produced is at 3 MeV, with a peak at 1.3 MeV, and the total number of neutron produced is 1.0758E+10. This energy weighted neutron spectrum is used as the characteristics of the external neutron source in the SERPENT2 input deck with a source strength of 1.0758E+10 n/s. The SERPENT2 model including the design, geometry, and parameters were defined similar to the MCNP6 model, the JEFF.3.3.1 [33] data library was used.

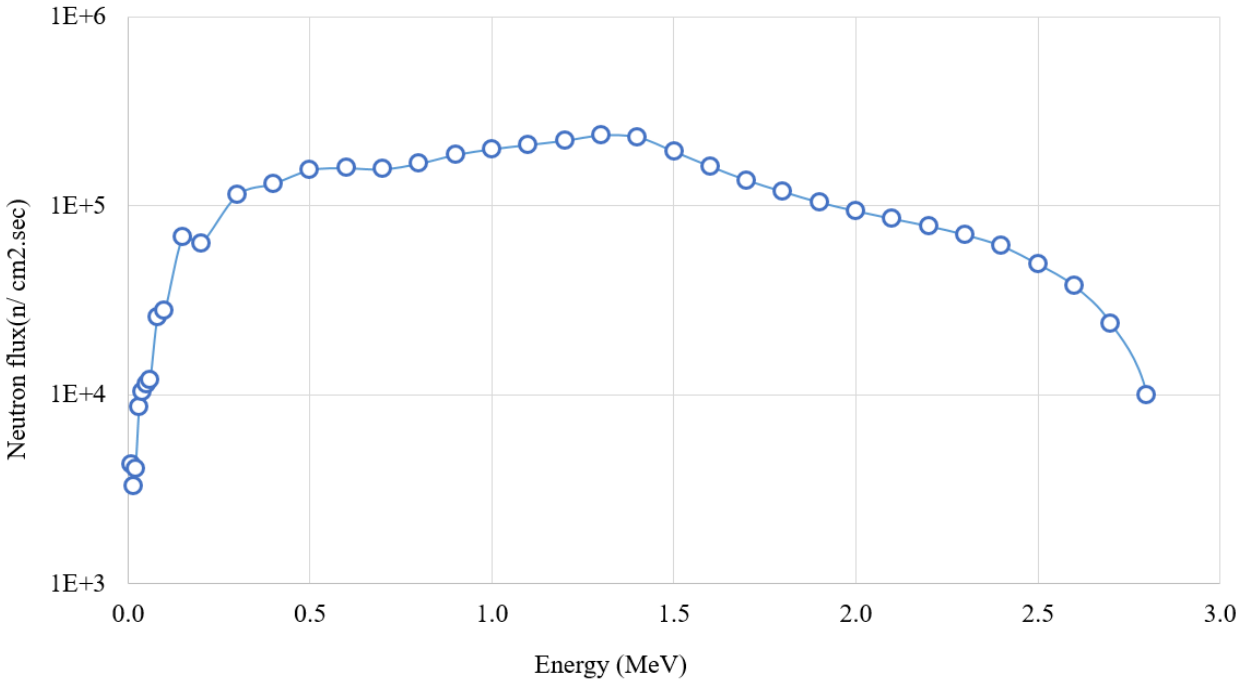

Figure 3.55: The produced neutron energy spectrum using MCNP6

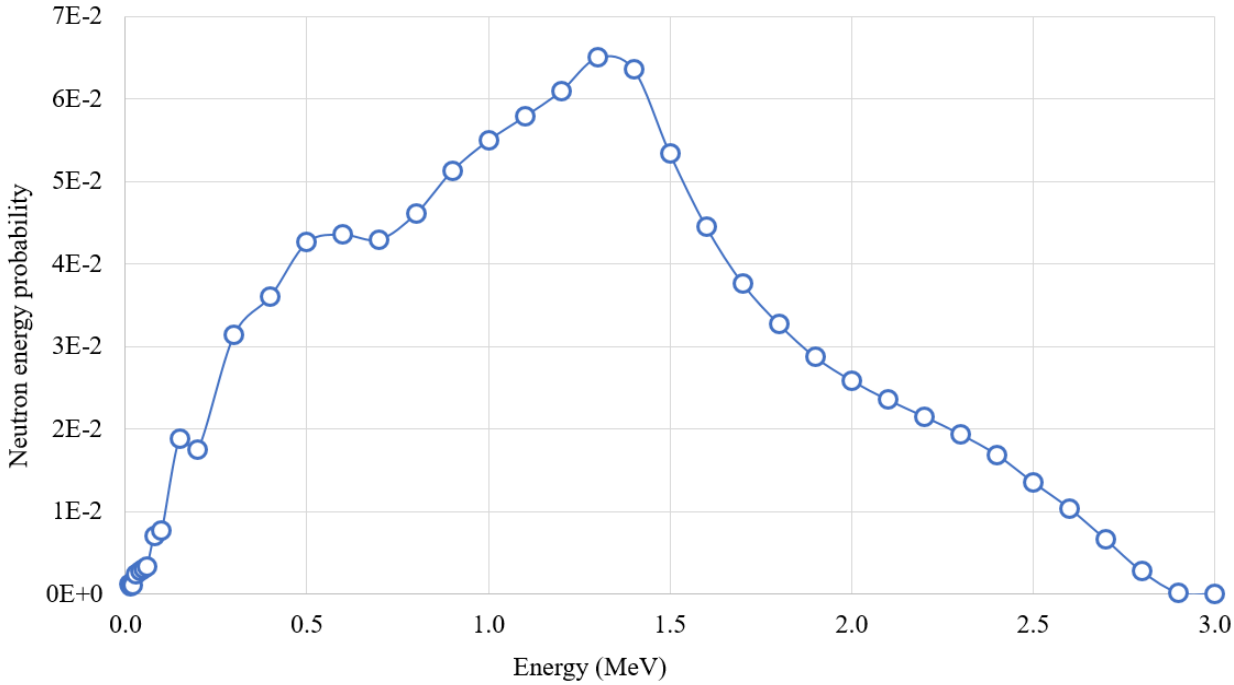

Figure 3.56: The produced neutron energy probability using MCNP6

3.2.2 Shielding Material Specification

The same materials were tested with a thickness of 5 cm shielding wall in SERPENT2 as in MCNP6 code. Figure 3.57 shows the neutron spectrum that leak out of the shielding walls into the outer air atmosphere with SERPENT2 code. Results from SERPENT2 also shows that PE serves as a better shielding material composition than the BPE. It should be noted that the maximum neutron energy here is 10 MeV, these results benchmark results from MCNP6, and so, it can be said that PE is better than BPE with a reliable results.

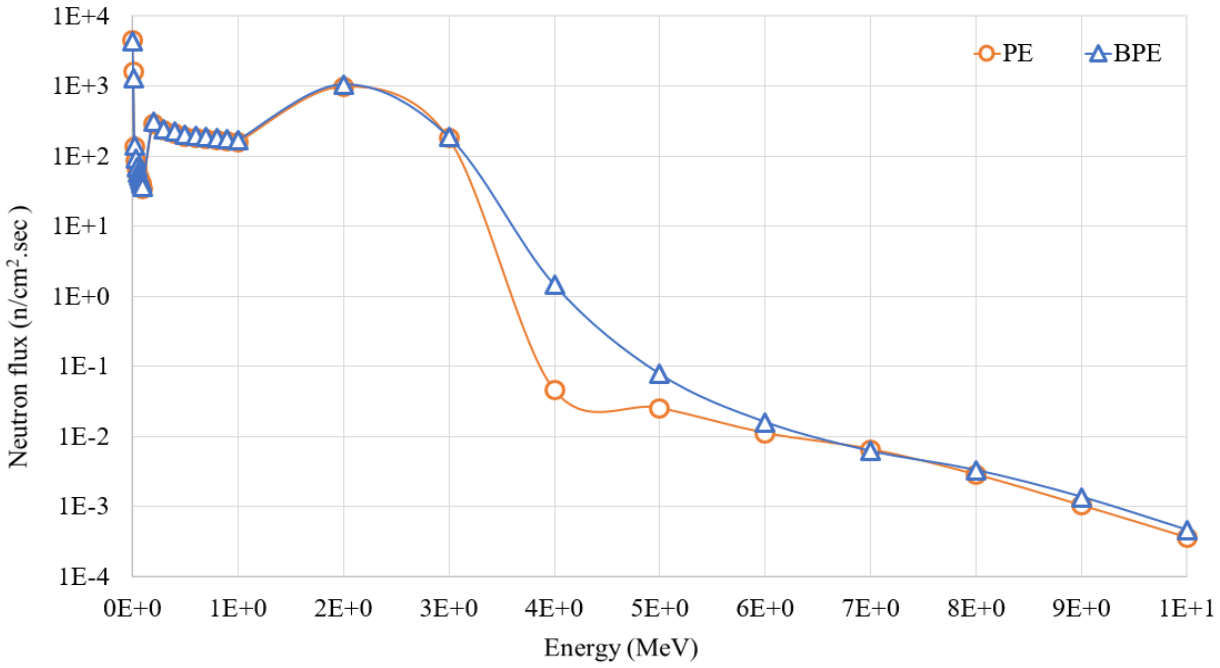

Figure 3.57: Neutron spectrum leak out of the shielding for a neutron source using SERPENT2

3.2.3 Shielding design sensitivity analysis

A SERPENT2 model was built with the same settings and parameters as in the MCNP6 model. After choosing the shielding material, shielding thickness sensitivity analysis was performed in SERPENT2 to benchmark the optimum shield thickness. Five PE shield thicknesses were tested,

these are 10 cm, 20 cm, 30 cm, 40 cm, and 50 cm as shown in Figure 3.58. It is clear that as the shield thickness increases, the average neutron spectrum decreases, the maximum neutron energy is 5 MeV at 10 cm, 3 MeV at 20, 30, and 40 cm, and 1 MeV at 50 cm.

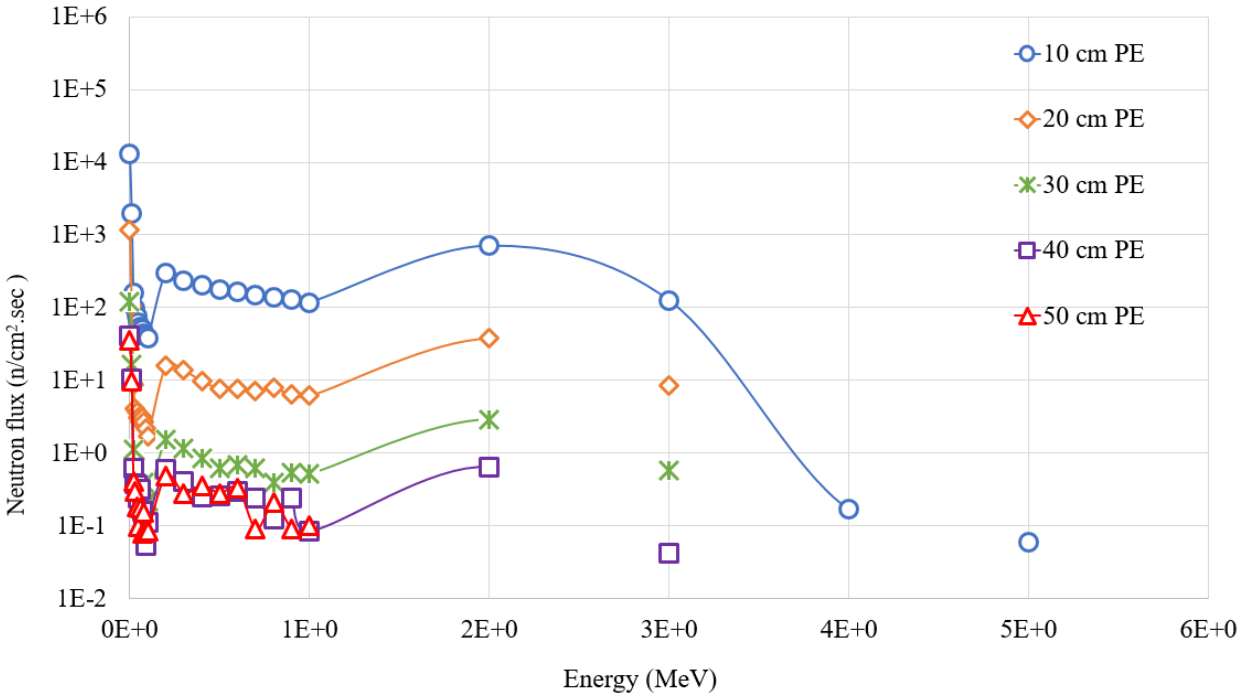

Figure 3.58: Average Neutron spectrum in the detector as a function of PE thickness using SERPENT2

3.2.4 Lithium target sensitivity analysis

The optimum lithium thickness was obtained earlier using MCNP6 code, the same target thickness investigation as was done in MCNP6 to compare the results between the two codes. The same sensitivity was tested in SERPENT2, the target was located at a close location to the FLiNaK-ThF_4 test section about 2 cm away from the test section (Z = 28 cm in the simulation), thickness sensitivity starts at 0.01 cm up to 0.1 cm with a 0.01 cm step. Figure 3.59 shows the number of fission neutrons produced in the test section as a function of the target thickness. It is shown that the optimum thickness is 0.06 cm when the target is located at Z = 28 cm in the simulation.

However, the distance between the target and the test section is an effective factor as mentioned, hence, the target is also attached to the test section (Z = 29.94 cm) to ensure the maximum fission neutrons production.

Figure 3.60, and Figure 3.61 shows the target at Z = 28 cm, and at Z = 29.94 cm, respectively. The mesh plotter feature in SERPENT Monte Carlo code was used to plot the neutron energy spectrum; where the red and yellow hot shades represent the relative fission power (fission rate) distribution, and the blue cold shades represent the relative thermal flux (flux below 0.625 eV) distribution .The mesh plotter capability in SERPENT2 can be used in reactor physics applications to visualize the neutron thermalization on fission rate, bright and dark indicate low and high values, respectively.

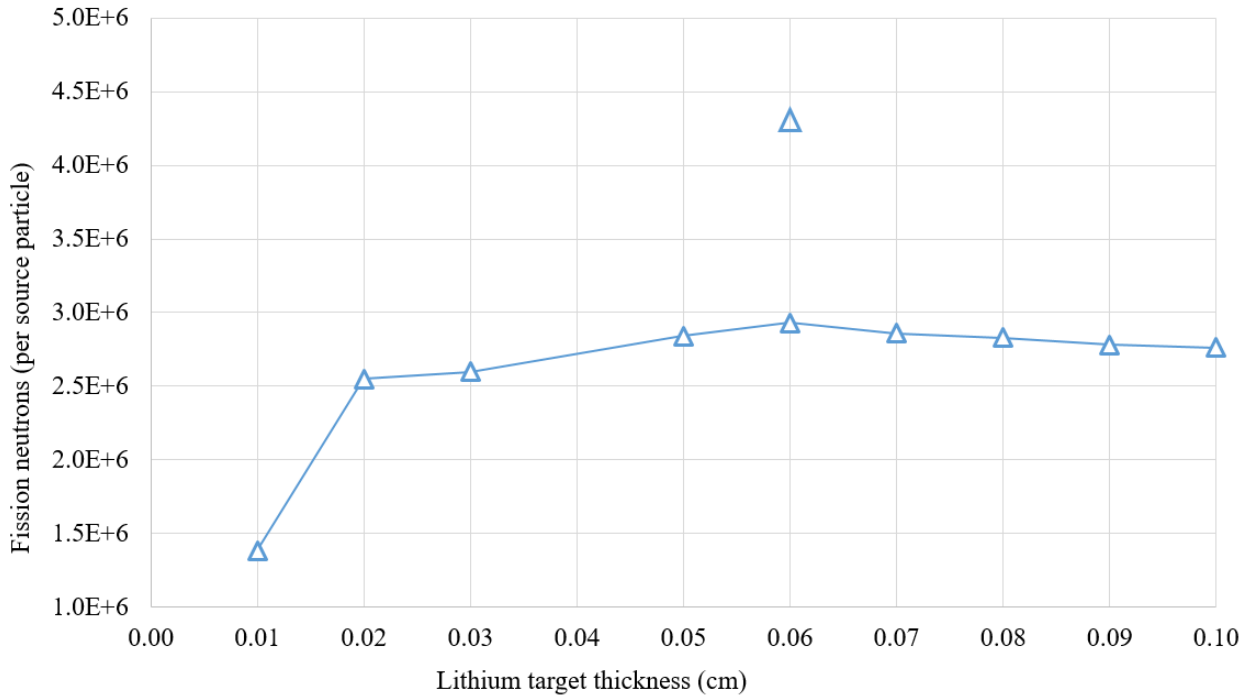

Figure 3.59: Target thickness sensitivity at the end of the beam using SERPENT2

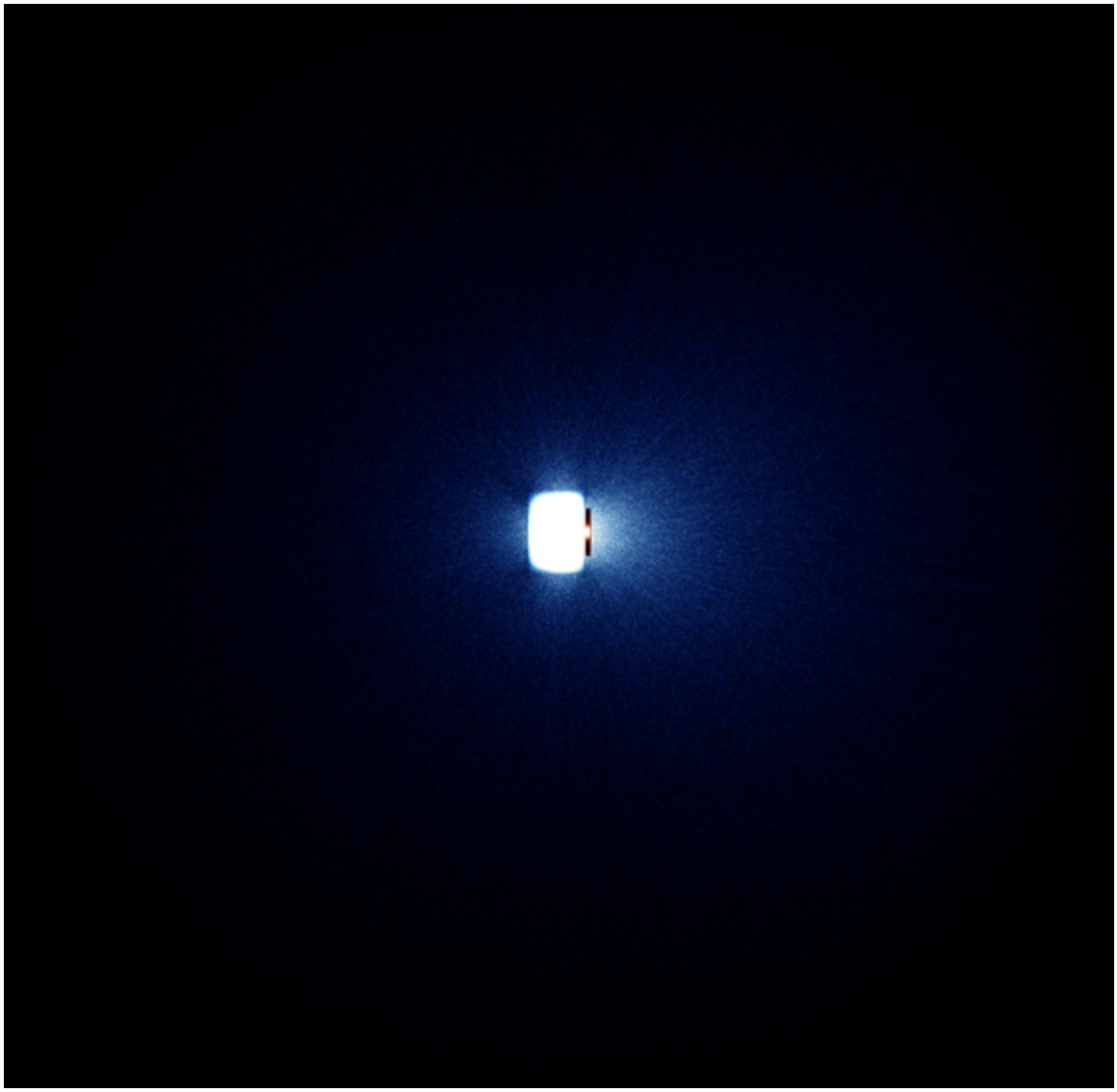

Figure 3.60: Neutrons produced using mesh plotter SERPENT2 where target is at the end of the beam

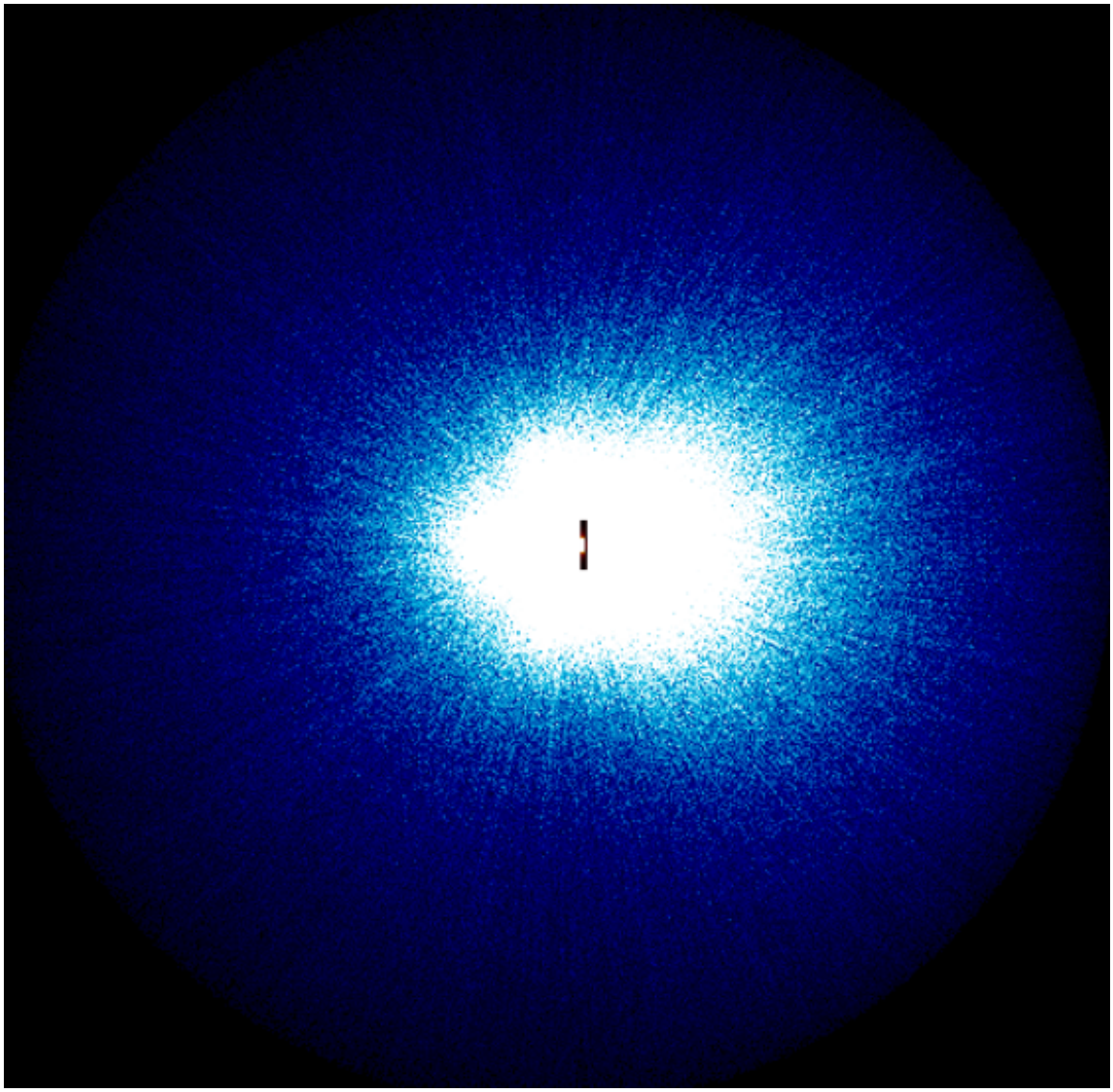

Figure 3.61: Neutrons produced using mesh plotter SERPENT2 where target is attached to the test section

4. DISCUSSION AND CONCLUSIONS

4.1 Shielding Material Composition Bench Marking

Comparing the neutron spectrum leak between the neutron source model in SERPENT2 as shown in Figure 4.1, and the proton source model in MCNP6 as shown in Figure 3.46, the neutron spectrum behavior and magnitude are in a good agreement. However, it should be noted that the maximum neutron energy that leak out of the shielding for the neutron source in the SERPENT2 model is 10 MeV, while it is 7 MeV in the proton source MCNP6 model. This is regarding the the source definition in the two cases, when running an MCNP6 simulation applying a neutron source with the same definition as in the SERPENT2 simulation, the neutron spectrum will have the similar behavior and very close results in the two codes, the neutron source MCNP6 model is shown in Figure 4.2.

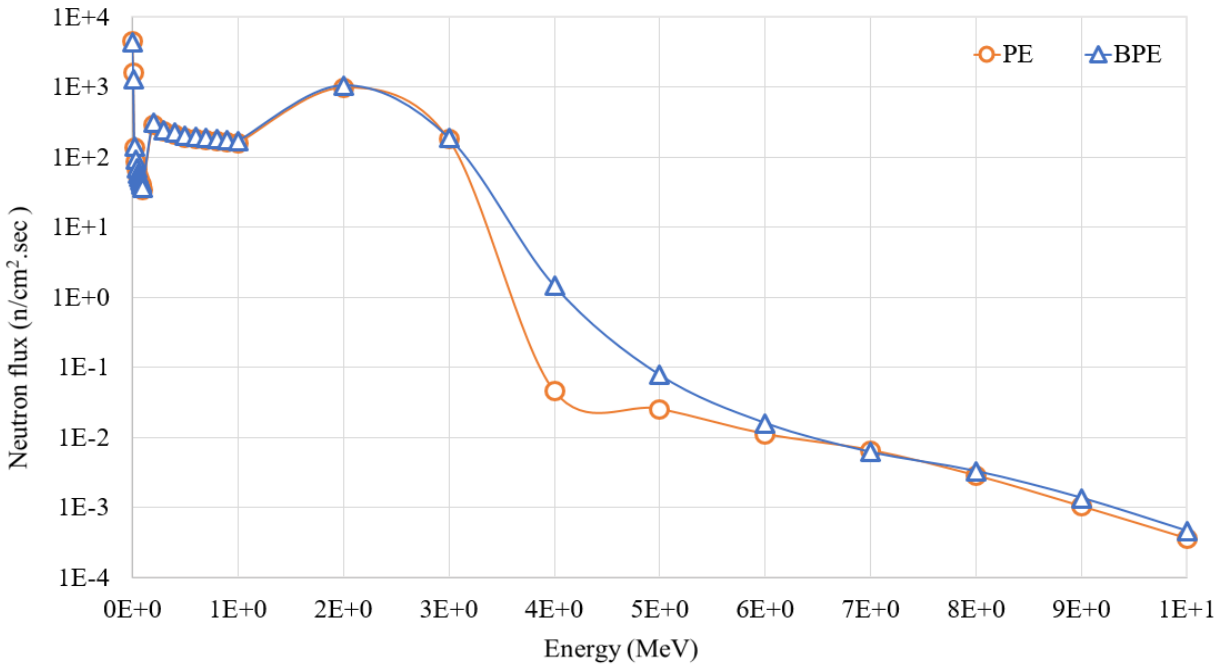

Figure 4.1: Neutron spectrum leak out of the shielding for a neutron source using SERPENT2 code

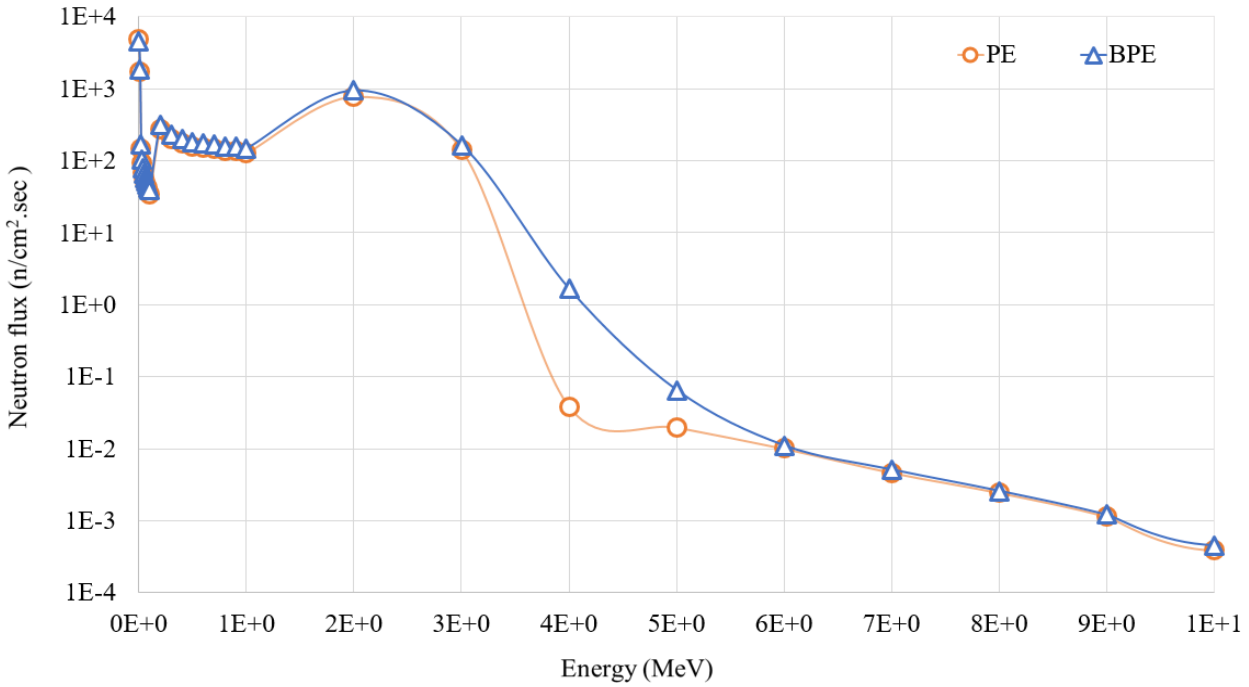

Figure 4.2: Neutron spectrum leak out of the shielding for a neutron source using MCNP6 code

Defining the same source in the two codes give results in a very good agreement,hence, Figure 4.1 and Figure 4.2 show the a very similar neutron spectrum for a neutron source in SERPENT2 and MCNP6, respectively. A comparison for the neutron spectrum leak out of shielding, and the neutron spectrum in the FLiNaK-ThF4 test section for the three source definitions in both MCNP6 and SERPENT2 is shown in Figure 4.3 and Figure 4.4, respectively.

The maximum neutron energy depends on the external source particle type, defining a proton with a specific energy and strength resulted in a maximum neutron energy of 7 MeV that leak out of the loop with a flux of almost 1E-2 $n/cm^2.sec$, and a max of also 7 MeV inside the test section with a flux of almost 1.5E+2 $n/cm^2.sec$. However, defining a neutron source with equivalent energy and strength will result a maximum energy of 10 MeV with a flux of almost 1.5E-4 $n/cm^2.sec$ that leak out of the loop, and a maximum of 10 MeV with a flux of almost 1.5E0 $n/cm^2.sec$ inside the test section, either using MCNP6 or SERPENT2 code.

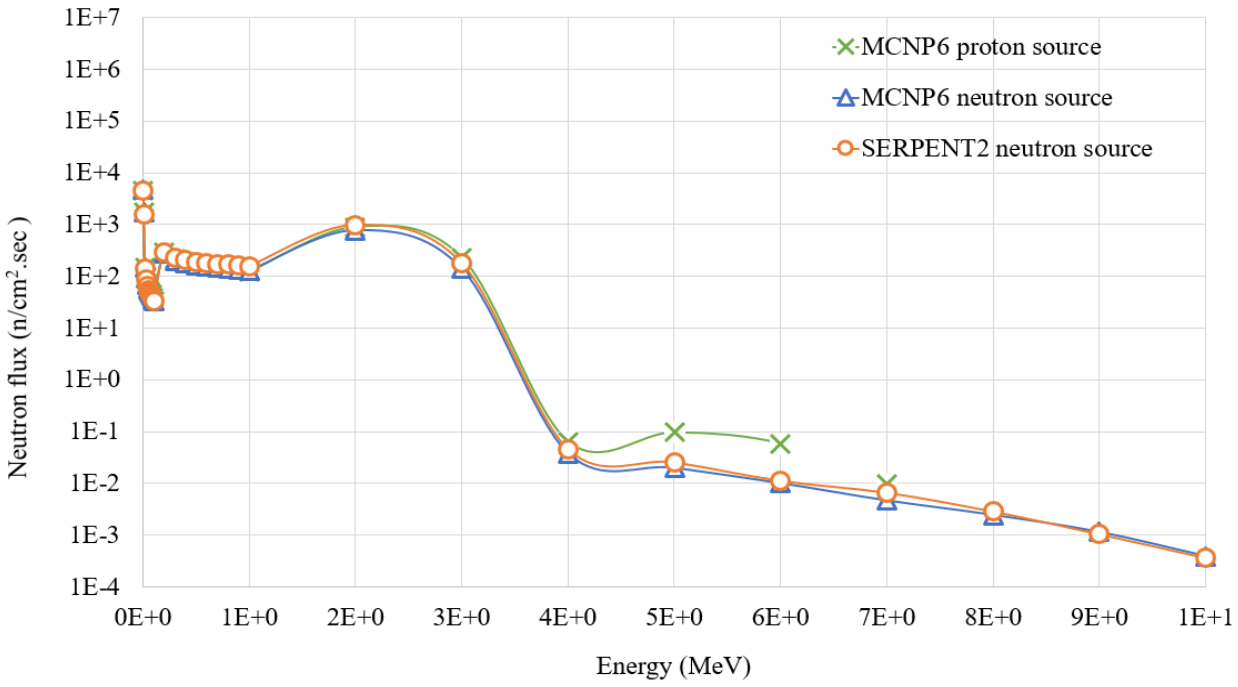

Figure 4.3: Neutron spectrum leak out of the shielding in MCNP6 and SERPENT2

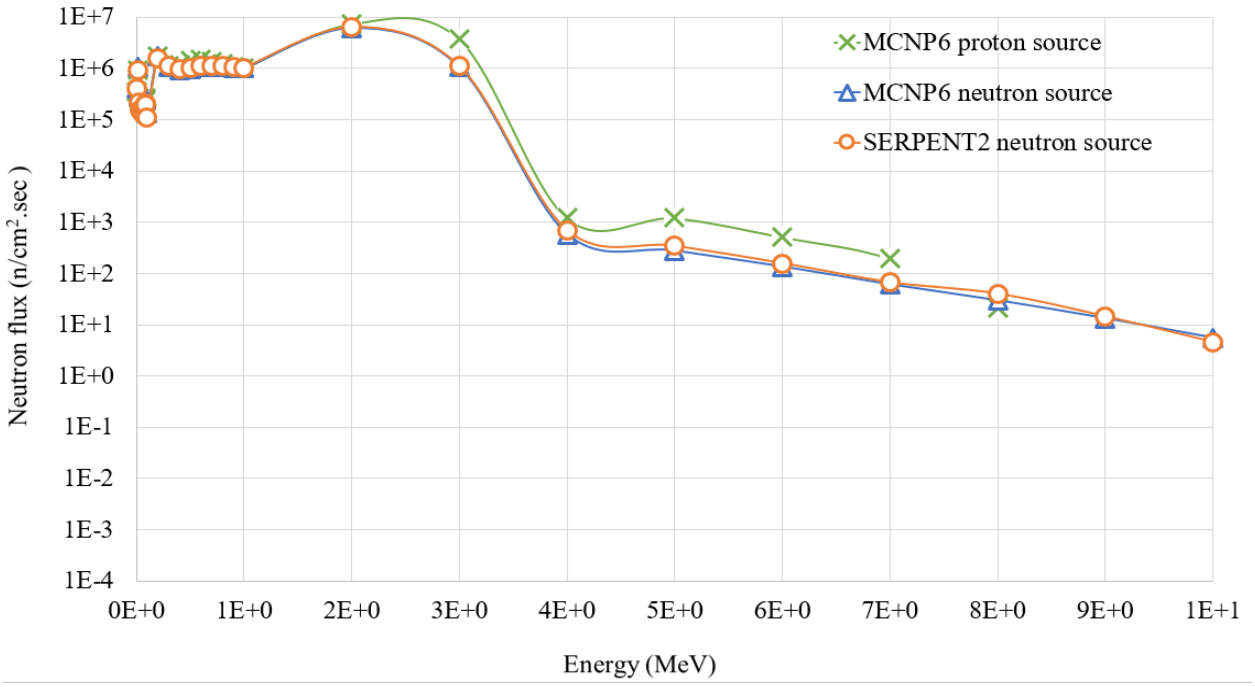

Figure 4.4: Neutron spectrum inside FLiNaK-ThF_4 test section in MCNP6 and SERPENT2

4.2 Shielding Material Thickness Bench Marking

This section talks about the bench marking of the optimum PE shielding thickness by comparing results of both MCNP6 and SERPENT2 Monte Carlo code. To do so, the sensitivity study was performed using each code, and as mentioned earlier, problem set up and parameters were defined equivalently in each of the input decks. The five thicknesses mentioned in chapter 3 were applied in both codes and results were compared. Figure 4.5 shows the average neutron spectrum in the detector located in front of the proton beam as a function of PE shield thickness in SERPENT2, and Figure 4.6 shows the same quantity in MCNP6. Comparing the two figures, it is shown that both have a maximum neutron energy of 5 MeV at 10 cm, 3 MeV at 20, 30, 40 cm, and a maximum of 1 MeV at 50 cm PE thickness in the two codes. Figure 4.7 shows the average neutron spectrum in the detector located in front of the proton beam at the maximum thickness (50 cm)for this side of the shielding wall using both MCNP6, and SERPENT2.

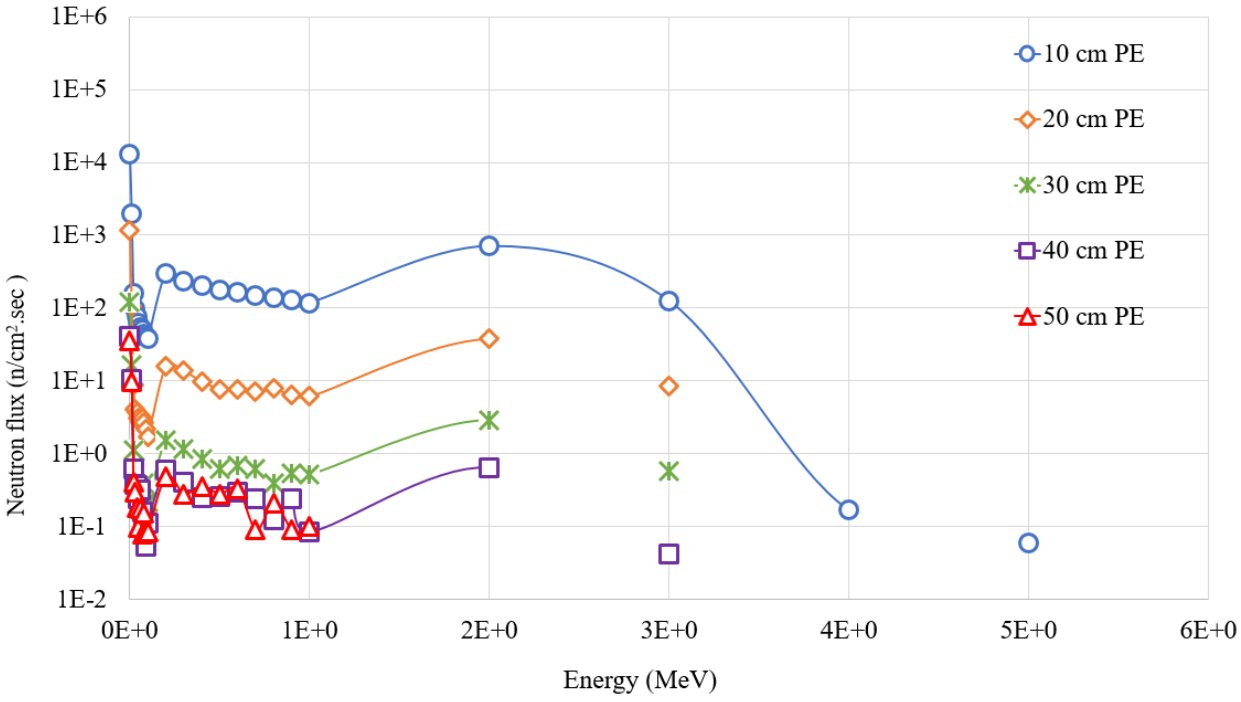

Figure 4.5: Average neutron spectrum in the detector as a function of PE thickness using SERPENT2

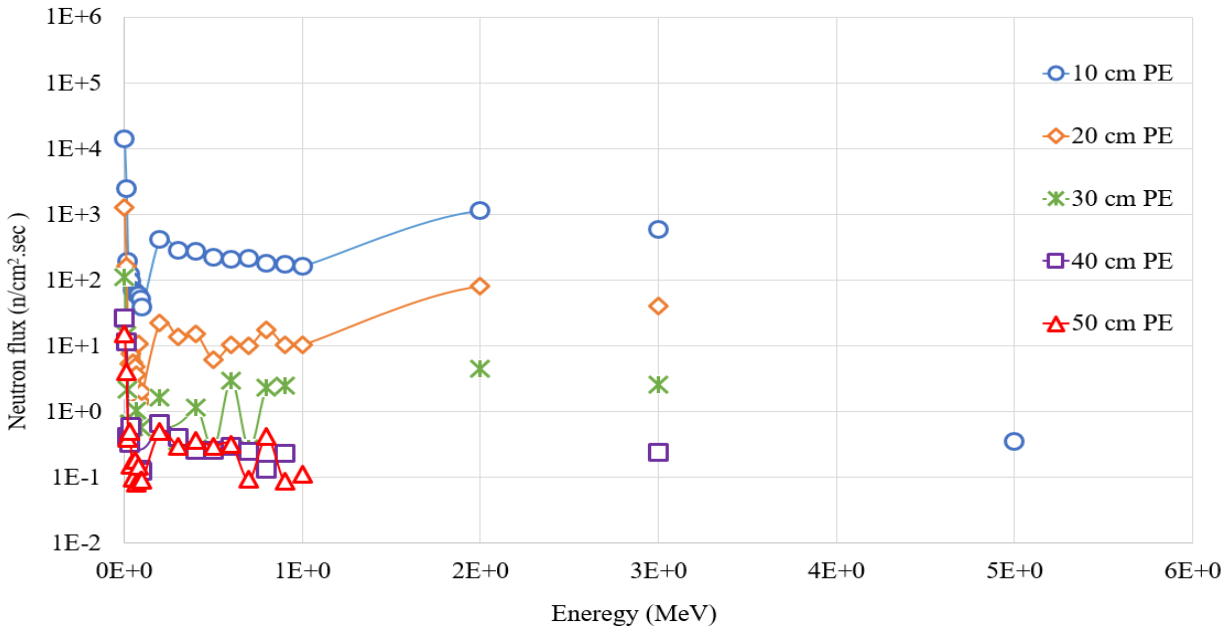

Figure 4.6: Average neutron spectrum in the detector as a function of PE thickness using MCNP6

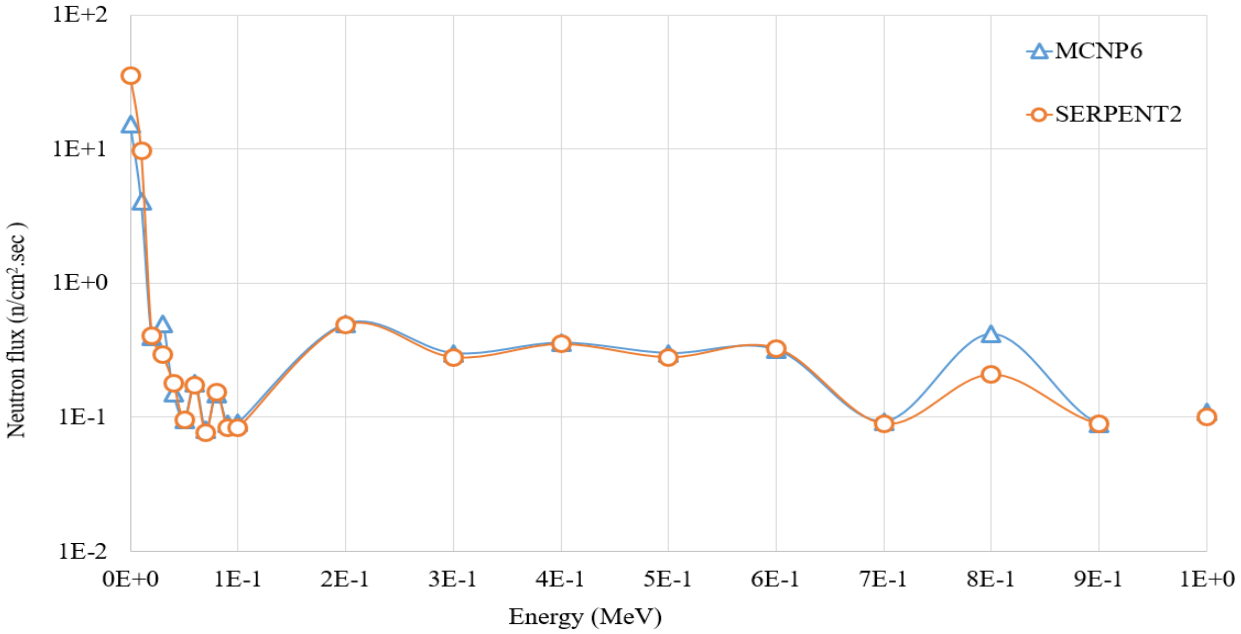

Figure 4.7: Average Neutron spectrum in the detector at 50 cm PE using MCNP6 and SERPENT2

4.3 Target Thickness Bench Marking

The target thickness sensitivity was performed using both codes, at first the optimum thickness was found to be 0.06 cm using MCNP6 at a location attached to the test section. The same tests were run with SERPENT2 to benchmark the target depth that can results in the largest number of fission neutrons production. Figure 4.8 shows the target sensitivity that was performed in both MCNP6 and SERPENT2.

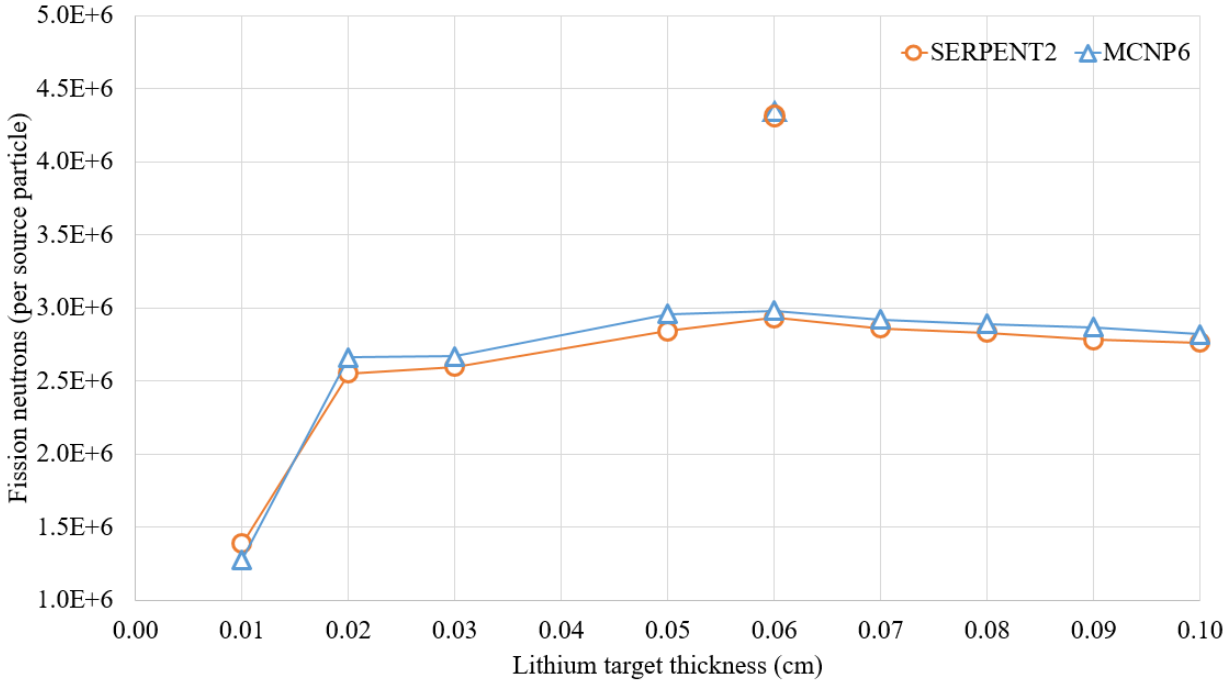

Figure 4.8: Lithium target sensitivity analysis using MCNP6 and SERPENT2

As shown above, SERPENT2 results bench mark the MCNP6 results, from here it can be said that 0.06 cm target depth is the optimum thickness. Not only that, but also the number of fission neutrons produced when target is attached to the test section is very close in the two codes.

Using SERPENT2 Monte Carlo code to bench mark results from MCNP6 is very important in this research, specially because there is no experimental results.

4.4 Conclusion

The research perform a detailed study and investigation on the proton accelerator driven thorium-fueled molten salt test loop, to design and optimize the major components of the facility. The facility is a combination of two sections; the proton accelerator, and the molten salt loop facility. It can be concluded from the results through out the work that:

1 - The proton source is a square surface source with 6*6 mm dimensions to simulate the physical squared aperture of the proton accelerator, it is mono-directional, mono-energetic (3 MeV to 4.5 MeV), and 2 $\mu Amps$ current. 2 - The optimum thickness for the graphite shield is 45 cm, it is the thickness with the minimum neutron energy at the graphite surface. 3 - The lithium target has a depth of 0.06 cm, and attached to FLiNaK-ThF_4 test section. 4 - The molten salt is composed out of a stainless steel 316 chamber that confine the molten salt, and a piping system that circulate the salt inside. 5 - The molten salt is composed of LiF-NaK-KF-ThF_4 with a mole fraction of 40.5-9.5-38-12, respectively. A MATLAB code was developed to convert the mole fraction into a weight fraction for each element to be input in MCNP6 and SERPENT2 input decks. 6 - The PE material composition was found to be a better shielding than the BPE. 7 - The annual dose rate was calculated, if the dose rate is to be limited annually, then 40 cm of PE meets the ICRP annual exposure limit (0.02 Sv/yr) assuming a total number of hours per year is 288, and 30 cm assuming 100 hours per year. 8 - The hourly dose rate was calculated as well, if the dose rate is to be restricted hourly based on the limits followed by the Nuclear Science Center (NSC) workers which is 1.25 $mrem/hr$, a minimum of 30 cm PE on one side, 50 cm on two sides, and more than 50 cm on the last side, but this is challenging due to cost and space. 9 - The hourly dose rate can be controlled be several factors, the approach that was followed to reduce the hourly dose in this research is to reduce the accelerator energy. Reducing the energy from 4.5 MeV to 2.5 MeV, a 20 cm on one side, 30 cm on the other three sides are required for shielding. 10 - Results from MCNP6 code were bench marked with results of SERPENT2 code. It is important to bench mark the results to make it reliable because so far, there are no experimental data.

REFERENCES

[1] S. Q. M. Jaradat, "Impact of thorium based molten salt reactor on the closure of the nuclear fuel cycle," 2015.

[2] W. Grimes, D. Cuneo, F. Blankenship, G. Keilholtz, H. Poppendick, and M. Robinson, "Chemical aspects of molten fluoride salt reactor fuels," *Fluid-Fueled Reactors*, p. 569, 1958.

[3] C. N. A. C. Z. Bahri, W. M. Al-Areqi, M. F. M. Ruf, and A. A. Majid, "Characteristic of molten fluoride salt system lif-bef2 (flibe) and lif-naf-kf (flinak) as coolant and fuel carrier in molten salt reactor (msr)," in *AIP Conference Proceedings*, vol. 1799, p. 040008, AIP Publishing LLC, 2017.

[4] R. E. Thoma, *Phase diagrams of nuclear reactor materials*, vol. 2548. Oak Ridge National Laboratory, 1959.

[5] M. Rosenthal, P. Kasten, and R. Briggs, "Molten-salt reactors—history, status, and potential," *Nuclear Applications and Technology*, vol. 8, no. 2, pp. 107–117, 1970.

[6] C. N. A. C. Z. Bahri, A. A. Majid, and W. M. Al-Areqi, "Advantages of liquid fluoride thorium reactor in comparison with light water reactor," in *AIP Conference Proceedings*, vol. 1659, p. 040001, AIP Publishing LLC, 2015.

[7] L. Mathieu, D. Heuer, E. Merle-Lucotte, R. Brissot, C. Le Brun, E. Liatard, J.-M. Loiseaux, O. Méplan, A. Nuttin, and D. Lecarpentier, "Possible configurations for the thorium molten salt reactor and advantages of the fast nonmoderated version," *Nuclear Science and Engineering*, vol. 161, no. 1, pp. 78–89, 2009.

[8] W. Ergen, A. Callihan, C. Mills, and D. Scott, "The aircraft reactor experiment—physics," *Nuclear Science and Engineering*, vol. 2, no. 6, pp. 826–840, 1957.

[9] H. MacPherson, "Molten-salt reactor program quarterly progress report for period ending july 31, 1960," tech. rep., Oak Ridge National Lab., Tenn., 1960.

[10] K. Furukawa, A. Lecocq, Y. Kato, and K. Mitachi, "Thorium molten-salt nuclear energy synergetics," *Journal of nuclear science and technology*, vol. 27, no. 12, pp. 1157–1178, 1990.

[11] K. Furukawa, H. Numata, Y. Kato, K. Mitachi, R. Yoshioka, A. Furuhashi, Y. Sato, and K. Arakawa, "New primary energy source by thorium molten-salt reactor technology," *Electrochemistry*, vol. 73, no. 8, pp. 552–563, 2005.

[12] C. D. Bowman, "Once-through thermal-spectrum accelerator-driven light water reactor waste destruction without reprocessing," *Nuclear Technology*, vol. 132, no. 1, pp. 66–93, 2000.

[13] H. Boussier, "Molten salt reactor system gif 2010 status," 2012.

[14] J. Caldwell, E. Dowdy, B. Berman, R. Alvarez, and P. Meyer, "Giant resonance for the actinide nuclei: Photoneutron and photofission cross sections for u 235, u 236, u 238, and th 232," *Physical Review C*, vol. 21, no. 4, p. 1215, 1980.

[15] E. Hayward and T. Stovall, "Photoneutron production by li6, li7, b10, b11 and o16," *Nuclear Physics*, vol. 69, no. 2, pp. 241–252, 1965.

[16] B. Bayanov, V. Belov, and S. Taskaev, "Neutron producing target for accelerator based neutron capture therapy," in *Journal of Physics: Conference Series*, vol. 41, p. 460, IOP Publishing, 2006.

[17] R. L. Martz, "Mcnp6 unstructured mesh initial validation and performance results," *Nuclear technology*, vol. 180, no. 3, pp. 316–335, 2012.

[18] J. Leppänen, M. Aufiero, E. Fridman, R. Rachamin, and S. van der Marck, "Calculation of effective point kinetics parameters in the serpent 2 monte carlo code," *Annals of Nuclear Energy*, vol. 65, pp. 272–279, 2014.

[19] V. Alferov, A. Radaev, M. Shchurovskaya, G. Tikhomirov, N. Hanan, and F. Van Heerden, "Comparative validation of monte carlo codes for the conversion of a research reactor," *Annals of Nuclear Energy*, vol. 77, pp. 273–280, 2015.

[20] D.Ćalić, G. Žerovnik, L. Snoj, and A. Trkov, "Analysis of neutron flux and reaction rates of triga research reactor using monte carlo code serpent," in *International Conference Nuclear Energy for New Europe*, pp. 8–11, 2014.

[21] A. Talamo1a, Y. Gohara, and J. Leppänenb, "Serpent performance with hybrid combinatorial and stereolithographic geometry," 2017.

[22] A. Talamo, Y. Gohar, and J. Leppänen, "Serpent validation and optimization with mesh adaptive search on stereolithography geometry models," *Annals of Nuclear Energy*, vol. 115, pp. 619–632, 2018.

[23] M. Cagnazzo, H. Herzog, M. Villa, and H. Boeck, "Serpent-2 reactor model validation at the vienna triga mark ii reactor," in *Proceedings of European Research Reactor Conference (RRFM)*, pp. 14–18, 2017.

[24] O. Novak, L. Sklenka, O. Huml, J. Frybort, O. Chvala, N. P. Luciano, and G. I. Maldonado, "Benchmark evaluation of zero-power critical parameters for the temelin vver nuclear reactor using serpent & nestle and mcnp," *Nuclear Engineering and Design*, vol. 353, p. 110243, 2019.

[25] F. Brown, "Fundamentals of monte carlo particle transport la-ur-05—4983," *Los Alamos National Laboratory, http://mcnp-green. lanl. gov/publication/pdf/ LAUR-05-4983_Monte_Carlo_Lectures. pdf*, 2005.

[26] J. F. Briesmeister *et al.*, "Mcnptm-a general monte carlo n-particle transport code," *Version 4C, LA-13709-M, Los Alamos National Laboratory*, vol. 2, 2000.

[27] F. Ager, M. Ynsa, J. Domınguez-Solıs, M. López-Martın, C. Gotor, and L. Romero, "Nuclear micro-probe analysis of arabidopsis thaliana leaves," *Nuclear Instruments and Methods in Physics Research Section B: Beam Interactions with Materials and Atoms*, vol. 210, pp. 401–406, 2003.

[28] J. Leppänen, "On the use of the continuous-energy monte carlo method for lattice physics applications," 2009.

[29] S. Lee, S.-W. Chung, S.-J. Lee, and Y. Yun, "Corrosion of type 316l stainless steel piping in synthetic gas plants," *Corrosion*, vol. 69, no. 9, pp. 921–953, 2013.

[30] C. Gesh, R. Pagh, R. Rucker, and R. WILLIAMS, "Radiation portal monitor project. compendium of material composition data for radiation transport modeling. pnnl-15870, rev. 1," *Pacific Northwest National Laboratory*, 2011.

[31] M. Chadwick, P. Obložinskỳ, M. Herman, N. Greene, R. McKnight, D. Smith, P. Young, R. MacFarlane, G. Hale, S. Frankle, *et al.*, "Endf/b-vii. 0: next generation evaluated nuclear data library for nuclear science and technology," *Nuclear data sheets*, vol. 107, no. 12, pp. 2931–3060, 2006.

[32] ICRP, *ICRP publication 60: 1990 recommendations of the International Commission on Radiological Protection*. No. 60, Elsevier Health Sciences, 1991.

[33] A. Santamarina, D. Bernard, P. Blaise, M. Coste, A. Courcelle, T. Huynh, C. Jouanne, P. Leconte, O. Litaize, S. Mengelle, *et al.*, "The jeff-3.1. 1 nuclear data library," *JEFF report*, vol. 22, no. 10.2, p. 2, 2009.